Palacký University
Olomouc

Faculty of Science
Department of Experimental Physics

Master Thesis

sp-state-based magnetism of 2D nanosystems

Boron-doped and Nitrogen-doped graphene nanoribbons - structural and magnetic properties from DFT calculations

Author: Bc. Zdeněk Baďura

Supervisior: Doc. Mgr. Jiří Tuček, Ph.D.

Consultant: Mgr. Piotr Blonski, Ph.D.

Degree program: N1701 Physics

Field of study: Nanotechnology

Bibliographical identification

Author's first name and suremane:	Zdeněk Bad'ura
Title:	sp-state-based magnetism of 2D nanosystems
Subitle:	Boron-doped and Nitrogen-doped graphene nanoribbons - structural and magnetic properties from DFT calculations
Type of thesis:	Master
Department:	Department of Experimental Physics
Supervisor:	Doc. Mgr. Jiří Tuček, Ph.D.
Consultant:	Mgr. Piotr Blonski, Ph.D.
Year of presentation:	2017
Number of pages:	138
Language:	English
Key words:	Density functional theory, *VASP*, magnetism, graphene, graphene nanoribbons, boron, nitrogen

Declaration

I hereby state, that I have written this Thesis myself under the supervision of Mgr. Piotr Blonski, Ph.D. and Doc. Jiří Tuček, Ph.D. All used resources are listed under Bibliography.

In Olomouc, date ....

Signature

Acknowledgment

A special acknowledgement goes to my thesis consultant Mgr. Piotr Blonski, Ph.D.,to whom I am very grateful for his enormous amount of patience during the whole process of creating this thesis and for his kind words when were needed.

Further, I would like to thank my supervisior doc. Mgr. Jiří Tuček, Ph.D., this thesis would not have been created without his help and support.

The support from the Internal Grant Agency of the Palacký University in Olomouc (Project No. IGA_PrF_2017_025) is gratefully acknowledged.

Abstract

To date, a broad familly of carbon nanostructures, as carbon nanotubes, nanohorns, onion-like carbon, nanodiamonds, carbon dots, graphene, graphene quantum dots, *etc* has been discovered but the most studied carbon nanoallotrope is graphene. The research of graphene and its derivatives is rapidly evolving topic, because of unique properties of graphene, including ambipolar effect, room-temperature half-integer quantum Hall effect, *etc*. Due to its extraordinary conductivity graphene is a desirable candidate for electronic/optoelectronic and spintronic applications. For spintronic applications it is required to develop magnetically active graphene, which can be achieved by using defects such as vacancies in the graphene lattice, heteroatom doping by light elements, spatial restrictions of graphene sheet. In this thesis we studied two fundamental types of graphene nanoribbons (*i.e*, armchair and zigzag graphene nanoribbons) with bare edges and also with edges passivated by hydrogen atoms. Further, we studied in details the properties of nanoribbons doped by boron and nitrogen. Several configurations of dopant atoms were chosen; these motifs have been tested in *AGNNs* and *ZGNNs* of different widths and with bare and passivated edges by hydrogen atoms. For calculations and modeling of magnetic properties of graphene nanoribbons we use Vienna *ab initio* simulation package.

Contents

Introduction

Carbon is one of the basic elements in nature and life on Earth. It is a building block of all organic molecules and thus the living organisms. Carbon plays the key role in a world's energetic industry where the fossil fuels are used for electricity production. The importance of carbon in other branch of industry as chemical industry and production of plastic materials is also worth mentioning.

Pure carbon occurs naturally in several bulk allotropes such as the various types of amorphous carbon, diamond and graphite. It can hardly be found a pair of materials of different properties such as diamond and graphite have. Diamond is a transparent electrical insulator and the hardest known material. In contrast, graphite is opaque soft conducter. These differencies comes from the abillity of carbon to exist in different hybridization states. Diamond is made of tetrahedral sp^3 hybridized carbons forming large crystals. Conversely, graphite is made of sp^2 hybridized carbon atoms, which forms graphene monolayers that are held together by van der Waals interactions.

1985 witnessed the discovery of new carbon structure which is made of 60 carbon atoms arranged in pentagons and hexagons to form a spherical structure [1],[2]. These structures are known as fullerens and form the bridge between molecules and nanomaterials. The discoveries of another smaller and

bigger fullerenes followed. To date, a broad familly of carbon nanostructures, as carbon nanotubes, nanohorns, onion-like carbon, nanodiamonds, carbon dots, graphene, graphene quantum dots, *etc* has been discovered. The most studied carbon nanoallotrope is graphene [3]. Graphene is a planar structure made of sp^2 hybridized carbon atoms arranged in a honeycomb lattice. The research of graphene and its derivatives is rapidly evolving topic attracts interest of many scientific groups working in various fieds. It is because of unique properties of graphene, including ambipolar effect, room-temperature half-integer quantum Hall effect, *etc*. Due to its extraordinary conductivity graphene is a desirable candidate for electronic/optoelectronic and spintronic applications.

Pristine graphene is a diamagnet. Thus, for spintronic applications it is required to develop magnetically active graphene, ideally with high Curie temperature, with spin-polarized conductive behavior. Localized magnetic moment can be implemented in graphene sheet by using defects such as vacancies in the graphene lattice [4], heteroatom doping by light elements [5], spatial restrictions of graphene sheet [7], *etc*.

In this thesis we studied graphene sheets cut along certain directions to form narrow strips known as graphene nanoribbons [8]. Experimental results indicate that the most common chiral edge configurations are 0^o (armchair) and 30^o (zigzag), which leads to armchair and zigzag nanoribbons, respectively. Further, we studied in details the properties of nanoribbons doped by boron and nitrogen. Both elements are used in classical semiconductor technology very frequently. Boron atom, which has one electron less than carbon, should induce p-type behavior in graphene lattice. In case of nitrogen, one

electron remains unpaired, thus n-type behavior is expected [6]. The nature of these dopant elements has strong influence on the magnetic properties of graphene based nanomaterials and nanostructures [9]. For calculations and modeling of magnetic properties of graphene nanoribbons we use Vienna *ab initio* simulation package where the spin polarized density functional theory is implemented [10], [11]. The method has been successfully employed to study similar systems [5], [6], [12]. The study of influence of dopation by boron and nitrogen atoms on magnetic properties of graphene nanoribbons is the aim of this thesis.

1 Theoretical part

1.1 Carbon nanoallotropes

A broad family of carbon nanoallotropes is known and many others has been theoretically predicted. It comes from the ability of carbon to exist in different hybridization states (sp, sp^2, sp^3) and to participate in covalent bonds between them. Carbon nanostructures can be classified in several ways, i.e., (i) according to the type of hybridization between C atoms, or (ii) based on dimensionality of carbon nanostructure (see Figure 1.1). The latter has been used in this work. According to this classification, three groups of carbon nanoallotropes can be distinguished:

(i) **0.D** - Fullerens, onion-like carbon (OLC), carbon dots ($C\text{-}dots$), graphene quantum dots ($GQDs$) and nanodiamonds

(ii) **1.D** - Carbon nanotubes ($CNTs$), carbon nanofibers and single-walled carbon nanohorns ($SWNHs$)

(iii) **2.D** - Graphene, graphene nanoribbons and multilayer graphitic nanosheets

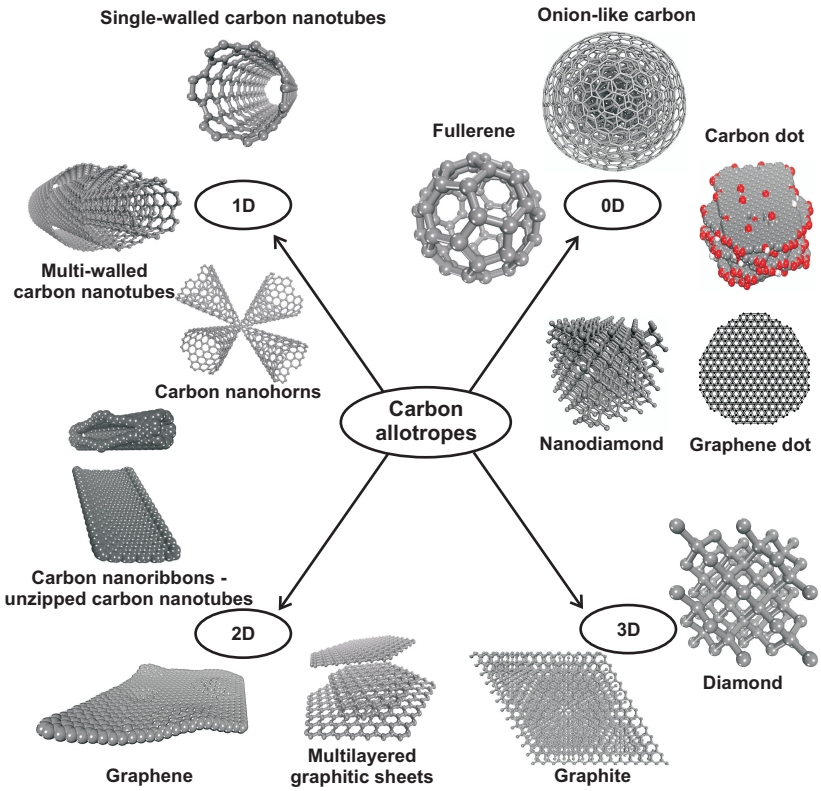

Figure 1.1: Classification of carbon allotropes according to their dimensionality. Reprinted with permission from ref. [13].

1.1.1 0.D Carbon nanoallotropes

Fullerenes

Fullerenes C-60 were manufactured in 1985 as the first member of the carbon nanostructures family [1]. To date, a large group of fullerenes consisting of different number of carbon atoms (both, bigger and smaller than C-60) is known. Fullerenes are made of sp^2 carbon atoms arranged in hexagons and pentagons, which are assembled in to the shape of sphere. The number of pentagons in perfect fullerene structure is always 12. Compared to that, the

number of hexagons depends on the size or more precisely on the number of carbon atoms contained in the fullerene. A fullerene with $20 + 2n$ carbon atoms has n hexagons following the well-known Euler rule. Buckminster-fullerene, the C-60 fullerene consisting of 12 pentagons and 20 hexagons is the most studied fullerene so far.

Fullerene C-60 does not have properties characteristic for another carbon nanoallotropes such as conductivity and mechanical strength. It is caused by limited size and molecular character of the fullerenes. However, fullerenes can be used as radical scavenger in various applications as an antioxidant in cosmetics and biologigal systems [14], [15].

In a solid phase, fullerenes form aggregates and crystallize in a face-centered cubic (*fcc*) lattice [2]. Fullerenes aggregates and crystals are solutable in many organic solutions [16].

Fullerenes crystals include cavities which can host several species, for example alkali metals. These doped crystals are superconductive at low temperatures. Potassium-doped C-60 crystals has transition temperature at 18 K [17]. More complex C-60 crystals such as Rb_2CsC_{60} are superconductive below 33 K [18].

Onion-like carbon

Carbon nanostructures known as onion-like carbon *OLC* are multishell spherical structure containing couple of fullerenes where the smaller fullerenes are sealed in the bigger ones. *OLC* can be prepared in various sizes. By heating carbon soot under vacuum *OLC* structures with 2-8 shells and diameter from 3 to 10 nm can be prepared. For preparation of larger structures with

mean diameter of 25-30 nm an arc discharge between graphite electrodes in water can be used [19]. The most promising aplication of OLC is in supercapacitors as electrodes [20]. Due to large specific surface area ($\sim 500\,\mathrm{m^2 g^{-1}}$) which is fully accesible to ion adsorption, the OLC are often used where the limited volume is available for device integration.

Carbon dots

Carbon dots are quasi-spherical nanoparticles that assume mostly an amorphous form and contain sp^3-hybridized carbon. The most striking characteristic of C-dots is photoluminiscence which depends on both the excitation wavelength and the size and surface functionalization of C-dots. The wide range of spectra and high intensities of the emission peaks underline the multicolor properties of C-dots. The distinct colors observed in photoluminiscence of C-dots are connected with energy states associated with surface defects in the graphitic nanoparticles. The surface functionalization is often used to get single emission wavelengths. C-dots are also dispersible in water and exhibit extremely low toxicity.

Above mentioned properties are useful for several applications in biology and nanomedicine [21]. For example the great potential of the C-dots is in cell imaging with two-photon luminescence microscopy [22].

The top-down approach using laser ablation is typical for preparation of C-dots. The final nanoparticles have diameter of about 5 nm. Other methods of preparation are based on the thermal decomposition or carbonization of organic compounds [13].

Graphene quantum dots

Properties of graphene sheets with diameter under 100 nm are strongly affected by character of the edges. Graphene quantum dots ($GQDs$) are small pieces of graphene with diameter of $2-20$ nm composed dominantly of sp^2-conjugated carbon atoms and therefore the properties of $GQDs$ are strongly dependent on the edges and also on the size, geometry and on the shape of $GQDs$ [23], [24].

GQDs with zigzag edges with average diameter of $7-8$ nm are metallic due to the presence of zigzag edge states [23]. Conversaly,$GQDs$ with armchair edges have non-zero band gap inversely proportional to the size (the smaller $GQDs$ the larger band gap). This dependence of band gap on the size of $GQDs$ is interesting for applications in photovoltaic devices, phototransistors and photocatalysis [13], [25], [26].

The major property of $GQDs$ is strong photoluminiscence as in the case of C-dots and it can be also tuned by chemical functionalization.

Nanodiamonds

Nanodiamonds are crystaline structures containing sp^3 hybridized carbon atoms. They exist in the range of diameters between 2 and 20 nm. Structures below 2 nm are known as diamondoids and their properties are strongly governed by surface pheneomena due to high surface to volume ratio. Conversaly, the crystals with diameter above 20 nm behave like bulk diamonds. Nevertheless, nanodiamonds bring many of the extraordinary properties of bulk diamond to the nanoscale. These properties include superior hardness and Young's modulus, biocompatibility, high thermal conductivity, chemical

stability and the resistance of nanodiamond to harsh environments [27]. The major property of nanodiamonds is an electrical resistivity but boron-doped nanodiamonds are conductive and can be used in electrochemical double-layer capacitors and batteries [27], [28]. Heteroatoms (especially, nitrogen) contained in the nanodiamonds can form heteroatom-vacancy centers. These nitrogen-vacancy centers can be neutral or negatively charged. The negatively charged nitrogen-vacancy centers are more studied than neutral centers, due to spin ground state (S = 1) and paramagnetic nature [13]. Nitrogen-vacancy centers in nanodiamonds exibit bright luminescence with possible applications in photonic crystals and waweguides. Similarly to nitrogen-vacancy centers contain in nanodiamonds, silicon-vacancy, chromium-vacancy, nickel-vacancy sites have been reported [29], [30].

1.1.2 1.D Carbon nanoallotropes

Carbon nanotubes

Carbon nanotubes *CNTs* are cylindrical structures consisting of sp^2 hybridized carbon atoms arranged in hexagonal lattice as in the case of graphene [31], [32]. *CNTs* can be single-walled (*SWNTs*), double-walled (*DWNTs*) and multi-walled (*MWNTs*).

SWNTs have diameters in the range of $0.4 - 2$ nm and the length is in order of micrometers and therefore the main characteristic of *CNTs* is high value of aspect ratio (i.e., length-to-diameter ratio). It can exceed 10 000, and thus *CNTs* are regarded the most anisotropic materials ever produced [13].

Another impotant parameter is chirality which determines conductivity of

CNTs. Depending on a chiral vector, *CNTs* can be semiconducting or exibit metallic behavior. The chiral vector is defined by expression $\vec{C} = n\vec{a_1} + m\vec{a_2}$, where n and m are integers, $\vec{a_1}$ and $\vec{a_2}$ are unit cell vectors. And, for example, armchair *CNTs* have $n = m$. These nanotubes have finite value of density of states at Fermi level, exibit metallic behavior and low resistivity [33]. Conversely, zigzag *CNTs* are either metallic or semiconducting depending on their diameter. Unexpectedly, bend-ended *MWNTs* are superconductive below 12 K [34].

Regarding to the mechanical properties of *CNTs*, superelasticity and high value of Young's modulus should be mention. In case of *MWNTs*, the Young's modulus was found to be up to 1.8 TPa. Similarly, the Young's modulus of *SWNTs* has been measured at 1.25 TPa [13].

Carbon nanofibers

Carbon nanofibers *CNFs* are linear filaments with diameter from 50 to 200 nm consisting of sp^2 hybridized carbon atoms. The aspect ratio commonly exceeds 100. Contrary to the previous case of *CNTs*, carbon nanofibers have no cavity space [35].

According to the inner structure, carbon nanofibers can be separated in several groups as platelet *CNFs*, herringbone *CNFs*, ribbon *CNFs* and cone-helix *CNFs*, *etc.* [36], [37].

Because of a good electrical conductivity and structural stability, *CNFs* are proper candidates for applications in supercapacitors and for battery applicatipons. However, the specific capacitances of *CNFs* is lower than those of other materials (*e.g.*, metal oxides and hydroxides) [38]. To improve its

electrical properties, substituting some atoms with heteroatoms, such as nitrogen, sulphur and boron is often used. These nanostructures have a high reversible capacity and an excellent cycling stability [39].

The extremaly large specific surface area (up to $3000\,\mathrm{m^2g^{-1}}$) of activated *CNFs* coresponding to high affinity for a gas adsorption is also worth of mentioning [40].

Carbon nanohorns

Single-walled carbon nanohorns (*SWNHs*) have conelike structures [41]. *SWNHs* form large spherical aggregates with diameter around of $80 - 100$ nm depending on preparation method. CO_2 laser oblation of graphite target at room temperature and arc-discharge techniques are the most often used.

The electronic properties of *SWNHs* are strongly dependent on the structure. *SWNHs* formed in shape of Dahlia flower behave as n-type semiconductor, but if they are oxidized, they show p-type properties [13]. The carbon nanohorn films are promising candidates for field emission applications for its good field emission characteristics. Also a gas-adsorption phenomenon makes it possible to use carbon nanohorns in fuel cells [42].

1.1.3 2.D Carbon nanoallotropes

Graphene

Graphene was first isolated in 2004 [3]. Since than graphene attracts many scientific groups from different fields and it is because of its high electrical and thermal conductivity and capacity to carry large currents at room temperature, room-temperature quantum Hall effect, *etc.* [43].

Graphene has a planar structure made of sp^2 hybridized carbon atoms arranged in a hexagonal lattice with the lattice parameter about 1.42 Å. The hexagonal graphene lattice (also known as honeycomb lattice) consists of to interleaving triangular sublattices (α, β). Carbon atoms are connected by covalent σ bonds and it is the strongest known material. The unhybridized p orbitals of carbon atoms are oriented out of the plane and interact with one another to form what is referred as the half filled π band which gives graphene its aromatic character and is responsible for most of its electronic properties.

Graphene has zero density of states at the Fermi level and it is decribed as a zero bandgap semiconductor or semimetal. The high conductivity (*i.e.*, low resistivity) of graphene and its capacity to carry large currents (carrier mobilitiy of up to $\sim 2.5\,\mathrm{m^2V^{-1}s^{-1}}$ at room temperature) are important properties for applications in electronic devices [44]. The charge carriers act as massless relativistic particles and have same properties of Dirac fermions, thus they can be described by Dirac's equation [45]. Graphene exhibits an ambipolar electric field effect as well [46].

The thermal conductivity at room temperature has been measured up to $5300\,\mathrm{Wm^{-1}K^{-1}}$, that establlishes graphene as an exelent material for thermal management [47].

Optical transmittance of graphene monolayer is 97.5% but with increasing number of stacked monolayers transmittance decreases rapidly [48]. The high thermal conductivity mediated by covalent bonds is inherent to graphene.

Due to above mentioned extraordinary properties, possible applications of graphene are particularly in high-speed electronics, optoelectronic devices

including displays, and solar cells [3], [46]. One of the major advantages of graphene is the high compatibility with current *CMOS* technology. Another possible applications for graphene are sensors for single-molecule detection [49]. Even so, the absence of an energy gap in graphene limits its application for an electronic switching devices as graphene-based transistors with high enough on-off ratio. Several methods of band-gap engineering (*e.g.*, substrate effects, hydogenations, adatoms, *etc.*) can be used [50].

Graphene nanoribbons

Graphene nanoribbons (*GNNs*) are a wide strips of graphene sheet and as in the case of graphene they are in great research attention. It is due to combination of unique properties of pristine graphene together with spatial restrictions of *GNNs*. According to the edge structure, the three types of (*GNN*) can be recognized: armchair graphene nanoribbons (*AGNNs*), zigzag graphene nanoribbons (*ZZGNNs*) and chiral nanoribbons.

The electronic properties of *GNNs* are strongly dependent on the edge character and the key role plays also the width. Both types, *AGNNs* and *ZZGNNs*, show non-zero band gaps. In the case of *AGNNs*, as the width of nanoribbons increases, the band gap decreases finally reaching the limit case of infinite graphene with zero band gap. Similarly, the size of band gaps of *ZZGNNs* also decreases with increasing width till the particular value $7 - 8$ nm is exceeded [13]. Than the *ZZGNNs* become metallic due to edge states present as a flat band around the Fermi level and thereby give a sharp peak in the density of states [13], [51]. The electron density in the edge states is localized on a zigzag edges. *AGNNs* have no such localized states.

But graphene nanoribbons with general edges (*i.e.*, mixture of zigzag and armchair edges) have non-negligible edge states even than, if zigzag edges are less developed [40].

The thickness (*i.e.*, number of stacking layers) has also strong influence on the electronic properties on graphene nanoribbons. The band gap of multilayered *AGNNs* decreases and in the case of multilayered *ZGNNs*, the number of edge states incrases.

The unsaturated bonds on the zig-zag edges offer the possibility for functionalization of these *ZZGNNs* and thus tuning their properties.

The edge structure has major influence on magnetic properties of *GNNs* which will be discussed later.

Multilayer graphitic nanosheets

Multilayer graphitic nanosheets (*MGNs*) are formed from 2 up to 10 layers of graphene sheets. *MGNs* have similar properties to previously mentioned graphene. *MGNs* are usually prepared as byproducts of synthesis of monolayer graphene which is of greater interest.

The physical properties such as electrical and thermal conductivity are strongly dependent on the number of graphene layers stacked together and on the position of carbon atoms in neighbouring layers [13].

1.2 Magnetism in carbon nanoallotropes

All known carbon allotropes are diamagnets. The diamagnetic susceptibility of graphite is very large and it is exceeded only by the magnetic susceptibility of superconductors. In the case of diamond, the magnetic susceptibility contains two dominating diamagnetic contributions from core and valence electrons and a small paramagnetic term (van Vleck) coming from magnetic dipole transitions. But magnetism in nano-sized carbon allotropes is much more sundry.

1.2.1 Fullerenes

Pure fullerenes are diamagnetic and its susceptibily consists of two contributions, i.e. a paramagnetic term from the pentagonal rings and diamagnetic term from the hexagonal rings. Therefore, the diamagnetic susceptibility should increase with the size of cluster. Nevertheless the diamagnetic susceptibility of fullerenes containing less than 100 atoms is varying randomly [52]. Diamagnetic susceptibility of larger fullerenes approaches the value for graphite, as expected, the fullerene C-5000 has a susceptibility equal to graphite's [53].

The ferromagnetic behavior of fullerene derivatives was observed in complexes C-60-TDAE (tetrakis(dymethylamino)ethylene) with transition temperature at 16 K [54]. It is believed, that ferromagnetism is established due to strong donor-acceptor interaction. Similar magnetism below 19 K was observed where the TDAE was replaced by another strong donor compounds. However, in cases where C-70 is used instead of C-60, long-range magnetic ordering is lost [13], [53].

Another fullerene based material showing ferromagnetic behaviour is two-dimensional rhombohedral C-60 fullerene prepared at 6 GPa [55]. Structures prepared at 800 K show strongest magnetism with a saturation magnetization reaching $0.045\,\mathrm{emu\,g^{-1}}$. With increasing temperature of preparation the number of collapsed fullerenes increases and the grafitization is expected [56].

The influence of the fullerenes on single molecular magnets has been studied. Complexes of $Mn_{12}-$based molecular magnets containing fullerenes shows behavior regarded as magnetic training in a measurements of hysteresis loops. It is due to orientation of incorporated fullerenes molecules in magnetic field [57].

1.2.2 Nanotubes and nanohorns

The magnetic behavior of carbon nanotubes and nanohorns is similar to the behavior of pure fullerenes. The magnetic susceptibility of *CNTs* and *SWNHs* contains both diamagnetic and paramagnetic parts [13], [58]. To induce magnetic ordering in *CNTs* and in *SWNHs* the same strategy as in the case of graphene is often used (*i.e.*, using defects such as vacancies in the lattice, doping by heteroatoms) [59], [60]. However in case of *CNTs* a functionalization with magnetic nanoparticles is more promising approach [61]. The magnetic nanoparticles can be attached on the surface of *CNTs* or can be placed inside the cavity place of *CNTs*. The wide range of applications of functionalized *CNTs* include components in magnetic data storage devices, toners and inks for xerography, *etc.* [61]. CNTs find attractive applications in medicine as contrast agents in magnetic resonance imaging and magnetically guided drug delivery [62], [63].

1.3 Magnetism in graphene

Pristine graphene is diamagnetic. It is due to unhybridized p orbitals of carbon atoms oriented perpendicular to the graphene plane forming extensive π-bonding network with delocalized π-electrons [64]. It is believed that localized magnetic moments can be realized by presence of structural defects in graphene lattice. The defects include vacancies, heteroatoms in graphene lattice, adatoms, spatial restrictions and mixed hybridizations $sp^2 - sp^3$ (see Figure 1.2)[64], [65].

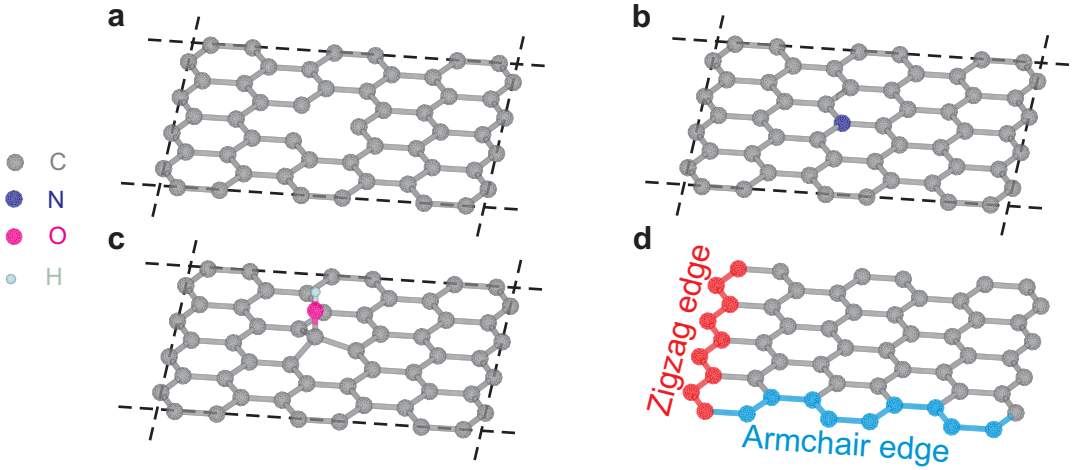

Figure 1.2: (**a**) a single atom vacancy in the graphene structure, (**b**) heteroatom (in this case nitrogen), (**c**) chemical functionalization (in this case by -OH group) and (**d**) the fundamental types of edges.

As a consequence of defects in graphene, a flat bands in the band structure of graphene are induced and they can be seen as a semilocalized π *midgap* states in density of states near the Fermi level [66]. All mentioned types of defects of graphene lattice and their influence on magnetic behavior of graphene are discussed below.

1.3.1 Vacancies in graphene lattice

The simplest defect in any material is missing lattice atom and single vacancies in graphene are result of a missing carbon atom. To minimalize energy of single vacancy and to complete the ring structure, the atoms around vacancy relaxe in a pentagon and a nine-membered ring. Due to the reconstruction of the atomic positions neighboring to double vacancy two pentagons and one octagon defect are formed. The formation energy $\mathrm{E_f}$ of single vacancies and double vacancies is of the same order ($\backsim$ 8 eV). Hence, double vacancies are thermodynamically favored than single vacancies. The formation energy is given as

$$\mathrm{E_f} = \frac{1}{n}\left(\mathrm{E_{Vn}} - \frac{N-n}{N}\mathrm{E_g}\right) \tag{1.1}$$

where n is number of vacant atoms and $\mathrm{E_{Vn}}$ is total energy of n vacancies in graphene, N and $\mathrm{E_g}$, respectively, are the total number of carbon atoms in graphene and its total energy [67], [68]. The migration barrier for monovacancy in graphene is $\sim$ 1.3 eV. Compared to that, the energy of migration barrier for divacancy reaching 7 eV and they are practically immobile [65]. In case of multiple vacancies, energetically favored are vacancies with even number of missing atoms it is due to a complete saturation of dangling bonds. On the contrary, in the case of vacancies with an odd number of missing atoms the dangling bonds remain open.

It has been theoretically predicted and experimantally confirmed that vacancies in graphene carry magnetic moments $\mu \approx 1\,\mu_B$ (where μ_B is Bohr magneton) and they can interact in ferromagnetic (FM) or antiferromagnetic (AFM) way [13], [64], [69], [70]. The total spin S of the bipartite graphene

lattice is given by the Lieb's theorem

$$\mathrm{S} = \frac{1}{2} |n_\alpha - n_\beta| \tag{1.2}$$

where n_α, n_β respectively, is number of atoms present on the sublattice α , β [71]. Accordingly, vacancies present only on the one type of subblatice bring ferromagnetic ordering in graphene sheet. Conversaly, if the vacancies occur on both sublatticies with equal propability, antiferromagnetic ordering is expected. Nevertheless the energy difference between ferromagnetically and antiferromagnetically coupled vacancies for the same configuration is very small and Curie temperature is about of $\mathrm{T_C} \sim 1\,\mathrm{K}$ [72]. Hence, at higher temperatures, graphene with vacancies will respond as a paramagnetic material, which is in an agreement with experimental measurements [74].

1.3.2 Substitutional doping of graphene by heteroatoms

Atomic substitution of carbon atoms by hetero atoms is another way how to induce localized magnetic moments in graphene lattice. The electronic and magnetic properties depend on the type of dopant atom, location and its concentration in the graphene structure. The charge carriers can be either electrons or holes. Accordingly two types of dopant atoms can be distinguished n-type or p-type. In both cases, the position of the Fermi level is modified and the positon of the highest occupied molecular orbital *HOMO* and the lowest unoccupied molecular orbital *LUMO* with respect to the Dirac point is important for determination of direction of charge transfer (see Figure 1.3).

The formation energy of graphene doped systems is given as

$$\mathrm{E_f} = \frac{1}{n} \left[\mathrm{E_{dpd}} - \mathrm{E_{graph}} + n \left(\mu_C - \mu_{sub}\right)\right] \tag{1.3}$$

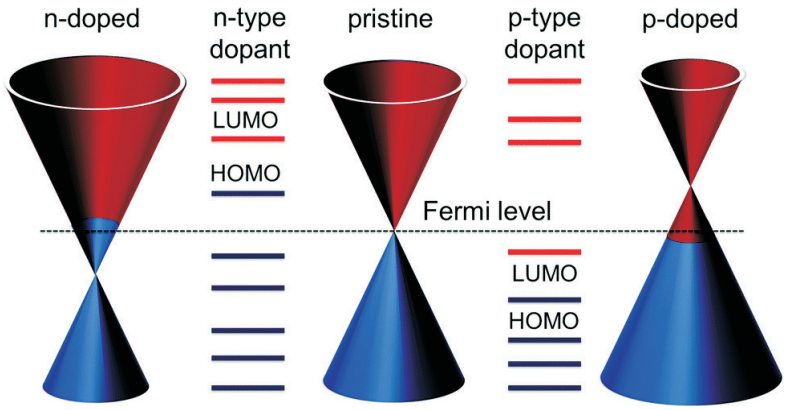

Figure 1.3: Schematic showing positions of *HOMO-LUMO* levels of n-type and p-type dopants with respect to pristine graphene. Reprinted with permision from ref. [75].

where E_{graph} and E_{dpd} is total energy of pristine and doped graphene, respectively, n is number of substituted atoms, μ_C and μ_{sub} are chemical potentionals of carbon and dopant atoms [5]. Boron and nitrogen are the natural dopants, they have approximately same atomic radius [6], [65]. Larger foreign atoms such as sulfur, phosphorus or transition metals, *etc.*, also received particular attention [5], [76], [77]. Substitution of carbon atoms by boron and nitrogen is often used to design band gap for electronic applications [6], [78]. It is possible to induce magnetic response in graphene due to dopation in specific ranges of concentrations. It has been reported that graphene with concentration of nitrogen atoms below 5 at% is diamagnetic. Interestingly, at ~ 5 at% of nitrogen in graphene paramagnetic centers iduced by dopation begin to interact to establish ferromagnetism. The saturation magnetization of nitrogen doped graphene at 5.1 at% was measured at 1.09 emu g^{-1} at temperatures below ~ 69 K. It was identified that in N-doped graphenes ferromagnetic orderring in the graphene lattice at low temperatures emerges mostly

due to substitution of nitrogen atoms in graphitic positions [79]. Graphene with higher concentrations of nitrogen, *i.e.*, at 6.25 at% and at 12.5 at% show magnetic moment of 0.75 μ_B, 0.61 μ_B per supercell, respectively [80]. It has been theoretically predicted and experimentaly confirmed that sulfur doped graphene at 4.2 at% show strong ferromagnetism with saturation magnetization of 5.5 emu g^{-1} below the temperature at $\sim$ 62 K. The superior magnetic properties of the S-doped graphene over the N-doped analogues can be explained in terms of injection of two unpaired electrons by each sulfur atom to the conducting band. These electrons are delocalized among the S and C atoms contrary to those injected by N-doping that are dominantly localized at the N-sites. The pumping of electrons from substitutional sulfur to the graphene conduction band is also believed to promote the sustainability of the magnetism at relatively high temperatures (up to $\sim$ 62 K) [5].

1.3.3 Edge magnetism

The edge structure has major influence on magnetic properties of graphene structures, especially of graphene nanoribbons. The three types of edges can be distinguished as was discussed in the section 1.1.3. The zigzag edges are often short and defective. On contrary, the armchair edges tend to be long and defect free, that means the armchair edges are energetically more stable than zigzag edges having the edge states at the Fermi level. The origin of the edge states is in the breaking symmetry phenomenom of the Dirac electrons due to boundary conditions at the zigzag edges [81]. Hence the edge states in zigzag edges have same origin as non-bonding states in non-Kekulé type of an aromatic molecules which particular feature is magnetism [82]. Conversaly,

Kekulé molecules have a large *HOMO-LUMO* gap between the π-bonding and π^*-antibonding states with no midgap states.

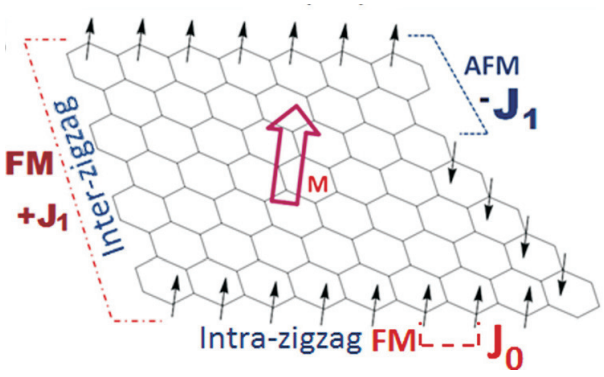

Figure 1.4: The exchange interaction between the edges in an arbitrary shaped graphene sheet. Reprinted with permission from ref. [83].

The presence of the non-bonding edge states gives rise to localized magnetic moments. In case of zigzag edges, carbon atoms along one edge interact ferromagnetically with each other due to a strong intra-zigzag edge exchange interaction with exchange integral $J_0 \sim 10^3$ K. Furthermore, the inter-edge interaction is medieted by π-electrons and can be either a ferromagnetic or an antiferromagnetic depending on the sign of exchange integral J_1 (*i.e.*, minus for *AFM* state and plus for *FM* state, see Figure 1.4) [13]. The nature of the intertaction between spins on opposite sites is governed by the width of *GNNs*. The transition between *FM* state and *AFM* state is regarded as semiconductor-metal transition [84]. However, it was reported, that transition from an *AFM* to a *FM* regime can be triggered by the presence of line defects [85].

Compared to that, armchair graphene nanoribbons have no midgap states and they are non magnetic. To induce magnetic ordering in *AGNNs* the same

mechanism as dopation, surface addition or functionalization can be used as in the case of graphene sheet.

1.3.4 Functionalization

Another way for imprinting magnetic moments in graphene based nanomaterials is using of functionalization. The most often elements used for covalent functionalization of graphene are hydrogen, oxygen, fluorine *etc.* Covalently modified graphene derivatives are known as graphane, graphene oxide and fluorographene in case of functionalization by hydrogen, oxygen and fluorine respectively [86], [87], [88], [89]. Besides the single elements several molecules as functional groups can be used (*i.e.*, $-$OH, $-$SH, $-$CN, $-$COOH, $-NH_2$, *etc.*)[13], [88], [91], [92].

The covalent functionalization changes hybridization of participating carbon atoms from sp^2 to sp^3 and induce localized magnetic moments. It is believed that appropriate ratio between sp^2 and sp^3 hybridized carbon atoms brings magnetic ordering in graphene structure.

Graphane is a nonmagnetic and wide-gap semiconductor, but the electronic and magnetic properties of graphane can be tune by the defects, especially by partial dehydrogenation and spatial confinement. The hybridization of the edges is found to play key role in defining the size of the *HOMO–LUMO* gap, which can be in range of $3.04 - 7.51$ eV when the hybridization changes from the sp^2 to the sp^3 type [93]. In case of graphane nanoribbons, unpaired and unpassivated dangling bonds at the edges have $1\,\mu_B$ magnetic moment and exhibit antiferromagnetic coupling with adjacent dangling bonds [94]. Further, the H-vacancies have also influence on the size of band gap, but there

is dependence on thier distribution between the two sides of the graphane plane. It is believed that the H-vacancies present only on the one side of graphane plane and located on the neighboring carbon atoms belonging to the same sublattice will be generate ferromagnetic ordering [93]. In addition, magnetism induced by the partial dehydrogenation contains both contributions, the *FM* part and *AFM* part [95].

Graphene oxide exhibits dominantly diamagnetic behavior but localized magnetic moments can be induced by the functionalization. The magnetization of functionalized graphene oxide has diamagnetic, ferromagnetic and also paramagnetic contribution. But different functional groups introduce magnetic moments followed the order from the highest $-$SH, $-$OH, $-$COOH, $-NH_2$ [96].

In case of fluorographene, it is believed that the partial defluorination can induce magnetic ordering. Nevertheless due to low energy of migration barrier, the fluorine atoms have tendency towards clustering and form paramagnetic centers [69]. Magnetic interactions between these paramagnetic centers are mediated by π-electrons but these interactions are weak and in the temperatures above $\sim$ 100 K are overcome by thermal fluctuations. Recently it was reported a discovery of hydroxofluorographene (G(OH)F) with *AFM* ordering at room temperature and *FM* ground state with transition temperature $T_{FM/AFM}$ at $\sim$ 62 K. It is graphene based material prepared from fluorographene by substituting some fluorine atoms by hydroxyl groups. The magnetism is established due to diradical motifs consisting of sp^2 hybridized carbon atoms embedded in an sp^3 matrix and the ability of –OH groups to stabilize magnetically ordered state up to room temperature due to emer-

gence of superexchange interactions [97].

1.4 Theoretical background

It is evident that properties of atoms, molecules, solids, *etc.*, can be obtained by solving Schrödinger equation (*SE*). However solving of *SE* for real systems analytically is almost impossible except a few limited cases. Thus the several approximative ways of solving *SE* are often used. This chapter introduces a brief overview of the theoretical background for the continued discussion.

1.4.1 Many-body problem

The non-relativistic time-independent Schrödinger equation of interacting system can be expressed as

$$H\Psi\left(\mathbf{R},\mathbf{r}\right) = E\Psi\left(\mathbf{R},\mathbf{r}\right), \tag{1.4}$$

where $\Psi\left(\mathbf{R},\mathbf{r}\right)$ is the wavefunction of all electrons depending on the positions of the electrons $\mathbf{r}$ and nuclei $\mathbf{R}$. The Hamiltonian H is given as

$$H = \sum_{I=1}^{L} \frac{\mathbf{p}_I^2}{2M_I} + \sum_{i=1}^{N} \frac{\mathbf{p}_i^2}{2m_i} + \frac{1}{2}\sum_{I\neq J} \frac{Z_I Z_J e^2}{\mid \mathbf{R}_I - \mathbf{R}_J \mid} - \sum_{i,I} \frac{Z_I e^2}{\mid \mathbf{r}_i - \mathbf{R}_I \mid} + \frac{1}{2}\sum_{i\neq j} \frac{e^2}{\mid \mathbf{r}_i - \mathbf{r}_j \mid} \tag{1.5}$$

where e is charge of the electron and Z is an atomic number. The capital letter stands for a nucleus and the small letter stands for electons. Then $\mathbf{p}_I$ ($\mathbf{p}_i$) is momentum of I-th nucleus, i-th electron respectively. Mass of the I-th nuclei (i-th electron) is M_I (m_i). The first and the second term are the kinetic energy of the nuclei and the electrons, respectively. The remaining terms are

the potential energy given by a Coulomb interaction between nucleus and nucleus, electron and nucleus, and electron and electron. Nevertheless, as mentioned in the beginning of this chapter, obtaining analytical solution of *SE* in this form is limited.

The first step in the wide range of possible simplifications is so-called Born-Oppenheimer approximation (also known as adiabatic approximation) [98]. The central idea is that the mass of nuclei is 10^4 to 10^5 times larger than mass of electrons. Accordingly, electrons having the same kinetic energy as nuclei are 10^2 to 10^3 faster than nuclei. Hence, we can assume that electrons can follow the motion of nuclei almost instantly and that the electrons do not change eigenstates as the nuclei move. According to that, we can split up the full Hamiltonian and define an electronic Hamiltonian H_{el} for fixed nuclear coordinates $\{\mathbf{R}\}$ as

$$H_{el}\left(\{\mathbf{R}\}\right) = T_{el} + V_{nucl-nucl} + V_{nucl-el} + V_{el-el} \tag{1.6}$$

and then the *SE* for electrons in fixed positions of nuclei is given as

$$H_{el}\left(\{\mathbf{R}\}\right)\psi\left(r,\{\mathbf{R}\}\right) = E_{el}\left(\{\mathbf{R}\}\right)\psi\left(r,\{\mathbf{R}\}\right). \tag{1.7}$$

The energy $E_{el}\left(\{\mathbf{R}\}\right)$ is taken to be a potentional for motion of nuclei which are assumed to follow *SE* in the form

$$\left\{T_{nucl} + E_{el}\left(\mathbf{R}\right)\right\}\Lambda\left(\mathbf{R}\right) = E_{nucl}\Lambda\left(\mathbf{R}\right) \tag{1.8}$$

Nevertheless, the problem of solving the many body equation for a system of N interacting electrons still remains.

1.4.2 Thomas-Fermi model

Historically, the density functional theory (DFT) has its roots in the Thomas-Fermi model in which the all electron wavefunction ψ is substituted by the electron density $n(r)$ defined as

$$n\left(\mathbf{r}\right)=\sum_{i=1}^{N}\mid\psi_{i}\left(\mathbf{r}\right)\mid^{2} \tag{1.9}$$

which is physical observable [99]. In an inhomogeneous case, for finding the electron density it is required to determine all occupied one-particle wavefunctions obtained by solving the effective one-particle Schrödinger equations

$$\left\{-\frac{\hbar^{2}}{2m}\nabla^{2}+v_{eff}\left(\mathbf{r}\ \right)\right\}\psi_{i}\left(\mathbf{r}\right)=\varepsilon_{i}\psi_{i}\left(\mathbf{r}\right), \tag{1.10}$$

where v_{eff} is effective potential given as

$$v_{eff}\left(\mathbf{r}\right)=v_{ext}\left(\mathbf{r}\right)+\int\frac{n\left(\mathbf{r}'\right)}{\mid\mathbf{r}-\mathbf{r}'\mid}\mathrm{d}\mathbf{r}'. \tag{1.11}$$

Nevertheless this model works only for systems in constant or slowly varying potential. It is worth mentioning that this model neglects exchange and correlation effects.

1.4.3 Density functional theory

Going beyond the Thomas-Fermi model, Hohenberg and Kohn established the connection between the electron density and the many-electron Schrödinger equation, which can be substituted by the many body problem with an independent particle problem, which is considered as heart of density functional theory (DFT).

Hohenberg-Kohn theorems

The *DFT* is standing on the two theorems, which were formulated by Hohenberg and Kohn [100].

Theorem 1 *For any system of interacting particles in an external potential* $v_{ext}(\boldsymbol{r})$*, the potential can uniquely be determined except for a constant, by the ground state particle density* $n_0(\boldsymbol{r})$*.*

Theorem 2 *A universal functional for the energy* $E[n]$ *in terms of the density* $n(\boldsymbol{r})$ *can be defined, valid for any external potential* $v_{ext}(\boldsymbol{r})$*. For any particular* $v_{ext}(\boldsymbol{r})$*, the exact ground state energy of the system is the global minimum value of this functional, and the density* $n(\boldsymbol{r})$ *that minimizes the functional is the exact ground state density* $n_0(\boldsymbol{r})$*.*

Kohn-Sham equations

Following above mentioned Hohenberg-Kohn two theorems, the energy functional is defined as

$$E[n] = T_S[n] + \int v_{ext}(\mathbf{r})\, n(\mathbf{r})\, \mathrm{d}\mathbf{r} + \frac{1}{2}\int \frac{n(\mathbf{r})\, n(\mathbf{r})'}{\mid \mathbf{r} - \mathbf{r}' \mid} \mathrm{d}\mathbf{r}\mathrm{d}\mathbf{r}' + E_{xc}[n], \quad (1.12)$$

where the first term is kinetic energy, the second term is energy coming from external potential, the third term is the classical electrostatic energy (also known as Hartree energy) of the electrons and the last term is exchange correlation energy where are grouped all the many-body effects. By using variational principle for minimizing energy functional with respect to the single particle states under the constrain of normalization, we obtain Kohn-

Sham equations

$$\left\{-\frac{\hbar^2}{2m}\nabla^2 + v_{ext}(\mathbf{r}) + v_H(\mathbf{r}) + v_{xc}(\mathbf{r})\right\}\psi_i(\mathbf{r}) = \varepsilon_i\psi_i(\mathbf{r}), \tag{1.13}$$

where exchange-correlation potential $v_{xc}(\mathbf{r})$ is the functional derivative of the exchange-correlation potentional

$$v_{xc}(\mathbf{r}) = \frac{\delta E_{xc}[n(\mathbf{r})]}{\delta n(\mathbf{r})}. \tag{1.14}$$

Then the ground state energy is given as

$$E = \sum_{i=1}^{N}\varepsilon_i + E_{xc}[n(\mathbf{r})] - \int v_{xc}(\mathbf{r})\, n(\mathbf{r})\, \mathrm{d}\mathbf{r} - V_H - V_{nucl-nucl}. \tag{1.15}$$

Unfortunately, the exact exchange-correlation potentionals are not known, except for the free electron gas, *i.e.* for a system with constant electron density. Thus, several approximations were developed which permit the calculation of physical quantities more or less accurately.

The local density approximation

The most commonly used approximation is the local density approximation (LDA), where the exchange correlation energy for homogeneous electron gas is also used for non-homogeneous systems

$$E_{xc}^{LDA}[n(\mathbf{r})] = \int n(\mathbf{r})\, \varepsilon_{xc}^{LDA}[n(\mathbf{r})]\, \mathrm{d}\mathbf{r}, \tag{1.16}$$

where ε_{xc}^{LDA} is the exchange-correlation energy per particle of a uniform electron gas of density $n(\mathbf{r})$ [101]. Although LDA is a simple approximation, it is accurate in a wide range of problems in solids and solid surfaces, including systems with rapid density variations. Nevertheless, LDA tends to over-binding, *i.e.* binding and cohesive energies turn out to be large compared to experiment. In contrast, it underestimates atomic ground state energies and ionization energies [101], [102].

The generalized gradient approximation

The generalized gradient approximation (GGA) goes beyond the LDA and uses not only the density in the particular point but it takes into account also the derivative of the density at the same coordinate [103]. The exchange correlation functional in GGA is given as

$$E_{xc}^{LDA}\left[n\left(\mathbf{r}\right)\right]=\int n\left(\mathbf{r}\right)\varepsilon_{xc}^{LDA}\left[n\left(\mathbf{r}\right)\right]F_{xc}\left[n\left(\mathbf{r}\right),\left|\nabla n\left(\mathbf{r}\right)\right|\right]\mathrm{d}\mathbf{r}, \tag{1.17}$$

where F_{xc} is the enhancement function, which was later modified to PBE (after the names Perdew, Burke, Ernzerhof) [104]. The over binding problem of LDA is corrected in GGA. Nevertheless, both methods, LDA and GGA fail for example in description of band gap of Mott insulators [105].

Spin-polarized *DFT*

The initial formulation of DFT was not dealing with spin polarization of magnetic systems. This problem is fixed in spin-polarized DFT, where the basic variables are the scalar electron density $n\left(\mathbf{r}\right)$ and the vector of the magnetization density $\mathbf{m}\left(\mathbf{r}\right)$. Instead of those variables, sometimes the spin density matrix $n^{\alpha\beta}\left(\mathbf{r}\right)$ is used, where α and β can have two values, either $\uparrow$ for spin up, or $\downarrow$ for spin down. The relation between $n\left(\mathbf{r}\right)$, $\mathbf{m}\left(\mathbf{r}\right)$ and $n^{\alpha\beta}\left(\mathbf{r}\right)$ is given by

$$n(\mathbf{r})=\sum_{\alpha}n^{\alpha\alpha}(\mathbf{r}) \tag{1.18}$$

$$\mathbf{m}(\mathbf{r})=\sum_{\alpha\beta}\sigma^{\alpha\beta}n^{\alpha\beta}(\mathbf{r}) \tag{1.19}$$

and by

$$n^{\alpha\beta}(\mathbf{r})=\frac{1}{2}\left(n(\mathbf{r})\delta^{\alpha\beta}+m_{x}(\mathbf{r})\sigma_{x}^{\alpha\beta}+m_{y}(\mathbf{r})\sigma_{y}^{\alpha\beta}+m_{z}(\mathbf{r})\sigma_{z}^{\alpha\beta}\right), \tag{1.20}$$

where $\sigma_x, \sigma_y, \sigma_z$, are Pauli spin matrices [106], [107]. The Hohenberg-Kohn-Sham spin density functional is given as

$$E\left[n^{\alpha\beta}(\mathbf{r})\right] = T_s\left[n^{\alpha\beta}(\mathbf{r})\right] + \frac{e^2}{2}\int\int \frac{n(\mathbf{r})n(\mathbf{r}')}{\mid \mathbf{r}-\mathbf{r}' \mid}\mathrm{d}\mathbf{r}\mathrm{d}\mathbf{r}' + \\ + \sum_{\alpha\beta}\int V_{ext}^{\alpha\beta}(\mathbf{r})n^{\alpha\beta}(\mathbf{r})\mathrm{d}\mathbf{r} + E_{xc}\left[n^{\alpha\beta}(\mathbf{r})\right]. \tag{1.21}$$

The minimization of $E\left[n^{\alpha\beta}(\mathbf{r})\right]$ with respect to single particle wavefunctions leads to Kohn-Sham equations

$$-\frac{\hbar^2}{2m}\nabla_{\mathbf{r}}^2\varphi_i^{\alpha}(\mathbf{r}) + \sum_{\beta} V_{eff}^{\alpha\beta}(\mathbf{r})\varphi_i^{\alpha}(\mathbf{r}) = \varepsilon_i\varphi_i^{\alpha}(\mathbf{r}), \tag{1.22}$$

where ε_i is Lagrange parameter related to normalization of wavefunctions $\sum_{\alpha}\langle\varphi_i^{\alpha} \mid \varphi_i^{\alpha}\rangle = 1$ [108]. The potential $V_{eff}^{\alpha\beta}(\mathbf{r})$ is given as

$$V_{eff}^{\alpha\beta}(\mathbf{r}) = \delta^{\alpha\beta}e^2\int\frac{n(\mathbf{r}')}{\mid \mathbf{r}-\mathbf{r}' \mid}\mathrm{d}\mathbf{r}' + V_{ext}^{\alpha\beta}(\mathbf{r}) + V_{xc}^{\alpha\beta}(\mathbf{r}) \tag{1.23}$$

and in the case of applied external magnetic field $\mathbf{H}$, the term of external potential will contain magnetic contribution $-(\pm\mu_B\mathbf{H})$. The exchange correlation potential is again given as functional derivative of the exchange correlation energy

$$V_{xc}^{\uparrow\downarrow}(\mathbf{r}) = \frac{\delta E_{xc}\left[n^{\uparrow}(\mathbf{r}), n^{\downarrow}(\mathbf{r})\right]}{\delta n^{\uparrow\downarrow}(\mathbf{r})}. \tag{1.24}$$

As in the case od classical *DFT*, functional E_{xc} and $V_{xc}^{\uparrow\downarrow}$ are in the most case not known and local-spin density approximation or generalized gradient approximation have to be used [109], [110], [111].

The Bloch's theorem and k-points sampling

The methods discussed above are applicable for atoms and molecules, *i.e.* for systems with finite number of electrones. For solid systems it is needed

to handle with infinite number of electrons and *DFT* approximation cannot be used directly. In solids, one assumes the homogeneity of the system in all directions and therefore there are introduced periodic boundary conditions. Due to this periodicity, the effective potential must be also periodic

$$V_{eff}\left(\mathbf{r}+\ \mathbf{R}\right)=V_{eff}\left(\mathbf{r}\right), \tag{1.25}$$

where $\mathbf{R}$ is translation vector. According to the Bloch's theorem [112], the single particle wavefunctions can be written as

$$\psi_{i,\mathbf{k}}\left(\mathbf{r}\right)=e^{i\mathbf{k}.\mathbf{r}}u_{i,\mathbf{k}}\left(\mathbf{r}\right), \tag{1.26}$$

where i is a band index, $\mathbf{k}$ is a wavevector confined to the first Brillouin zone of the reciprocal lattice and $u_{i,\mathbf{k}}\left(\mathbf{r}\right)$ is a periodic function of the crystal (i.e. $u_{i,\mathbf{k}}\left(\mathbf{r}\right)=u_{i,\mathbf{k}}\left(\mathbf{r}+\mathbf{R}\right)$). Consequently by using the Bloch's theorem the problem with infinite number of electrons can be simplified to a problem with finite number of electrons within a single primitive unit cell. In periodic systems the wavefunctions can be expanded in the planewave basis set

$$\psi_{i,\mathbf{k}}\left(\mathbf{r}\right)=\sum_{\mathbf{G}}c_{i,\mathbf{k}+\mathbf{G}}e^{i(\mathbf{k}+\mathbf{G}).\mathbf{r}}, \tag{1.27}$$

where $\mathbf{G}$ is reciprocal lattice vector. Then, the variational Kohn-Sham orbital can be expressed as linear combination of basis functions ϕ obeying Bloch's theorem,

$$\psi_{i}\left(\mathbf{k},\mathbf{r}\right)=\sum_{j,l\,m\,n}e^{i\mathbf{k}\mathbf{R}_{j,l\,m\,n}}c_{j,l\,m\,n}\left(\mathbf{k}\right)\phi_{j,l\,m\,n}\left(\mathbf{k},\mathbf{r}\right), \tag{1.28}$$

where $c_{j,l\,m\,n}\left(\mathbf{k}\right)$ are expansion coeffients. Analogously to the equation 1.9, the electron density can be expressed as

$$n\left(\mathbf{r}\right)=\sum_{i}\int_{BZ}\mathrm{d}\mathbf{k}\,m_{i}\left(\mathbf{k}\right)\left|\psi_{i}\left(\mathbf{k},\mathbf{r}\right)\right|^{2}, \tag{1.29}$$

where $m_i(\mathbf{k})$ are the occupation numbers of the basis orbitals. It is worth mentioning that integration is done on a finite k-point grid. The proper choice of density of k-point mesh ensures that the integral converges and also that calculations are sufficient to obtain the reasonable accuracy.

The concept of using reciprocal space is reasonable, because differential *SE* in direct space transforms to set of algebraic equations in reciprocal space. Therefore calculations are much easier. And these two spaces are related by simple Fourier transformation. From the perspective of an experimentalist, the reciprocal space is important particularly in diffraction techniques (*i.e.* X-ray, electron or neutron diffraction).

Pseudopotentials

The one of the biggest disadvantages of planewaves is its inefficiency. The wavefunctions near to nucleus are rapidly oscillating and the number of planewaves which are required for their description would be immense. The concept of pseudopotentials is based on assumption that the physical and chemical properties of the systems (*i.e.* atoms, molecules, *etc.*) are mostly dependent on valence electrons [113], [114]. Pseudopotential is a potential of nucleus and core electrons. The wavefunctions of valence electrons outside the core region remain unchanged. The pseudo-wavefunctions must be continuous at the r_c boundary and the same condition is required for their first derivatives as well [116]. The graphical comparison of the wavefunction, pseudo-wavefunction and their potentials is in Figure 1.5.

It is worth mentioning that pseudopotentials are derived from reference state, *i.e.* from exact all-electron calculations of free atoms.

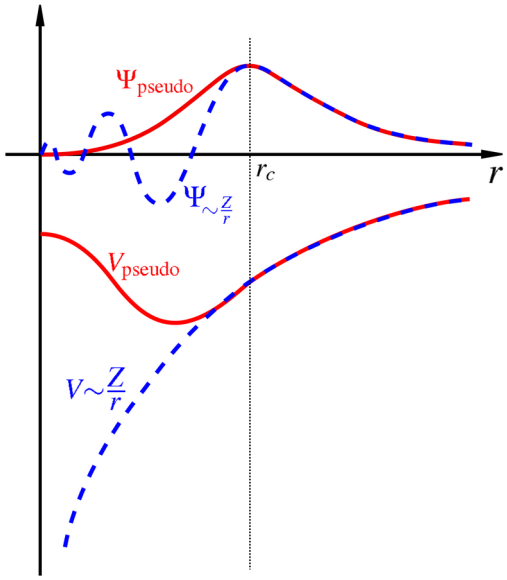

Figure 1.5: The schematic illustration of wavefunction in the electrostatic Coulomb potential of the nucleus (shown in blue) and of pseudo-wavefunction in pseudopotential (shown in red). Reprinted with permisions from Ref. [115].

The projector augmented wave method

The projector augmented wave (PAW) method extends the pseudopotential method [117], [118]. It is based on a linear transformation $\Im$ which transforms quickly converging auxilary pseudo-wavefunction $|\tilde{\psi}_i\rangle$ into the true all-electron wavefunction $|\psi_i\rangle$,

$$|\psi_i\rangle = \Im\,|\tilde{\psi}_i\rangle. \tag{1.30}$$

It is needed to modify the nodal structure in the core region of the all-electron wavefunction which is smooth beyond the r_c. Transformed Kohn-Sham equation can be expressed as

$$\Im^{\dagger} H \Im\,|\tilde{\psi}_i\rangle = \Im^{\dagger}\Im\,|\tilde{\psi}_i\rangle\,\varepsilon_i, \tag{1.31}$$

where $\tilde{H} = \Im^{\dagger} H \Im$ is a pseudo Hamiltonian. The transformation operator can be defined as

$$\Im = 1 + \sum_{R} S_R, \tag{1.32}$$

where R is the atom site index and S_R is the difference between pseudo and all ellectron wavefunctions which are non-zero only in the core region because beyond the r_c pseudo-wave function perfectly matches with all-electron wavefunction. Pseudo-wavefunctions can be expand into pseudo-partial waves in the core region

$$|\tilde{\psi}\rangle = \sum_{i \in R} c_i |\tilde{\phi}_i\rangle. \tag{1.33}$$

For every partial wave exist an auxiliary pseudo-partial wave connect by transformation $\Im$

$$|\phi_i\rangle = (1 + S_R)|\tilde{\phi}_i\rangle. \tag{1.34}$$

Any arbitrary pseudo wavefunction can be written in the pseudo-partial waves basis by

$$\tilde{\psi}(\mathbf{r}) = \sum_{i \in R} \tilde{\phi}_i(\mathbf{r}) c_i = \sum_{i \in R} \tilde{\phi}_i(\mathbf{r}) \langle \tilde{p}_i | \tilde{\psi} \rangle, \tag{1.35}$$

where $|\tilde{p}_i\rangle$ is set of so-called projector functions satisfying completeness

$$\sum_{i \in R} |\tilde{\phi}_i\rangle \langle \tilde{p}_i| = 1 \tag{1.36}$$

and ortogonality

$$\langle \tilde{\phi}_i | \tilde{p}_j \rangle = \delta_{i,j}. \tag{1.37}$$

Now the transformation operator $\Im$ can be written as

$$\Im = 1 + \sum_{i} \left(|\phi\rangle - |\tilde{\phi}_i\rangle \right) \langle \tilde{p}_i| \tag{1.38}$$

where index i goes over the all partial waves corresponding to all atoms. By using the definition of $\Im$ above, the true all-electron wave function can be expressed as

$$|\psi\rangle = |\tilde{\psi}\rangle + \sum_i \left(|\phi_i\rangle - |\tilde{\phi}_i\rangle\right) \langle \tilde{p}_i|\tilde{\psi}\rangle, \tag{1.39}$$

where index i stands for the atomic site R_i , the angular momentum quantum numbers l_i and m_i and the linearization energy ϵ_i. The pseudo-wavefunctions $\tilde{\psi}$ are the variational quantities in *PAW* method which can be expressed by using plane waves

$$\tilde{\psi}_{i,\mathbf{k}}(\mathbf{r}) = \sum_{\mathbf{G}} C_{i,\mathbf{k}+\mathbf{G}} e^{i(\mathbf{k}+\mathbf{G}).\mathbf{r}}. \tag{1.40}$$

As was written above, outside the core region the pseudo-wavefunctions (represented by planewaves) are with good agreement with all-electron wavefunctions, but deviation near the nuclei is significant. Due to this fact, the partial waves were introduced [119]. These partial waves $\tilde{\phi}_i$ are the solution of radial part of *SE* for non-spin polarized reference atom with energy ϵ_i [120].

2 Computational part

2.1 Computational parameters

Our calculations were performed by using the Vienna *ab inition* simulation package (*VASP*), where *SP-DFT* is implemented. By every self-consistent loop the Hamilton is set up with the charge density and the wavefunction is then optimized to get closer to the exact wavefunction. Then, the new wavefunction is used to get a new charge density which is mixed with the old initial charge density and so on (see Figure 2.1). The *PAW* method was used to represent atomic cores and exchange and correlation effects were approximated by *PBE* generalized-gradient approximation.

The cutoff energy was set to 400 eV. The structures were optimized to minimize residual forces under 25 meVÅ^{-1} by using a quasi-Newton algorithm. The optimization calculations were performed with a $3 \times 1 \times 1\,\Gamma$ point-centered Monkhorst-Pack k-point mesh. For the calculations of electronic density of states $30 \times 1 \times 1$ k-point mesh was used. Total magnetic moments are given as a difference between the number of electrons in occupied majority and minority of the spin states. In contrast, local magnetic moments were calculated by integration of local density of states which is given as projection of plane-waves components of all occupied eigenstates on spherical waves inside an atomic sphere. The Bader analysis was used for sep-

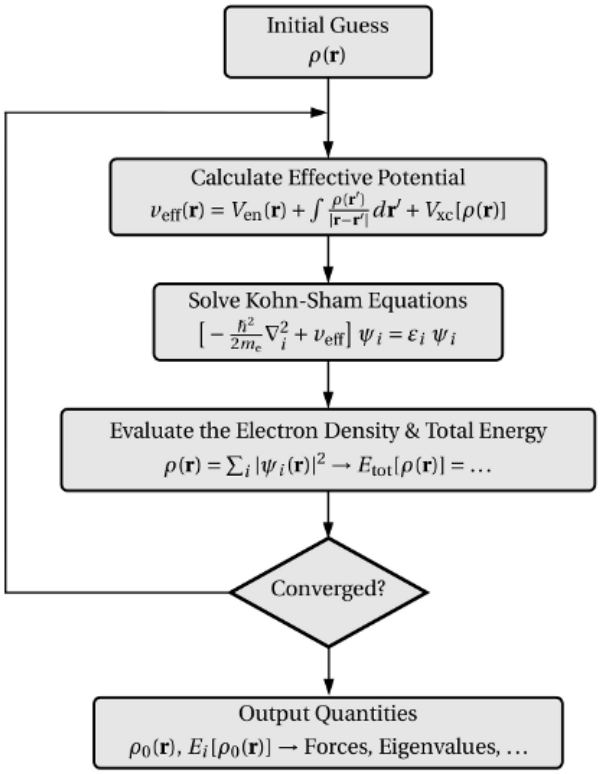

Figure 2.1: Self-consistent cycle. Reprinted with permisions from Ref. [122].

aration of contributions from different atoms in the ground state electronic density. The stability of the structures is given by the formation energy, which is discussed in section 1.3.2. The chemical potentials were approximated by the ground state energy of the free atom in the calculations of the formation energy.

2.2 Pristine nanoribbons

This section reports on calculations of pristine nanoribbons and compares their properties with the literature. Eight structures of armchair nanoribbons having width from 8.4 to 17.02 Å and seven structures of nanoribbons wih

zigzag edges with width from 11.28 to 24.02 Å were simulated.

Table 2.1: Calculated properties of *GNNs* with armchair edges, where E_{bg} (↑) is band gap energy for spin up and E_{bg} (↓) for spin down.

Name	Width [Å]	E_{bg} (↑) [eV]	E_{bg} (↓) [eV]	Total mag. mom.	Local mag. mom. [μ_B]
AGNN7w	8.40	0.579	0.579	0.000	0.000
AGNN8w	9.63	0.541	0.541	0.000	0.000
AGNN9w	10.86	1.094	1.094	0.000	0.000
AGNN10w	12.11	0.463	0.463	0.000	0.000
AGNN11w	13.32	0.455	0.455	0.000	0.000
AGNN12w	14.55	0.904	0.904	0.000	0.000
AGNN13w	15.8	0.386	0.386	0.000	0.000
AGNN14w	17.02	0.388	0.388	0.000	0.000

AGNNs exhibit semiconducting properties with no spin-splitting at the Fermi level, which is in full agreement with the literature [123]. *AGNNs* show an indirect band gaps arising from quantum confinement and increased hopping integral of the π orbitals of the edge atoms caused by small changes in lengths of bonds. There is also no difference in the band gap energy for electrons with different spin (see Table 2.1).

However, the band gap energies do not decrease monotonously with the width of *AGNNs*, as it stands in the literature for the cases of wide nanoribbons [13]. It shows cusps due to strong quantum confinement effect. This behavior was reported and deeply studied in Ref. [124] and our results are in a full agreement.

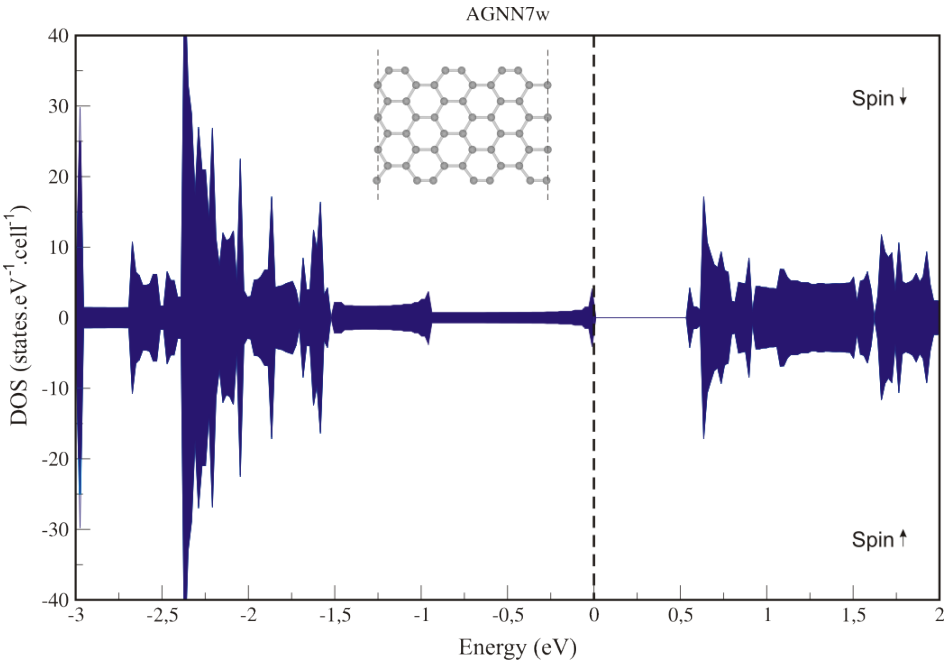

Figure 2.2: Density of states of pristine AGNN7w. Inset shows the structure of AGNN7w. In all figures and tables Fermi energy is set to be zero for better comparison of different structures. DOS plots of all remaining structures, which are not shown in main text, can be found in Section 2.4.3.

ZGNNs are also semiconducting, which is in agreement with the literature (Ref. [125]). With increasing width of *ZGNNs* the energy of band gap changes as can be seen in Figure 2.3. Band gaps in *ZGNNs* are result of staggered sublattice potential from magnetic ordering [123]. The energies of band gap vary slightly for electrons with different spins.

ZGNNs are antiferromagnetic as it was discussed in 1.3.3. The energy difference between ferromagnetic state and antiferromagnetic state ΔE_{FM-AFM} is small and decreases with increasing widths of *ZGNNs*. There is no spin imbalance around the Fermi level as you can see in the Figure 2.4. Figure 2.5 shows that imbalance in spin density is located around edges which interact

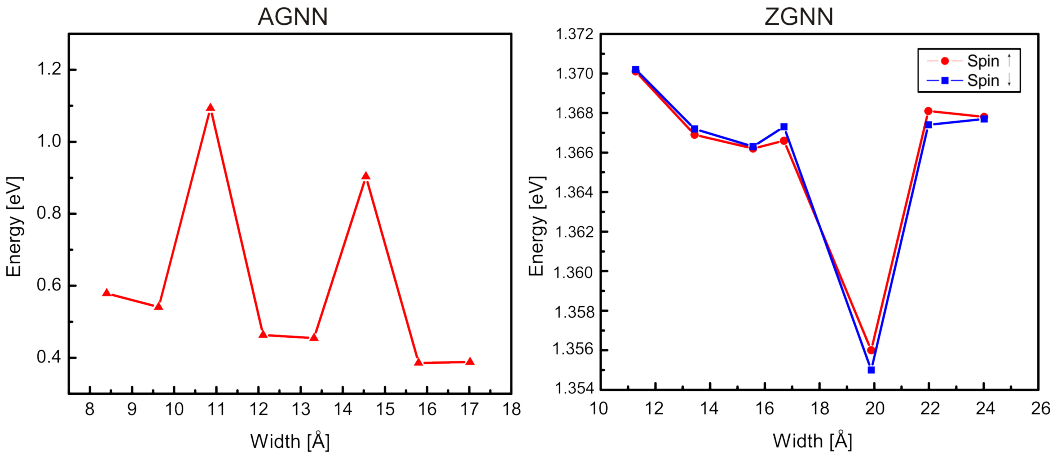

Figure 2.3: The dependence of energy of band gap on the width of *AGNNs* and *ZGNNs*. For further interest see Figure 2 in Ref. [124].

antiferromagnetically. Magnetism of pristine *ZGNNs* is established due to the formation of peculiar edge localized states near Fermi energy and the spins tend to align in a parallel manner on the same sublattice points along the same edge, giving rise to a long-range ferrimagnetic coupling (please, see Section 1.3.3).

Table 2.2: Calculated properties of *GNNs* with zigzag edges, where E_{bg} (↑) is band gap energy for spin up and E_{bg} (↓) for spin down.

Name	Width [Å]	E_{bg} (↑) [eV]	E_{bg} (↓) [eV]	Total mag. mom.	Local mag. mom. [μ_B]	ΔE_{FM-AFM} [eV]
ZGNN6w	11.28	1.370	1.370	0.000	0.000	0.066
ZGNN7w	13.43	1.367	1.367	0.000	0.000	0.051
ZGNN8w	15.57	1.366	1.366	0.000	0.000	0.041
ZGNN9w	16.7	1.366	1.367	0.000	0.000	0.033
ZGNN10w	19.89	1.356	1.355	0.000	0.000	0.027
ZGNN11w	21.98	1.368	1.367	0.000	0.000	0.023
ZGNN12w	24.02	1.368	1.368	0.000	0.000	0.020

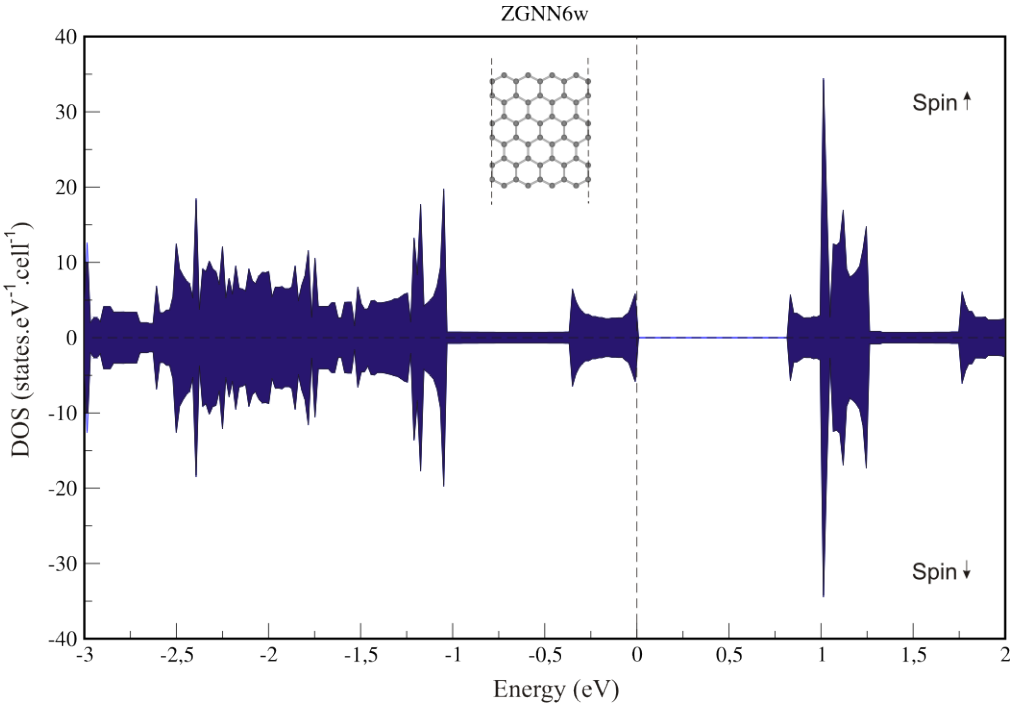

Figure 2.4: Density of states of pristine *ZGNN6w*. Inset shows the structure of *ZGNN6w*.

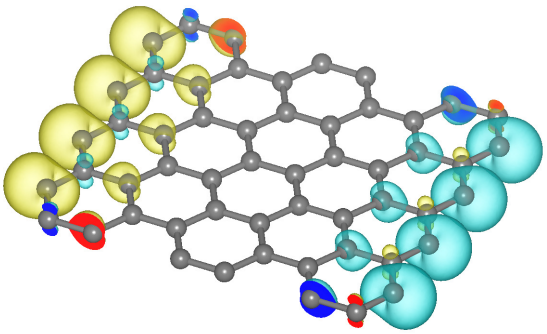

Figure 2.5: Spin density of *ZGNN6w* in the ground state with isosurfaces level at 1×10^{-2} eÅ^{-3}, the spin density for spin up and spin down is represented by yellow and green colors, respectively.

2.3 Pristine nanoribbons with edges passivated by hydrogen

The passivation of edges is often used for stabilization of structures and to avoid any edge reconstruction [127]. We limited our calulations only to symmetric cases of *GNNs* reported in previous chapter.

Table 2.3: Calculated properties of *GNNs* with edges passivated by hydrogen atoms, E_{bg} ($\uparrow$) is band gap energy for spin up and E_{bg} ($\downarrow$) for spin down.

Name	E_{bg} ($\uparrow$) [eV]	E_{bg} ($\downarrow$) [eV]	Total mag. mom.	Local mag. mom. [μ_B]	ΔE_{FM-AFM} [eV]
AGNN8w-H	0.800	0.800	0.000	0.000	-
AGNN10w-H	0.248	0.248	0.000	0.000	-
AGNN12w-H	0.837	0.837	0.000	0.000	-
AGNN14w-H	0.565	0.565	0.000	0.000	-
ZGNN6w-H	0.796	0.796	0.000	0.000	0.038
ZGNN8w-H	0.806	0.805	0.000	0.000	0.026
ZGNN10w-H	0.809	0.810	0.000	0.000	0.018
ZGNN12w-H	0.819	0.820	0.000	0.000	0.015

AGNNs retain their semiconducting properties after edge passivation with no spin-splitting at the Fermi level (see Figure 2.6). As can be seen in Figure 2.7 band gap dependence on the width of *AGNNs* with passivated edges by hydorgen atoms still shows cusps due to strong quantum confinement effect. However, edge passivation changes the nature of the band gap from an indirect to direct. It is due to enhanced interaction between electrons and nuclei near the edge [126].

AGNNs with H-passivated edges remain nonmagnetic. All the above-mentioned results are are in agreement with literature [124]-[126].

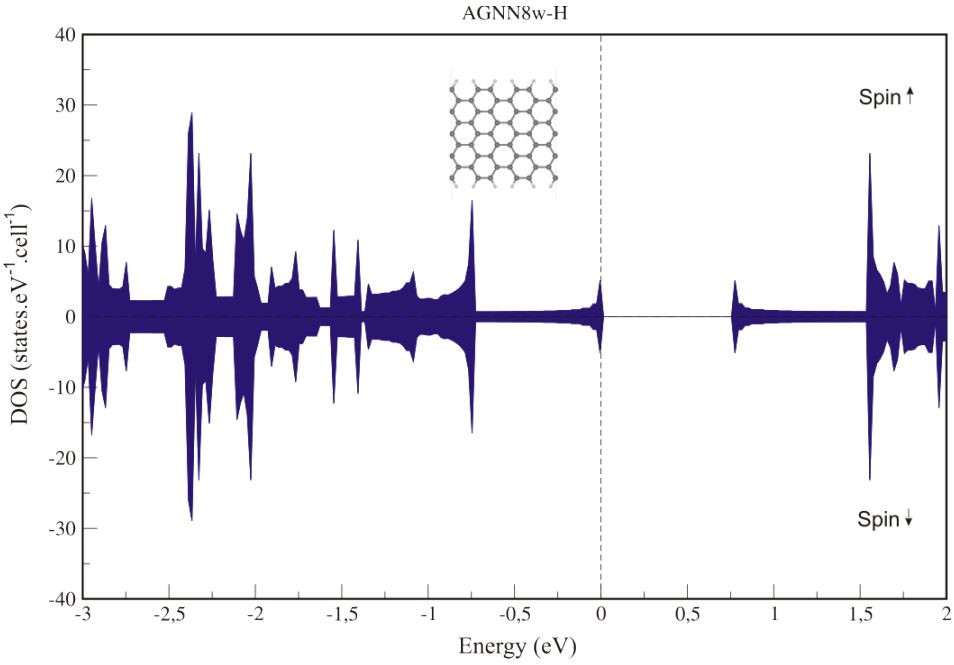

Figure 2.6: Density of states of pristine AGNN8w-H. Inset shows the structure of AGNN8w-H.

ZGNNs with passivated edges also retain their semiconducting properties with no spin-splitting near the Fermi level (Figure 2.8). The band-gap energy of H-passivated *ZGNNs* slowly increases with the widths and there is still slight difference in band-gap energies for opposite spins (Figure 2.7).

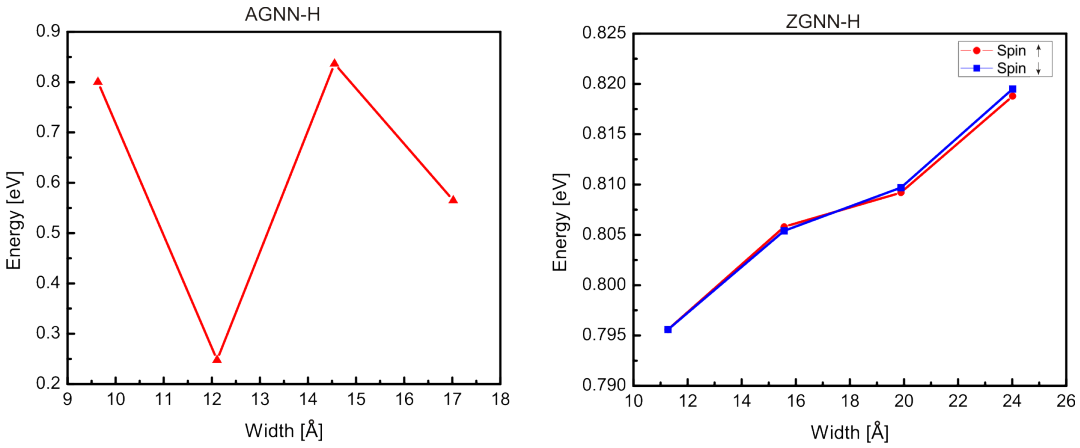

Figure 2.7: The band-gap energy vs. the width of *AGNNs* and *ZGNNs* with edges passivated by hydorgen atoms. For further interest see Figure 2 in Ref. [124].

ZGNNs are still antiferromagnetic after edge passivation which agrees with literature [125]. The energy difference between *FM* and *AFM* state is small and it decreases with the widths of *ZGNNs* (Table 2.3) as it was in the case of *ZGNNs* with bare edges. The spatial spin distributions of the ground state of ZGNN-6w-H is shown in Figure 2.9. The imbalance in spin density is located around edges as in the case of pristine *ZGNNs*.

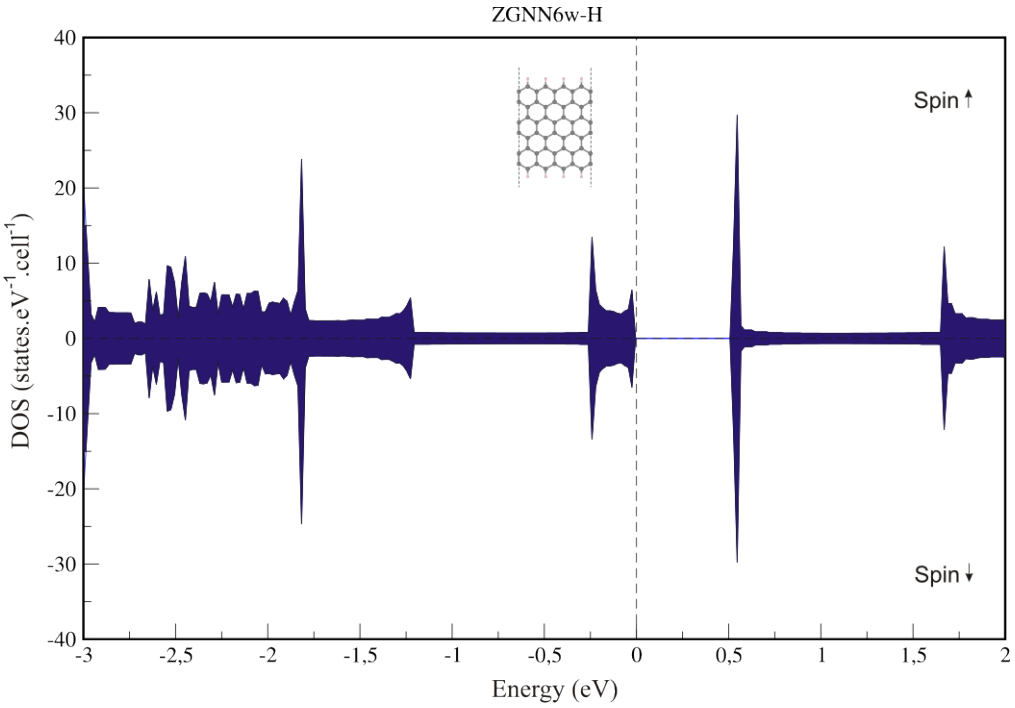

Figure 2.8: Density of states of pristine *ZGNN6w*. Inset shows the structure of *ZGNN6w*.

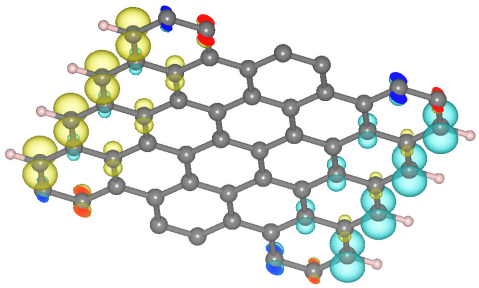

Figure 2.9: Spin density of *ZGNN6w-H* in the ground state with isosurfaces level at 7×10^{-3} eÅ^{-3}, the spin density for spin up and spin down is represented by yellow and green colors, respectively.

2.4 Substitutional doping of graphene nanoribbons by nitrogen and boron atoms

Substitutional doping of the graphene lattice by light elements, boron and nitrogen, has recently attracted particular attantion [6], [78], [79], [80]. For a brief discussion on their influence on the electronic and magnetic properties of graphene we refer the reader to section 1.3.2. Boron, which has one electron less than carbon, behaves as a p-type dopant. On contrary, nitrogen acts as an n-type dopant, when it is substituted in the graphene lattice. Therefore, different influence on physical properties of doped graphene nanoribbons can be expected.

Several configurations of dopant atoms in *GNNs* were considered, which led to interesting magnetic properties in doped graphene [129]. These motifs have been tested in *AGNNs* and *ZGNNs* of different widths and with bare and passivated edges by hydrogen atoms. The following chapters report our results.

2.4.1 2 heteroatoms in configuration A

We started with a simple motif of two hetero atoms in para-position in *GNNs* shown in Figure 2.10. The structures are named accordingly to the number of hetero atoms, dopant elements and a label of configuration and with sH for H-passivated edges. [1].

AGNNs with this configuration of boron atoms remain semiconducting,

[1] As an example the structure AGNN7w-2B-A-sH can be mentioned, where 2B represents two boron atoms in the structure, A is label of motif of dopant atoms and sH stands for edges passivated by hydrogen atoms.

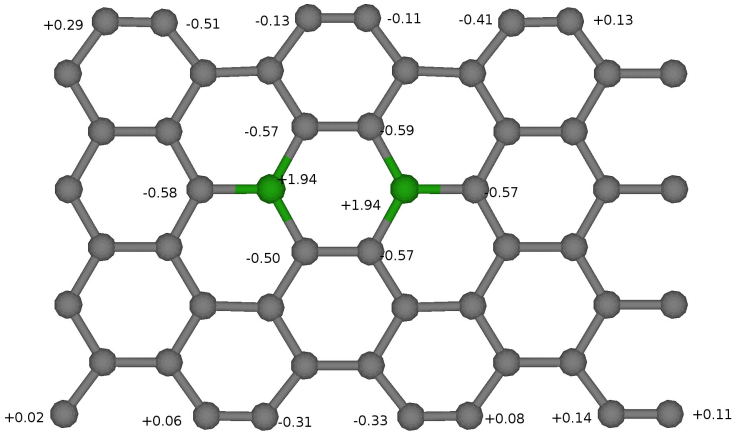

Figure 2.10: AGNN7w with two boron atoms represented by green color in configuration 2B-A. Numbers next to atoms represent calculated Bader charges.

which is unexpected due to p-dopation. These results are in contrast with behavior known for boron-doped graphene reported in literature which became conductive [128].

DOS plot presented in Figure 2.11 look more "discrete" with comparison with DOS plot of pristine AGNN7w shown in Figure 2.2. Using denser k-point mesh did not change the "discrete" character of the DOS plot.

Table 2.4 shows that the width of the band gap changes with the width of AGNNs but no clear dependence has been found. The only structure which exhibits metallic character is AGNN10w-2B-A which has been confirmed by calculations employing denser k-point mesh (DOS plot can be seen on Figure 2.12). The band gap is shifted to the higher energies with respect to the Fermi level, which corresponds with behavior known from boron-doped graphene [128]. The wider AGNNs with the same configuration of boron atoms in their lattices are again semiconductive. Therefore AGNN10w-2B-A is not a

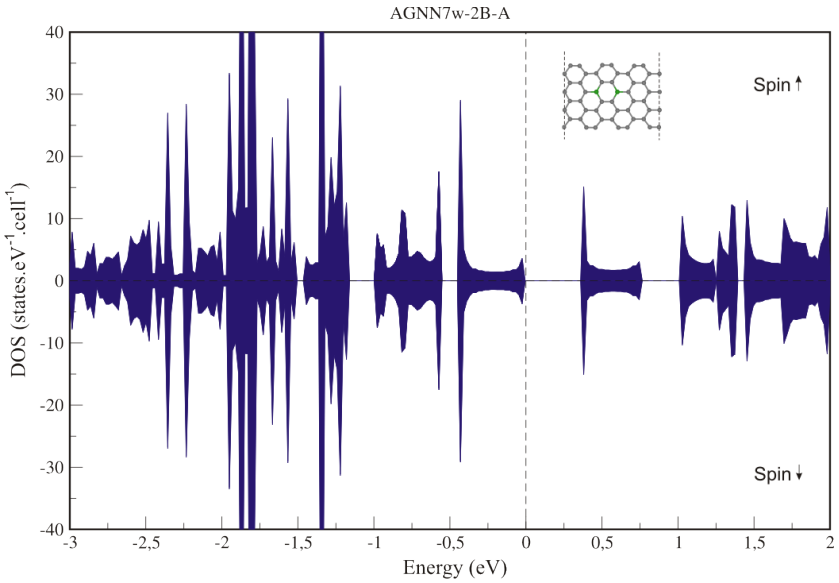

Figure 2.11: Density of states of AGNN7w-2B-A. Inset shows the structure of AGNN7w-2B-A.

borderline for semiconducting and metallic behavior.

The Bader charge analysis of AGNN7w-2B-A (Figure 2.10) shows significant charge transfer in the area around boron atoms substituted in the lattice. Boron atoms are positively charged. On contrary, surrounding carbon atoms have negative charges. This charge transfer is inherent to all *AGNNs* with configuration 2B-A of dopant atoms even in the case of AGNN10w-2B-A, which is the only one conductive.

Conversaly to the AGNNs, all ZGNNs with the same motif of boron atoms (2B-A) are conductive in one spin-channel and they are half-metals (see Figure 2.13). DOS plots of ZGNNs-2B-A shows strong spin splitting near the Fermi level. All *ZGNNs* became ferromagnetic after dopation and magnetic moments are listed in Table 2.4. Figure 2.13 shows, that imbalance in spin denstity is located around edges as in the case of pristine *ZGNNs*.

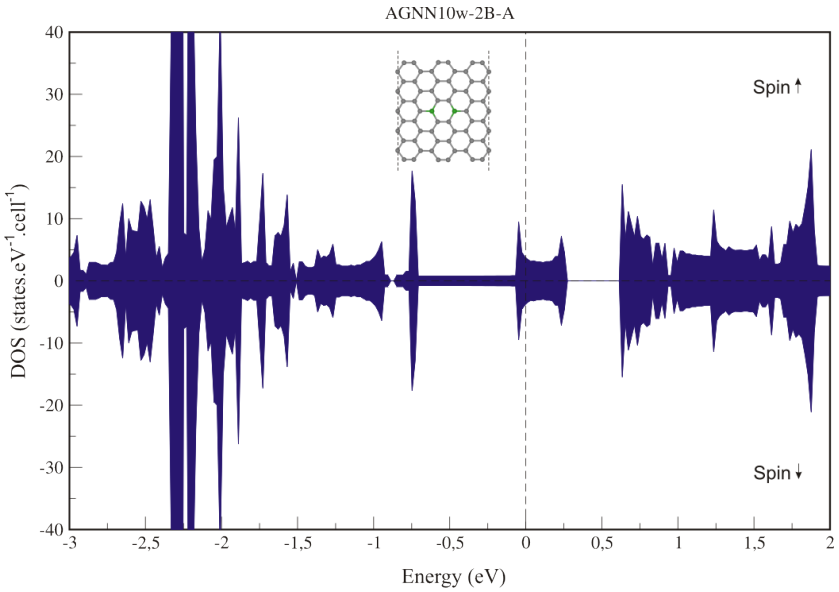

Figure 2.12: Density of states of AGNN10w-2B-A. Inset shows the structure of AGNN10w-2B-A.

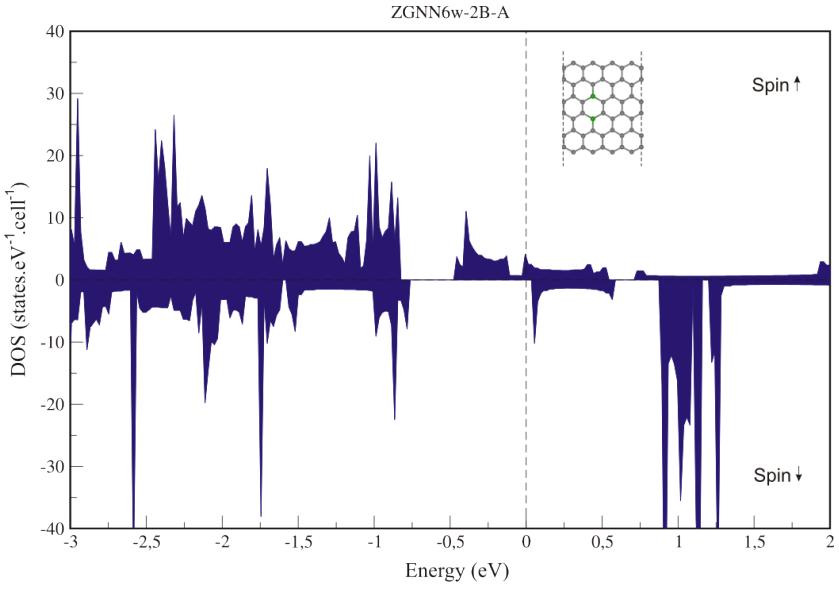

Figure 2.13: Density of states of ZGNN6w-2B-A. Inset shows the structure of ZGNN6w-2B-A.

Table 2.4: Calculated properties of *GNN-2B-A*, E_f is formation energy, E_{bg} (↑) is band gap energy for spin up and E_{bg} (↓) for spin down.

Name	E_f [eV]	E_{bg} (↑) [eV]	E_{bg} (↓) [eV]	Total mag. mom.	Local mag. mom. [μ_B]
AGNN7w-2B-A	2.32	0.777	0.777	0.000	0.000
AGNN8w-2B-A	2.38	1.354	1.354	0.000	0.000
AGNN10w-2B-A	2.65	-	-	0.000	0.000
AGNN11w-2B-A	2.63	0.555	0.555	0.000	0.000
AGNN12w-2B-A	2.65	0.193	0.193	0.000	0.000
AGNN13w-2B-A	2.59	0.489	0.489	0.000	0.000
AGNN14w-2B-A	2.57	0.898	0.898	0.000	0.000
ZGNN6w-2B-A	2.44	-	-	10.000	5.699
ZGNN8w-2B-A	2.59	-	-	10.000	5.685
ZGNN10w-2B-A	2.61	-	-	10.000	5.681
ZGNN12w-2B-A	2.65	-	-	10.000	5.679

The formation energy varies within 12% (*AGNNs*) and 10% (*ZGNNs*) with the ribbons width as it stands in Table 2.4. The positive value of formation energy represent endotermic process of the preparation of these structures.

AGNNs with edges passivated by hydrogen atoms with configuration 2B-A of boron atoms still remain semiconducting except the structure AGNN10w-2B-A-H which is conductive. As in the case of boron-doped AGNNs with bare edges, AGNN10w-2B-A-H cannot be taken as borderline, because wider nanoribbons AGNN12w-2B-A-H and AGNN14w-2B-A-H are semiconducting again.

The band-gap energies are listed in Table 2.4.1. They are changing with the width of *AGNNs* and still show cusps. The band gap energies are the same for electron with both spins and there is no spin splitting near the Fermi level (Figure 2.15). As in the case with bare edges, *AGNNs* with edges passivated by hydrogen atoms with this particular configuration of boron atoms in the lattice are nonmagnetic.

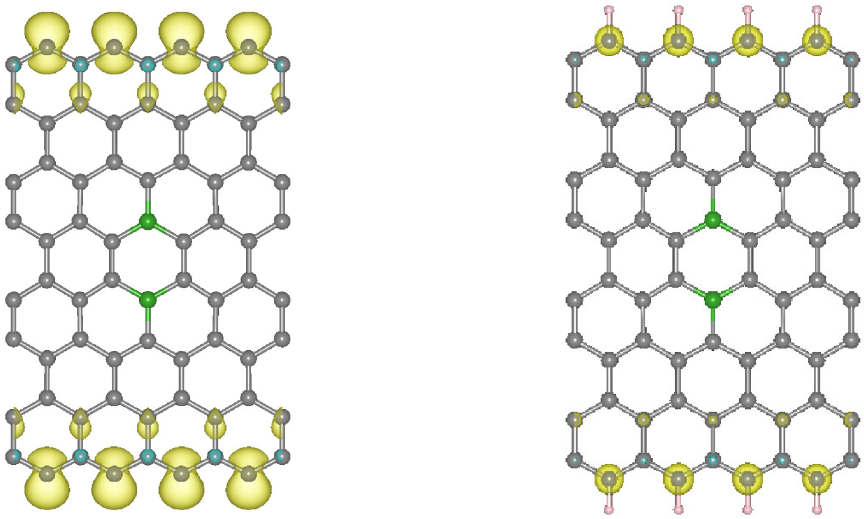

Figure 2.14: Spin density of *ZGNN8w-2B-A* and *ZGNN8w-2B-A-sH* in the ground state with isosurfaces level at 8×10^{-3} eÅ^{-3}. The spin density for spin up and spin down is represented by yellow and green colors, respectively.

However, *ZGNNs* with edges passivated by hydrogen and doped with two boron atoms are conductive in one spin channel with spin splitting near the Fermi level (Figure 2.16). The magnetic moments are suppressed in comparison with non-passivated doped *ZGNNs*. Figure 2.14 shows isosurfaces of spin densities both for doped *ZGNNs* with bare edges and edges passivated by hydrogen atoms.

Table 2.5: Calculated properties of *GNN-2B-A-sH*, E_{bg} ($\uparrow$) is band gap energy for spin up and E_{bg} ($\downarrow$) for spin down.

Name	E_{bg} ($\uparrow$) [eV]	E_{bg} ($\downarrow$) [eV]	Total mag. mom.	Local mag. mom. [μ_B]
AGNN8w-2B-A-sH	1.362	1.362	0.000	0.000
AGNN10w-2B-A-sH	-	-	0.000	0.000
AGNN12w-2B-A-sH	0.345	0.345	0.000	0.000
AGNN14w-2B-A-sH	0.563	0.863	0.000	0.000
ZGNN8w-2B-A-sH	-	-	2.000	1.026
ZGNN10w-2B-A-sH	-	-	1.747	0.905
ZGNN12w-2B-A-sH	-	-	1.932	0.998

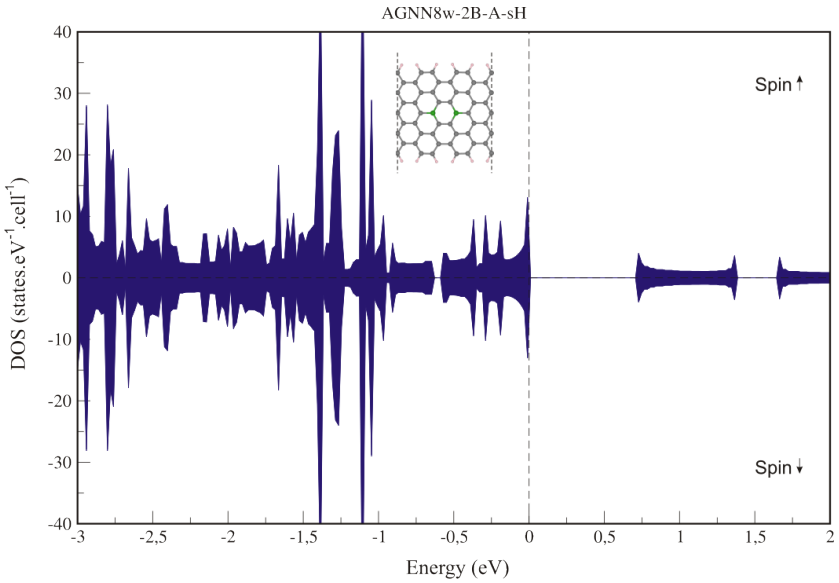

Figure 2.15: Density of states of AGNN8w-2B-A-sH. Inset shows the structure of AGNN8w-2B-A-sH.

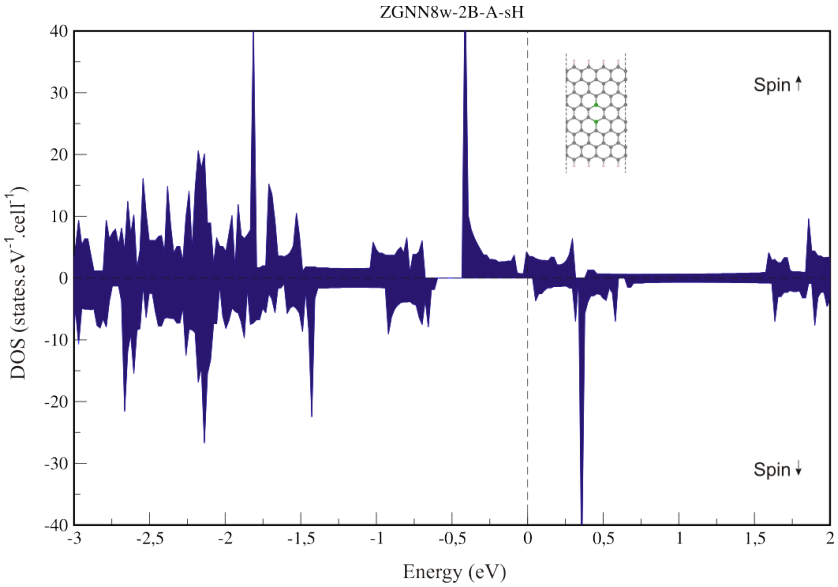

Figure 2.16: Density of states of ZGNN8w-2B-A-sH. Inset shows the structure of ZGNN8w-2B-A-sH.

Next, two nitrogen atoms embedded in the graphene lattice in para position were considered. In contrast to the boron doped *AGNNs*, nitrogen doped *AGNNs* became conductive. This is in agreement with literature on nitrogen doped graphene [128]. Bader charge analysis shows a charge transfer in the area around nitrogen atoms (Figure 2.17). Opposite fenomena to that for boron doped *AGNNs*, were found. This can be expected due to different electronegativity of carbon, boron and nitrogen. Carbon atoms have an electronegativity of 2.55 while boron atoms of about 2.04. Therefore boron atoms are positively charged and the surrounding carbon atoms have negative charge. In case of nitrogen having electronegativity of 3.04 opposite behavior is expected. Nitrogen atoms are negatively charged while the surrounding carbon atoms are positively charged.

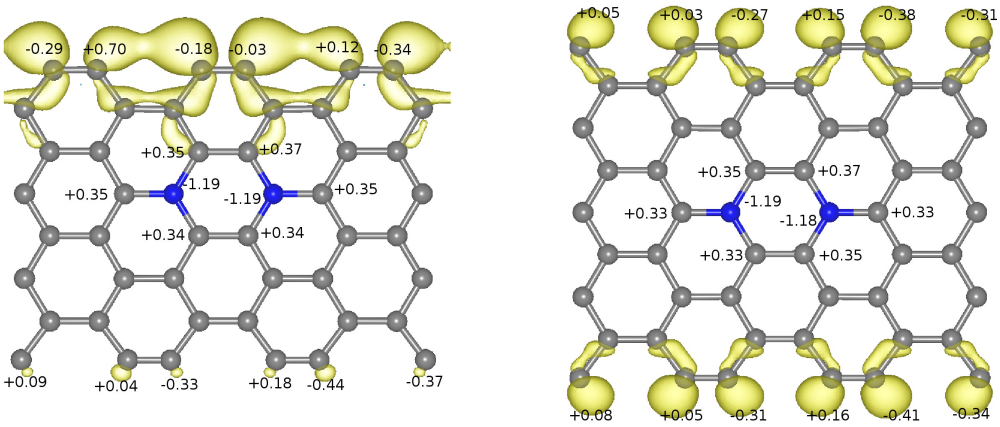

Figure 2.17: Spin density of *AGNN7w-2N-A* (on the left) and *AGNN8w-2N-A* (on the right) in the ground state with isosurfaces level at 5×10^{-3} eÅ^{-3}. Numbers corresponds to the calculated Bader charges The spin density for spin up is represented by yellow color.

The magnetic behavior of nitrogen doped *AGNNs* is quite complex. Nar-

row nitrogen doped *AGNNs* with two N atoms in para configuration (*i.e.*, AGNN7w-2N-A -AGNN11w-2N-A) are ferromagnetic. But wider N-doped *AGNNs* (*i.e.*, AGNN12w-2N-A - AGNN14w-2N-A) are antiferromagnetic. It turned out that there is a dependence on the symmetry and also on the width of the AGNNs. In the case of narrow antisymmetric*AGNNs* (*i.e.*, AGNN7w-2N-A and AGNN11w-2N-A) the spin density have strong imbalance along the edge which is closer to dopant atoms (Figure 2.17). Conversely to that, narrow symmetric AGNNs (*i.e.*, AGNN8w-2N-A and AGNN10w-2N-A) have strong imbalance along both edges which interact ferromagnetically. DOS plots and Bader charge analysis show no differences between symmetric and antisymmetric cases, please see Figure 2.17. Figure 2.18 shows DOS plot of AGNN7w-2N-A with strong spin imbalance at Fermi level. The band gap is shifted in the valence area of energies in comparison with pristine AGNN7w (Figure 2.2). This is in agreament with literature reporting nitrogen doped graphene [128].

In the case of wide symmetric *AGNNs* (*i.e.*, AGNN12w-2N-A and AGNN14w-2N-A), nitrogen atoms and also carbon atoms in the center of the slab are magnetic and interact in an antiferromagnetic manner with both edges, while in antisymetric AGNN13w-2N-A the antiferromagnetic interaction with one edge is preferred (see Figure 2.17). The magnetic moments are listed in Table 2.6. It can be seen that magnetic moments change with the width of *AGNNs*.

While AGNN7w-2N-A is a metal, ZZNN6w-2N-A exhibits semiconducting properties with a band-gap value of 1.012 eV for spin up and 0.326 eV for spin down. This contrasts the electronic properties of boron doped GNNs (please see Figure 2.13). DOS in Figure 2.21 also shows strong spin splitting near

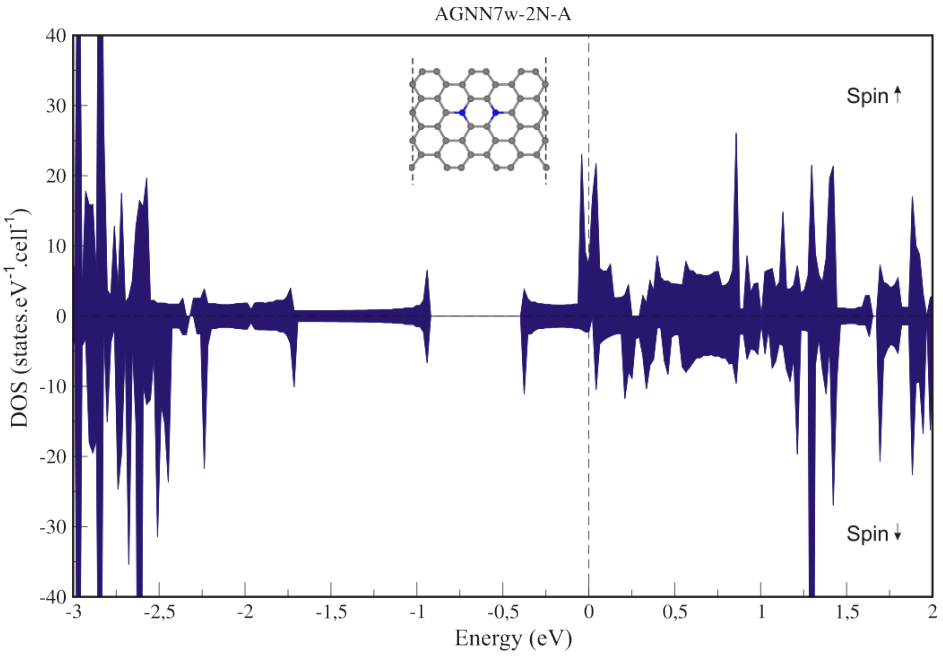

Figure 2.18: Density of states of AGNN7w-2N-A. Insets shows the structure of AGNN7w-2N-A.

the Fermi level which indicates that ZGNNs are magnetic after dopation but the magnetic moments are almost the same as in the case of boron doped *ZGNNs* (see Table 2.4 and Table 2.6).

One can notice that total magnetic moments listed in the Table 2.6 have non-integer value for *AGNNs* and an integer number for *ZGNNs*. It is due to definition of total magnetic moments which is given as a difference between the number of electrons in occupied majority and minority of the spin states (see section 2.1). In case of semiconducting *ZGNNs* having two nitrogen atoms in para-configuration in the structure, all electrons are localized and difference between the number of electrons in occupied majority and minority of the spin states is an integer. Conversely, metallic N-doped *AGNNs* have delocalized electrones, therefore the total magnetic moment cannot be an

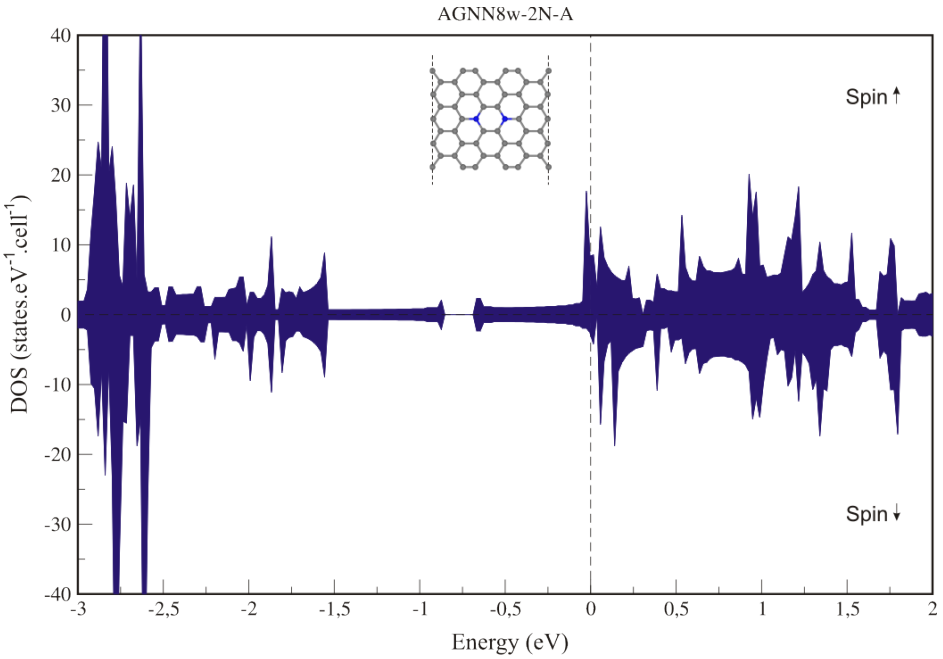

Figure 2.19: Density of states of AGNN8w-2N-A. Insets shows the structure of AGNN8w-2N-A.

integer number.

The formation energy varies only slightly with widths of *AGNNs* and *ZGNNs* as it stands in Table 2.6. The positive value of formation energy represents endotermic process of preparation of these structures as in the case of boron doped *GNNs*.

H-passivation changed the metallic character of AGNNs into semiconducting one. The semiconducting structures shows no spin splitting near the Fermi level (Figure 2.23). *AGNNs* with two nitrogen atoms in the structure and with edges passivated by hydrogen are nonmagnetic.

Interestingly enough, hydrogen passivated *ZGNNs* containing two nitrogen atoms in para-configuration are half-metaliic, *i.e.*, the only one spin channel is metallic as you can see in Figure 2.24. On contrary above mentioned

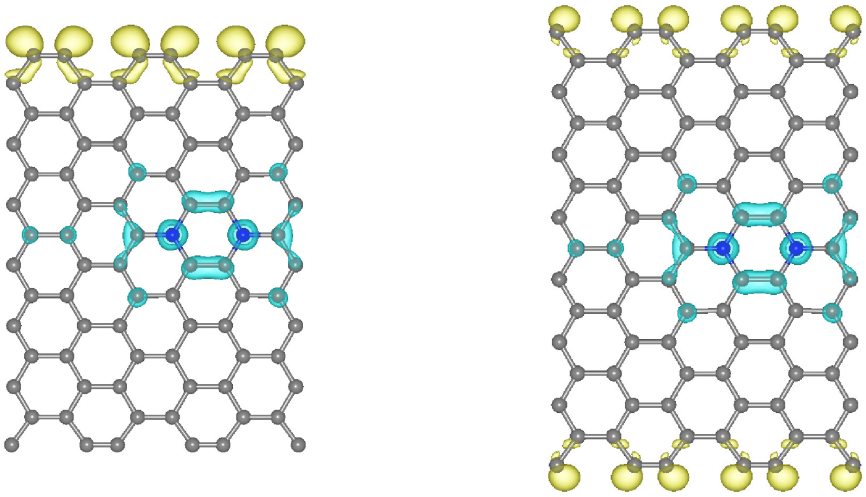

Figure 2.20: Spin density of *AGNN13w-2N-A* and *AGNN14w-2N-A* in the ground state with isosurfaces level at 3×10^{-4} eÅ^{-3}. The spin density for spin up and spin down is represented by yellow and green colors, respectively.

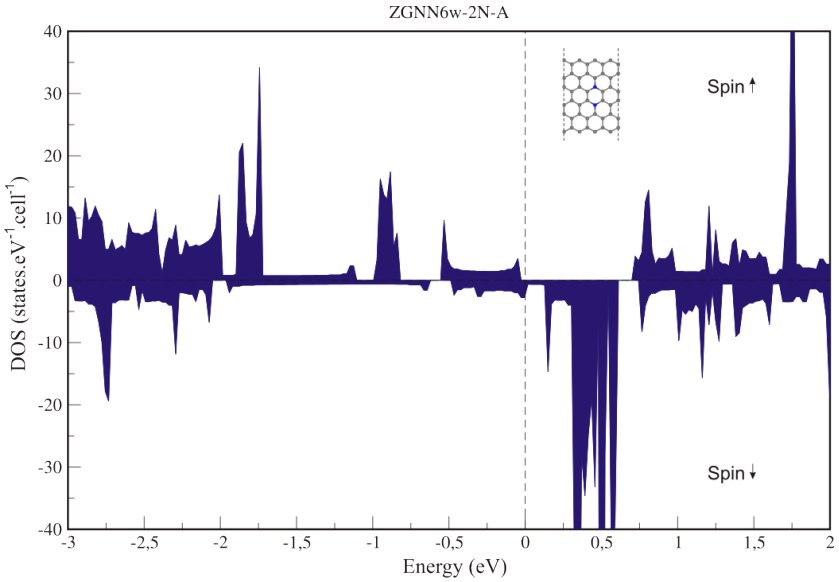

Figure 2.21: Density of states of ZGNN6w-2N-A. Inset shows the structure of ZGNN6w-2N-A.

Table 2.6: Calculated properties of *GNN-2N-A*, E_f is formation energy, E_{bg} (↑) is band gap energy for spin up and E_{bg} (↓) for spin down.

Name	E_f [eV]	E_{bg} (↑) [eV]	E_{bg} (↓) [eV]	Total mag. mom.	Local mag. mom. [μ_B]
AGNN7w-2N-A	3.61	-	-	0.430	0.227
AGNN8w-2N-A	3.54	-	-	0.295	0.152
AGNN10w-2N-A	3.69	-	-	0.184	0.096
AGNN11w-2N-A	3.65	-	-	0.589	0.330
AGNN12w-2N-A	3.66	-	-	0.000	-0.006
AGNN13w-2N-A	3.56	-	-	0.000	-0.007
AGNN14w-2N-A	3.73	-	-	0.000	-0.009
ZGNN6w-2N-A	3.46	1.012	0.326	10.000	5.662
ZGNN8w-2N-A	3.48	0.909	1.738	10.000	5.664
ZGNN10w-2N-A	3.48	0.834	0.482	10.000	5.665
ZGNN12w-2N-A	3.51	0.803	0.558	10.000	5.665

N-doped *ZGNNs* with bare edges are semiconducting. H-passivated *ZGNNs* are magnetic after dopation by nitrogen atoms and magnetic moments are fairly the same as in the case of boron doped *ZGNNs* with passivated edges. Spin densities of ZGNN8w-2N-A and ZGNN8w-2N-A-sH are shown in Figure 2.20.

Table 2.7: Calculated properties of *GNN-2N-A-sH*, E_{bg} ($\uparrow$) is band gap energy for spin up and E_{bg} ($\downarrow$) for spin down.

Name	E_{bg} ($\uparrow$) [eV]	E_{bg} ($\downarrow$) [eV]	Total mag. mom.	Local mag. mom. [μ_B]
AGNN8w-2N-A-sH	1.328	1.328	0.000	0.000
AGNN10w-2N-A-sH	0.951	0.951	0.000	0.000
AGNN12w-2N-A-sH	0.353	0.353	0.000	0.000
AGNN14w-2N-A-sH	0.855	0.855	0.000	0.000
ZGNN8w-2N-A-sH	-	-	2.000	1.034
ZGNN10w-2N-A-sH	-	-	1.808	0.918
ZGNN12w-2N-A-sH	-	-	2.000	1.025

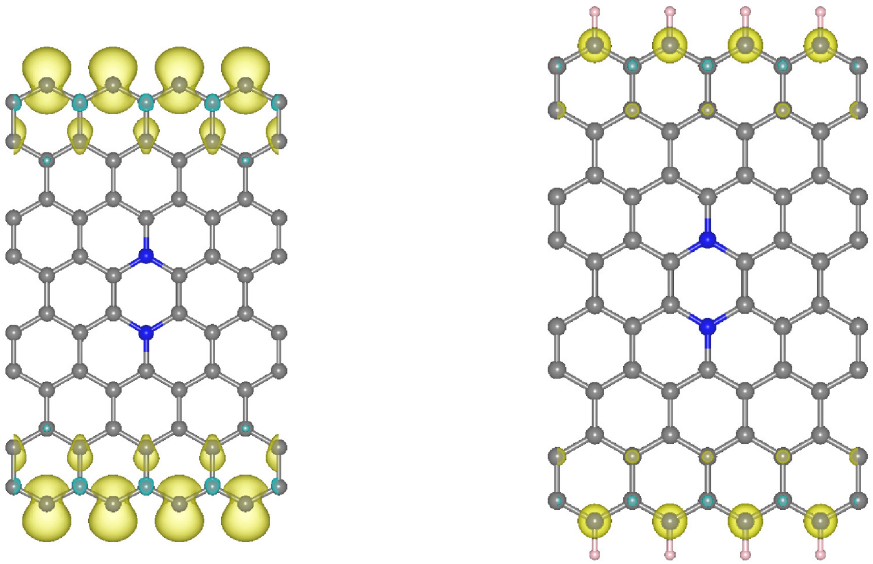

Figure 2.22: Spin density of *ZGNN8w-2N-A* and *ZGNN8w-2N-A-sH* in the ground state with isosurfaces level at 7×10^{-3} eÅ^{-3}. The spin density for spin up and spin down is represented by yellow and green colors, respectively.

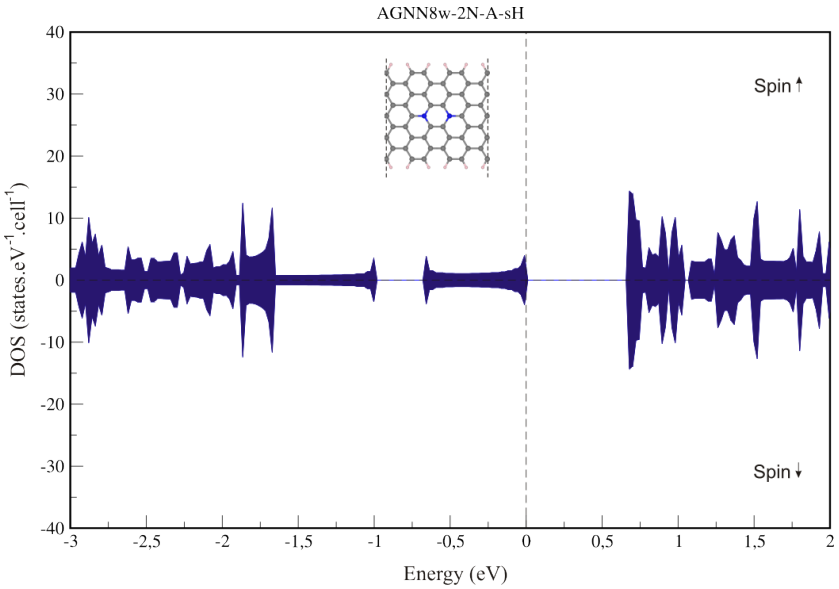

Figure 2.23: Density of states of AGNN8w-2N-A-sH. Inset shows the structure of AGNN8w-2N-A-sH.

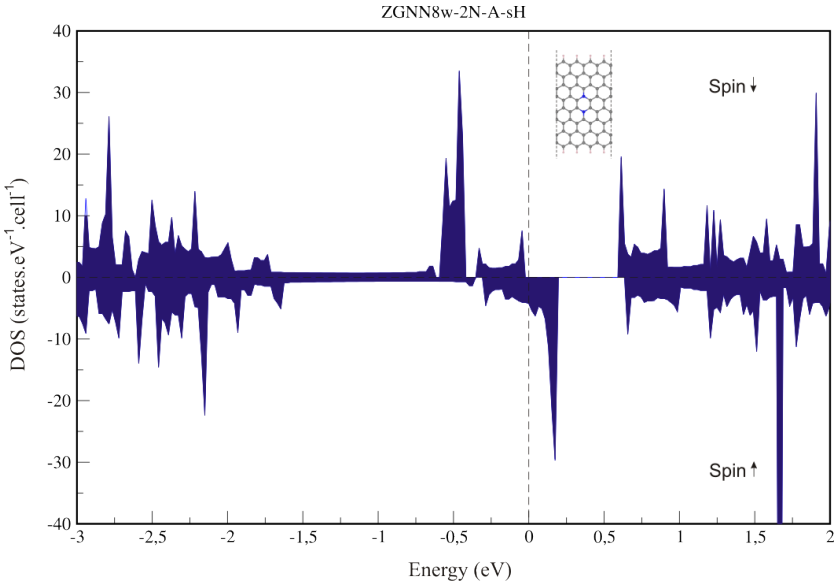

Figure 2.24: Density of states of ZGNN8w-2N-A-sH. Inset shows the structure of ZGNN8w-2N-A-sH.

In summary, this chapter reports our results of GNNs containing two boron and nitrogen atoms in para-configuration in the structure.

Boron doped *AGNNs* with bare edges and also with edges pasivated by hydrogen are semiconductive with different width of band gap but no clear trend of such behavior was found. The only one structure which exhibits metallic behavior is AGNN10w-2B-A. It remains metallic even after edge passivation. Because the wider *AGNNs* are again semiconductive, AGNN10w-2B-A cannot be considered as a borderline betwen the semiconductive and the metallic behavior. DOS plots of all tested AGNNs with two boron atoms in para-configuration show no spin splitting near the Fermi level and are non-magnetic. B-doped *ZGNNs* became half-metallic, the only one spin channel is conductive and this behavior remains unchanged even after edge passivation by hydrogen atoms.

AGNNs with two nitrogen atoms in para-position are conductive. The magnetic behavior is quite complex. It turns out that the key role is played not only by the width but also by the symmetry of *AGNNs* as it is discussed above. In the narrow symmetric cases the imbalance in spin density is located along both edges. On contrary, in case of narrow antisymmetric arrangements only the edge closer to the nitrogen atoms is magnetic. Wider *AGNNs* are antiferromagnetic and there is also the dependence on the symmetry of *AGNNs*. *AGNNs* with H-passivated edges became semiconductive and the magnetism was totally suppressed in all symmetric and antisymmetric *AGNNs*. *ZGNNs* with two N-atoms in para position are semiconducting but after edge passivaton they became half-metallic. Magnetic momets of nitrogen doped *ZGNNs* with bare and passivated edges are nearly the same

as in the case of boron doped *ZGNNs*.

2.4.2 3 heteroatoms in configuration C

Another motif of dopant atoms in *GNNs* which has been tested is three dopant atoms in triangular configuration denoted by "C" and shown in Figure 2.25.

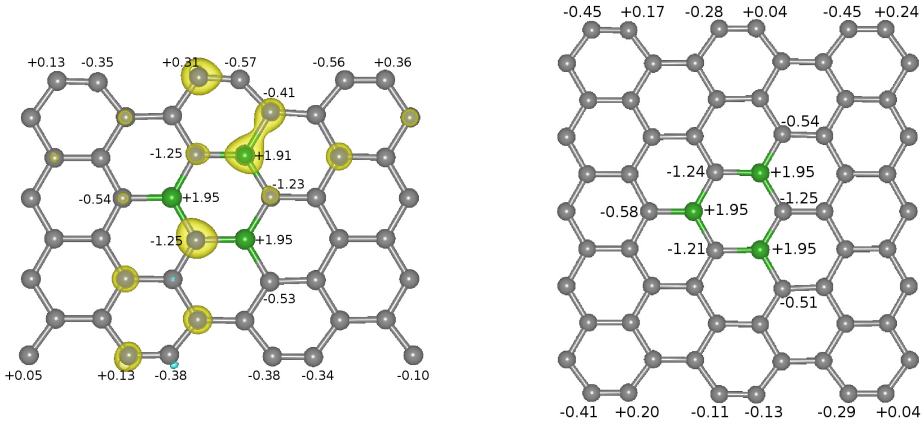

Figure 2.25: (Left) Spin density of AGNN7w-3B-C in the ground state with isosurfaces level at 4×10^{-3} eÅ^{-3}. The spin density for spin up is represented by yellow. (Right) structure of AGNN10w-3B-C. Numbers next to atoms represent calculated Bader charges.

The electronic properties of *AGNNs* with three boron atoms in this triangular configuration are dependent on the width of nanoribbons. Narrow nanoribbons AGNN7w-3B-C and AGNN8w-3B-C are half-metals (Figure 2.26). However, all wider *AGNNs* have metallic character as it is shown in Figure 2.27, which is in agreement with literature on B-doped graphene [128]. It can be recalled that the *AGGN*s with two boron atoms in the para-configuration are semiconductive.

Table 2.8: Calculated properties of *GNN-3B-C*, E_f is formation energy, E_{bg} (↑) is band gap energy for spin up and E_{bg} (↓) for spin down.

Name	E_f [eV]	E_{bg} (↑) [eV]	E_{bg} (↓) [eV]	Total mag. mom.	Local mag. mom. [μ_B]
AGNN7w-3B-C	2.62	0.599	0.660	1	0.502
AGNN8w-3B-C	2.71	-	-	1.000	0.508
AGNN10w-3B-C	2.83	-	-	0.000	0.000
AGNN11w-3B-C	2.89	-	-	0.584	0.294
AGNN12w-3B-C	2.95	-	-	1.010	0.503
AGNN13w-3B-C	2.92	-	-	0.794	0.399
AGNN14w-3B-C	2.90	-	-	0.495	0.249
ZGNN6w-3B-C	2.88	-	-	10.593	6.004
ZGNN8w-3B-C	2.97	-	-	11.000	6.189
ZGNN10w-3B-C	2.98	-	-	11.000	6.182
ZGNN12w-3B-C	2.99	-	-	11.053	6.205

The Bader charge analysis of AGNN7w-3B-C (Figure 2.25) shows significant charge transfer in the area around boron atoms substituted in the lattice. As in the previous cases of B-doped nanoribbons, boron atoms are positively charged. On contrary, surrounding carbon atoms have negative charges. This charge transfer is inherent to all *AGNNs* with configuration 3B-C of dopant atoms.

DOS plots show spin splitting near the Fermi level in the case of half-metallic and also in the case of matallic *AGNNs* with three boron atoms in the their structure, which is a sign of magnetism. Magnetic moments are listed in the Table 2.8 and variation in their values show no clear trend

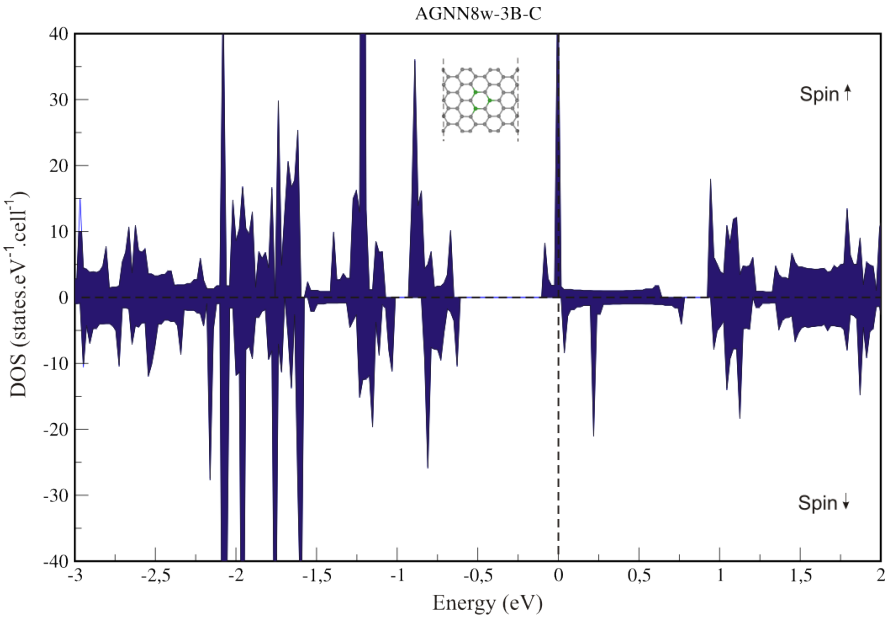

Figure 2.26: Density of states of AGNN8w-3B-C. Inset shows the structure of AGNN8w-3B-C.

with respect to the width of B-doped *AGNNs*. It should be pointed out that magnetic state does not change with the symmetry of *AGNNs* and all structures are ferromagnetic.

The only one nonmagnetic structure is AGNN10w-3B-C and its DOS plot (Figure 2.27) shows no spin splitting near the Fermi level. This behavior remains unchanged even when the denser k-point mesh is applied. The Bader charge analysis shows no difference between magnetic AGNN7w-3B-C and nonmagnetic AGNN10w-3B-C, please see Figure 2.25.

ZGNNs containing three boron atoms arranged in the triangular motif show different electronic properties. The most narrow *ZGNN* is a metal (Figure 2.28) but all wider tested *ZGNNs* have half-metallic character, Figure 2.30. Let us remind the reader that metallic properties have been found

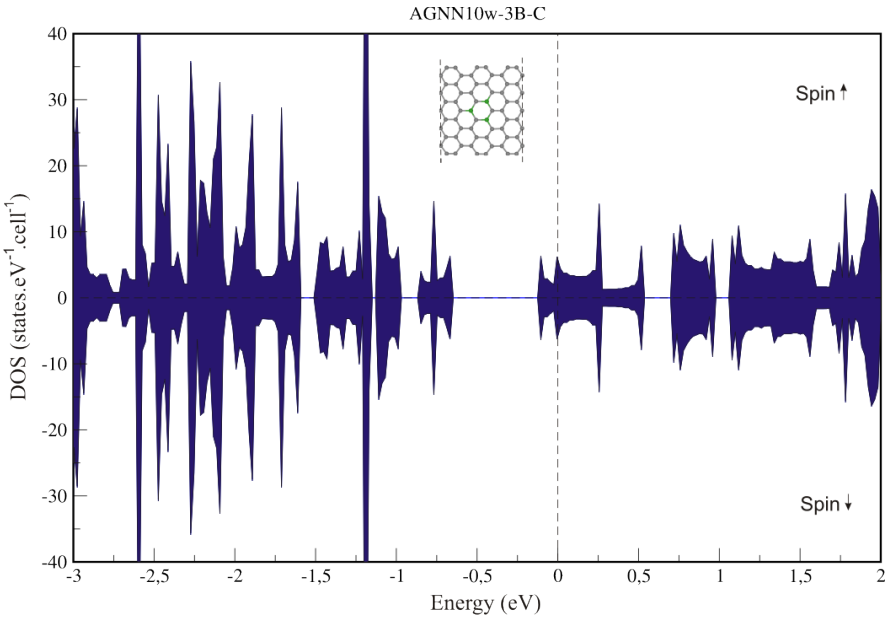

Figure 2.27: Density of states of AGNN10w-3B-C. Inset shows the structure of AGNN10w-3B-C.

in *ZGNNs* containing two boron atoms in para possition.

DOS plots show spin splitting near the Fermi level, which indicates magnetic behavior. Magnetic moments are listed in the Table 2.8 and they slowly increase with the width of *ZGNNs*. All magnetic moments also reach higher values in comparison with magnetic moments of *ZGNNs* containing two boron atoms in para position (Table 2.4). Figure 2.29 shows spin density of ZGNN8w-3B-C which have strong imbalance alog the edges, which is inherent to all pristine and doped *ZGNNs* having bare edges.

The formation energy is nearly the same as in the case of B-doped *GNNs* in para possition (Table 2.4), and varies within 12% (*AGNNs*) and 5% (*ZGNNs*) with the ribbons width as it stands in Table 2.8.

GNNs containing this triangular motif of boron atoms in their structures

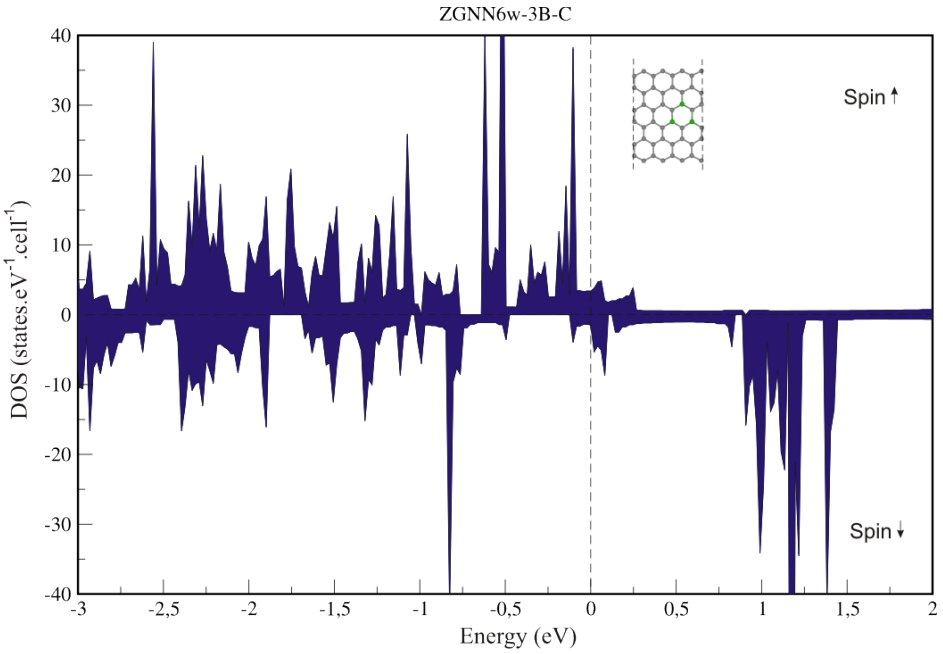

Figure 2.28: Density of states of ZGNN6w-3B-C. Inset shows the structure of ZGNN6w-3B-C.

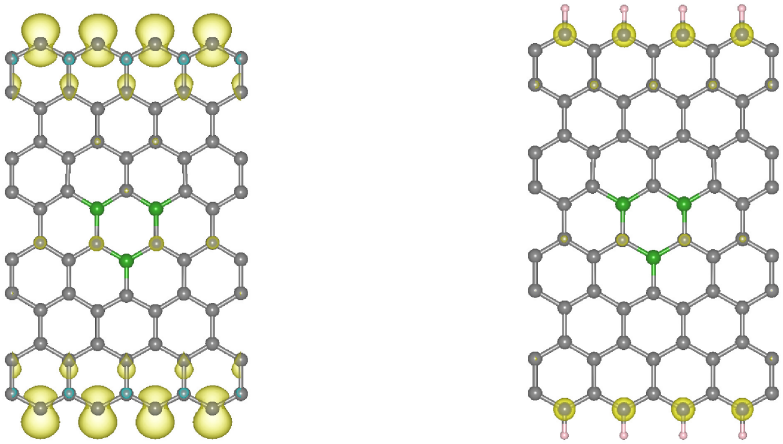

Figure 2.29: Spin density of ZGNN8w-3B-C and ZGNN8w-3B-C-sH in the ground state with isosurfaces level at 1×10^{-2} eÅ^{-3}. The spin density for spin up and spin down is represented by yellow and blue colors, respectively.

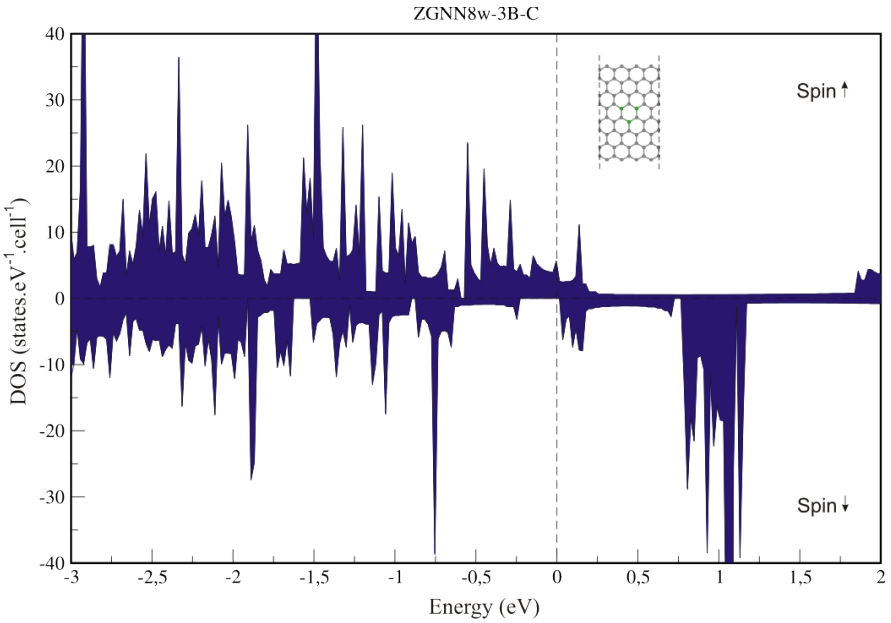

Figure 2.30: Density of states of ZGNN8w-3B-C. Insets show the structure of ZGNN8w-3B-C.

with edges passivated by hydrogen atoms have electronic properties dependent on the width. In case of B-doped *AGNNs*, AGNN8w-3B-C-sH keeps its half-metallic behavior and also AGNN12w-3B-C became half-metallic, see Figure 2.31. Remanining structures (*i.e.* AGNN10w-3B-C-sH and AGNN14w-3B-C-sH) are metals (Figure 2.32). DOS plots of half-metallic structures show more significant spin splitting near the Fermi level in comparison with DOS plots of metal structures. This is in line with higher values of magnetic moments than in the case of metals (Table 2.9). Interestingly enough, structure AGNN10w-3B-C-sH shows different orientation of magnetization and magnetic moments are increased in comparison with remaining passivated *AGNNs* with triangular motif of boron atoms in structure. Figure 2.33 shows comparison of spin densities of AGNN8w-3B-C-sH and AGNN10w-3B-

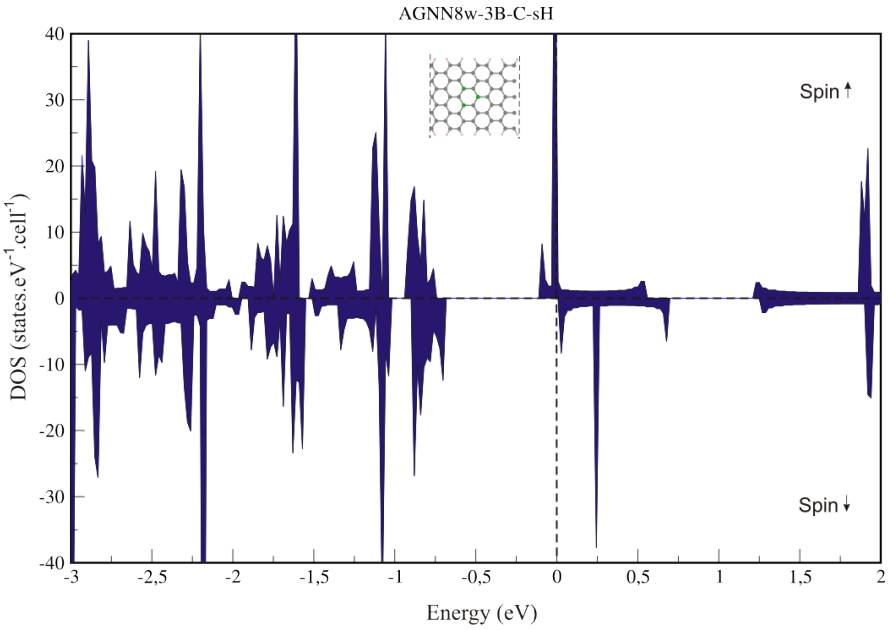

Figure 2.31: Density of states of AGNN8w-3B-C-sH. Inset shows the structure of AGNN8w-3B-C-sH.

C-sH. It can be seen that in the case of AGNN8w-3B-C-sH spin density for spin up dominates. Conversaly, in case of AGNN10w-3B-C-sH the spin density for spin down is dominant. Bader charge analysis of AGNN8w-3B-C-sH and AGNN10w-3B-C-sH show no differences.

ZGNNs with edges passivated by hydrogen atoms and containing the same boron motif in the structure as *AGNNs* discussed above, are metallic. Figure 2.34 shows DOS plot, where one can see spin splitting near the Fermi level, which is sign of magnetism. Magnetic moments are listed in the Table 2.9 and their values increase with the width except the widest ZGNN12w-3B-C-sH, which has magnetic moment slightly decreased. In comparison with the magnetic moments of H-passivated *ZGNNs* having two boron atoms in para position, magnetic moments of H-passivated *ZGNNs* containing three

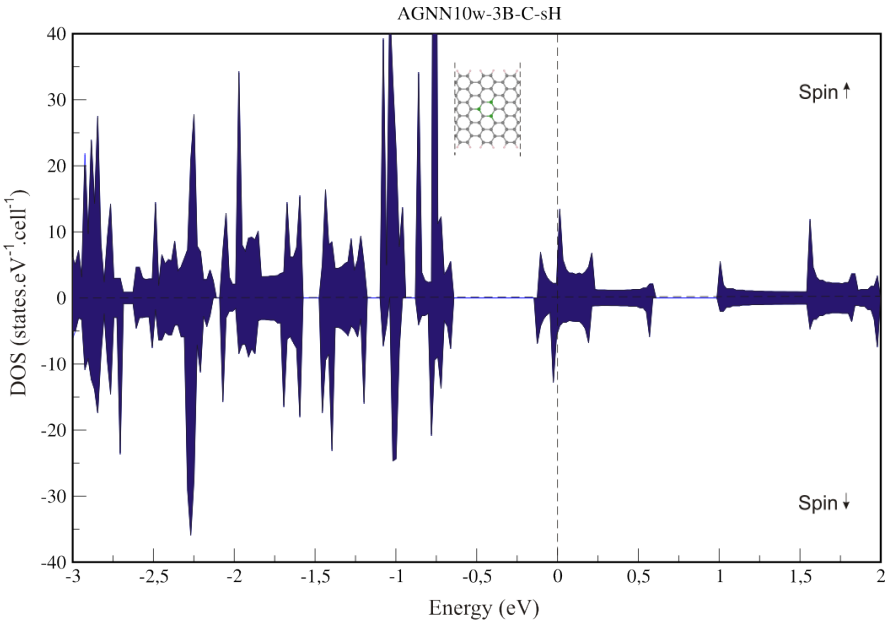

Figure 2.32: Density of states of AGNN10w-3B-C-sH. Inset shows the structure of AGNN10w-3B-C-sH.

Table 2.9: Calculated properties of *GNN-3B-C-sH*, E_{bg} (↑) is band gap energy for spin up and E_{bg} (↓) for spin down.

Name	E_{bg} (↑) [eV]	E_{bg} (↓) [eV]	Total mag. mom.	Local mag. mom. [μ_B]
AGNN8w-3B-C-sH	-	-	1.000	0.495
AGNN10w-3B-C-sH	-	-	-0.189	-0.094
AGNN12w-3B-C-sH	-	-	1.000	0.500
AGNN14w-3B-C-sH	-	-	0.460	0.231
ZGNN6w-3B-C-sH	-	-	1.967	1.001
ZGNN8w-3B-C-sH	-	-	2.666	1.356
ZGNN10w-3B-C-sH	-	-	3.000	1.531
ZGNN12w-3B-C-sH	-	-	2.4373	1.250

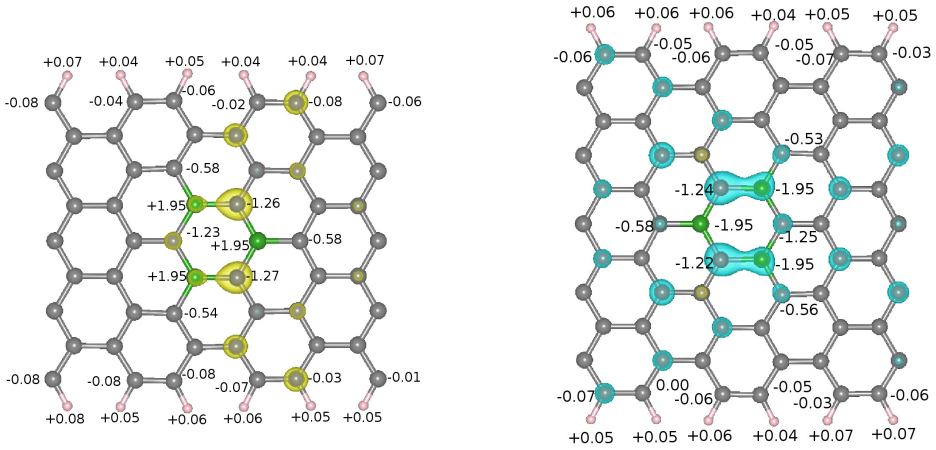

Figure 2.33: (Left) Spin density of AGNN8w-3B-C-sH in the ground state with isosurfaces level at 4×10^{-3} eÅ^{-3}. The spin density for spin up is represented by yellow color. (Right) Spin density of AGNN10w-3B-C-sH in the ground state with isosurfaces level at 5×10^{-4} eÅ^{-3}. The spin density for spin down is represented by blue color. Numbers next to atoms represent calculated Bader charges.

boron atoms in structure reach the higher values, see Table 2.5 and Table 2.9.

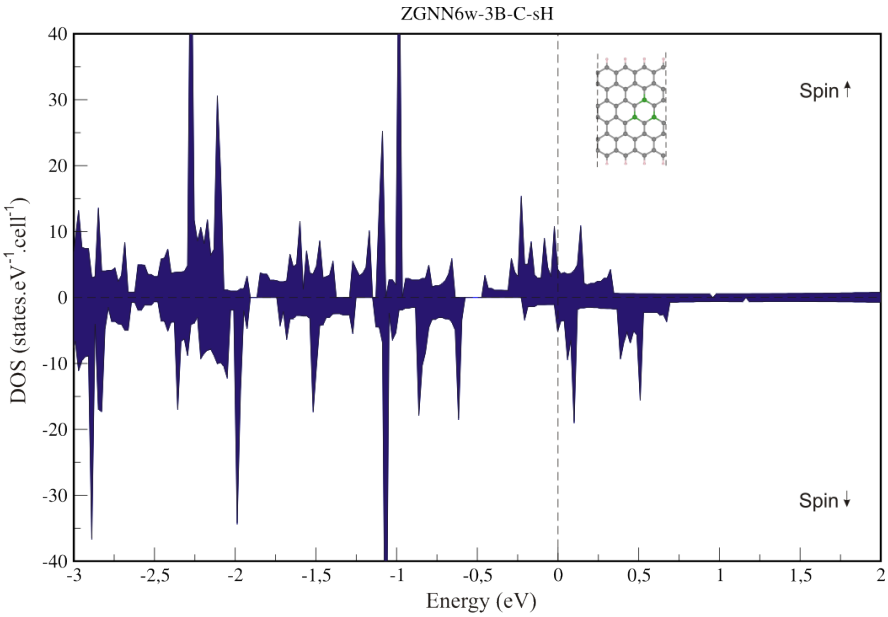

Figure 2.34: Density of states of AGNN10w-3B-C-sH. Inset shows the structure of AGNN10w-3B-C-sH.

Next, the same motif has been tested by using nitrogen as a dopant element. In contrast to the B-doped *AGNNs*, all nitrogen doped *AGNNs* became metallic, see Figure 2.35. This is in full agreement with literature on nitrogen doped graphene [128], [79]. Bader charge analysis shows a charge transfer in the area around nitrogen atoms (Figure 2.36). Nitrogen atoms are negatively charged and carbon atoms have positive charge, which one can expect.

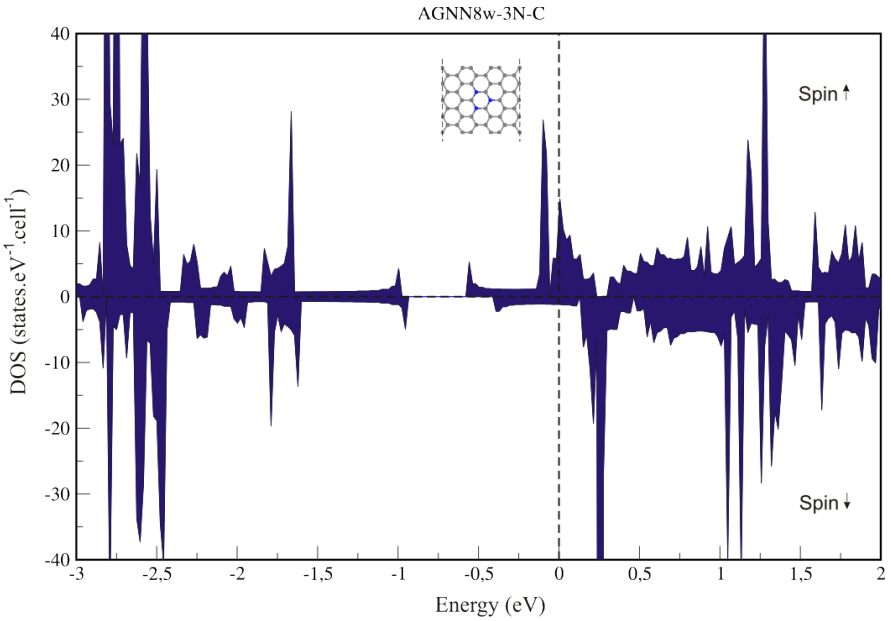

Figure 2.35: Density of states of AGNN8w-3N-C. Inset shows the structure of AGNN8w-3N-C.

DOS plots of all *AGNNs* show strong spin splitting at Fermi level, which indicates magnetic behavior. Magnetic moments, listed in Table 2.10, change with the width of *AGNNs*. From Figure 2.36 it is clearly seen that the strongest imbalance in spin density is around the nitrogen atoms and neighboring carbon atoms. Also edges show imbalance in a spin density. It is worth

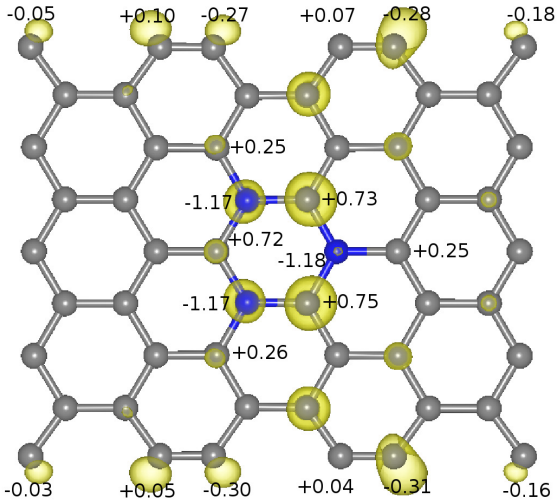

Figure 2.36: Spin density of AGNN8w-3N-C in the ground state with isosurfaces level at 4×10^{-3} eÅ^{-3}. The spin density for spin up is represented by yellow color. Numbers next to atoms represent calculated Bader charges.

mentioning that structure AGNN10w-3N-C exhibits weaker magnetism in comparison with another *AGNNs* containing this triangular motif of nitrogen atoms. DOS plot (Figure 2.37) shows that there is not as significant spin splitting at Fermi level as in the case of AGNN8w-3N-C (Figure 2.35). This remains unchanged even when the denser k-point mesh is applied.

It shloud be pointed out that in the *AGNNs* containing three nitrogen atoms in configuration C there is no dependence on the symmetry of nanoribbons as in the case of *AGNNs* with two nitrogen atoms in the para position.

The most narrow structure ZGNN6w-3N-C is metallic but all wider structures are half-metallic. DOS plots of all N-doped *ZGNNs* show spin imbalance near the Fermi level (Figures 2.38 and 2.39). Magnetic moments (Table 2.10) are nearly the same for all the widths. They are comparable with magnetic

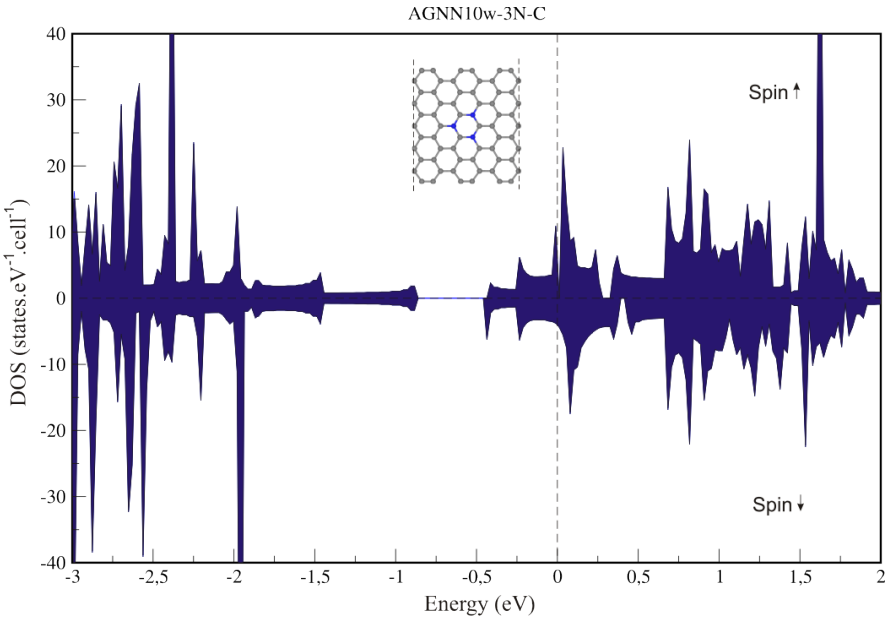

Figure 2.37: Density of states of AGNN10w-3N-C. Inset shows the structure of AGNN10w-3N-C.

moments of *ZGNNs* containing three boron atoms arranged in the same triangular motif. Figure 2.40 shows that spin density of ZGNN8w-3B-C is situated along the edges and also around several carbon atoms surrounding substituted nitrogen atoms.

The formation energy is nearly the same as in the case of N-doped *GNNs* in para position (Table 2.6), and varies only within 2% (*AGNNs*) and 1% (*ZGNNs*) with the ribbons width as it stands in Table 2.10.

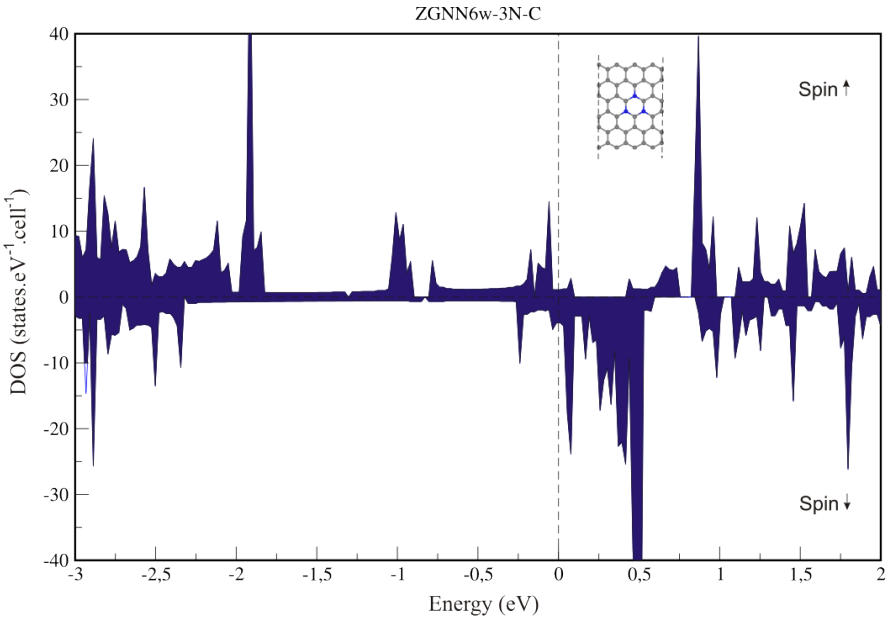

Figure 2.38: Density of states of ZGNN6w-3N-C. Inset shows the structure of ZGNN6w-3N-C.

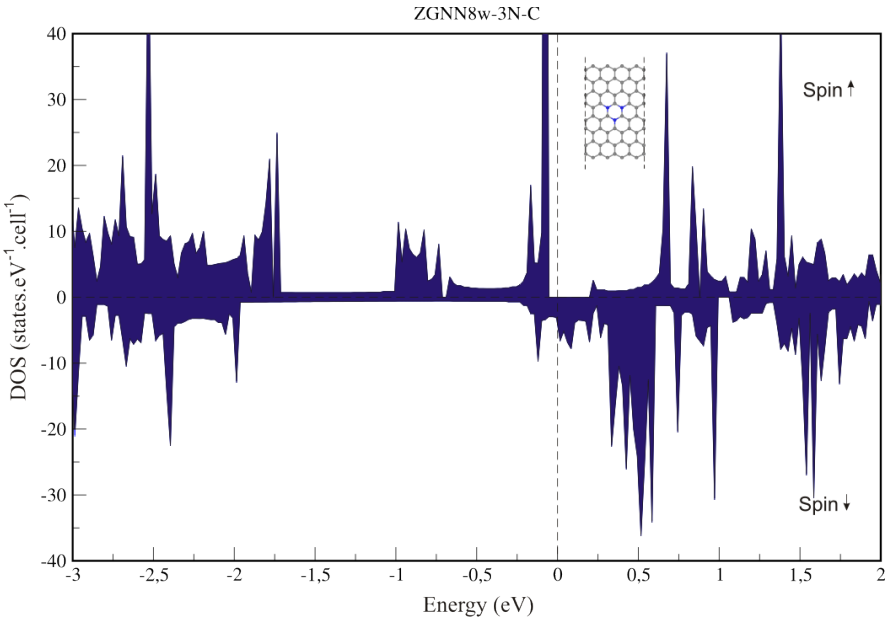

Figure 2.39: Density of states of ZGNN8w-3N-C. Inset shows the structure of ZGNN8w-3N-C.

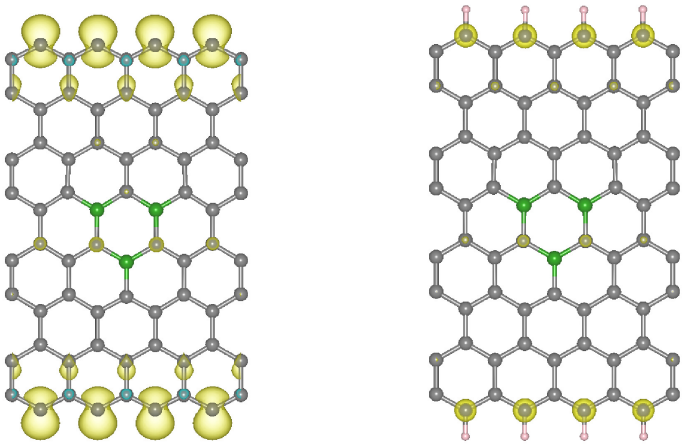

Figure 2.40: Spin density of ZGNN8w-3B-C and ZGNN8w-3B-C-sH in the ground state with isosurfaces level at 8×10^{-3} eÅ^{-3}. The spin density for spin up and spin down is represented by yellow and blue colors, respectively.

Table 2.10: Calculated properties of *GNN-3N-C*, E_f is formation energy, E_{bg} (↑) is band gap energy for spin up and E_{bg} (↓) for spin down.

Name	E_f [eV]	E_{bg} (↑) [eV]	E_{bg} (↓) [eV]	Total mag. mom.	Local mag. mom. [μ_B]
AGNN7w-3N-C	3.86	-	-	1.272	0.689
AGNN8w-3N-C	3.89	-	-	1.839	1.020
AGNN10w-3N-C	3.88	-	-	0.335	0.173
AGNN11w-3N-C	3.88	-	-	1.287	0.722
AGNN12w-3N-C	3.90	-	-	1.028	0.586
AGNN13w-3N-C	3.86	-	-	1.055	0.600
AGNN14w-3N-C	3.84	-	-	0.474	0.269
ZGNN6w-3N-C	3.81	-	-	10.689	6.049
ZGNN8w-3N-C	3.81	-	-	11.000	6.226
ZGNN10w-3N-C	3.80	-	-	11.000	6.230
ZGNN12w-3N-C	3.82	-	-	11.027	6.205

AGNN8w-3N-C-sH and AGNN12w-3N-C-sH with H-passivated edges become half-metals (Figure 2.42). On contrary, AGNN10w-3N-C-sH and AGNN14w-3N-C-sH keep their metallic behavior even after edge passivation (Figure 2.43). Bader charge analysis shows the same charge transfer, which was observed in all *GNNs* doped by nitrogen.

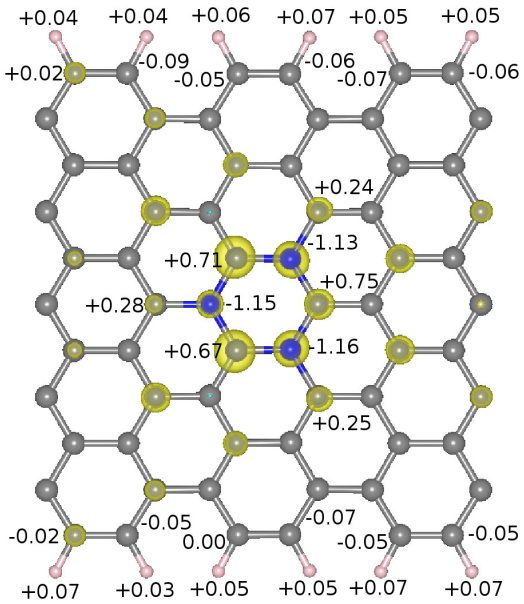

Figure 2.41: Spin density of AGNN10w-3N-C-sH in the ground state with isosurfaces level at 8×10^{-4} eÅ^{-3}. The spin density for spin up is represented by yellow color. Numbers next to atoms represent calculated Bader charges.

Figure 2.41 shows that imbalance in the spin density is located in large area around the nitrogen atoms. DOS plots of all structures, half-metallic and metallic show spin splitting near the Fermi level. Magnetic moments are listed in the Table 2.11 and they change with the width of *AGNNs*. Interestingly enough, they reach nearly the same values for the same width as passivated *AGNNs* containing three boron atoms in the same triangular configuration.

In case of H-passivated *ZGNNs* with three nitrogen atoms in the triangular configuration, the electronic properties are also dependent on the widths. Narrow structures (*i.e.* ZGNN6w-3N-C-sH and ZGNN8w-3N-C-sH) are metallic (Figure 2.44) but wider nanoribbons (*i.e.* ZGNN10w-3N-C-sH and ZGNN12w-3N-C-sH) became half-metals after edge passivation (Figure 2.45).

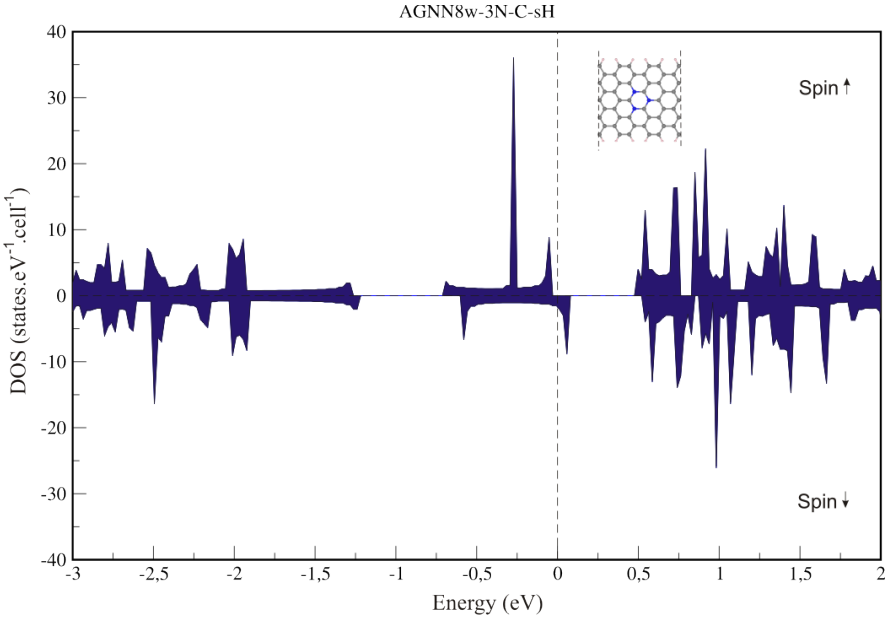

Figure 2.42: Density of states of AGNN8w-3N-C-sH. Inset shows the structure of AGNN8w-3N-C-sH.

As can be seen all DOS plots show spin splitting near the Fermi level. Corresponding magnetic moments are listed in the Table 2.11. In comparison with boron doped *ZGNNs* with edges passivated by hydrogen atoms (Table 2.9), passivated N-doped *ZGNNs* have magnetic moments of higher values.

Figure 2.4.2 shows that imbalance in the spin density of ZGNN8w-3N-C-sH along the edges is inhibit in comparison with ZGNN8w-3N-C with bare

edges. But the spin density in the area around the heteroatoms remains the same. Therefore, it can be said that edge passivation affects only the edge magnetism.

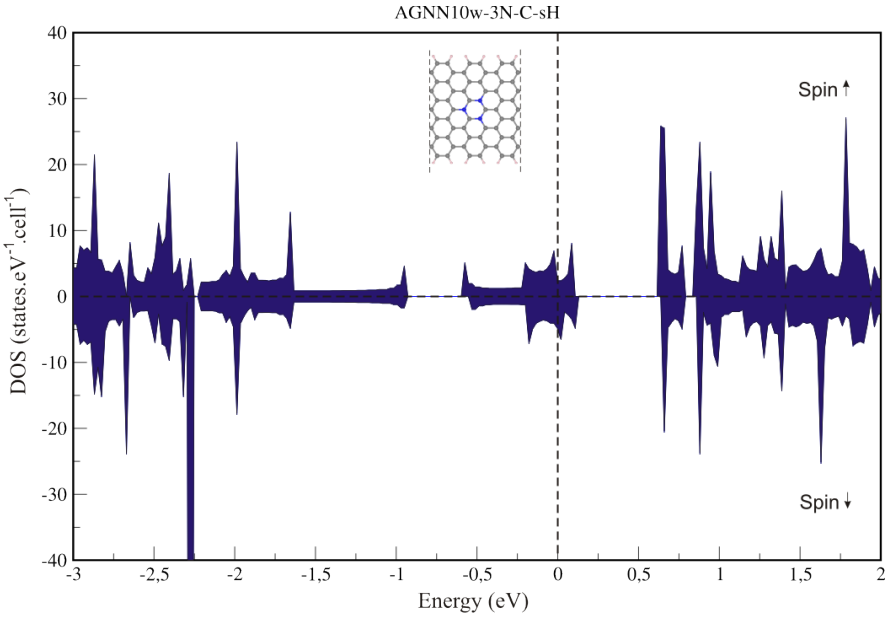

Figure 2.43: Density of states of AGNN10w-3N-C-sH. Inset shows the structure of AGNN10w-3N-C-sH.

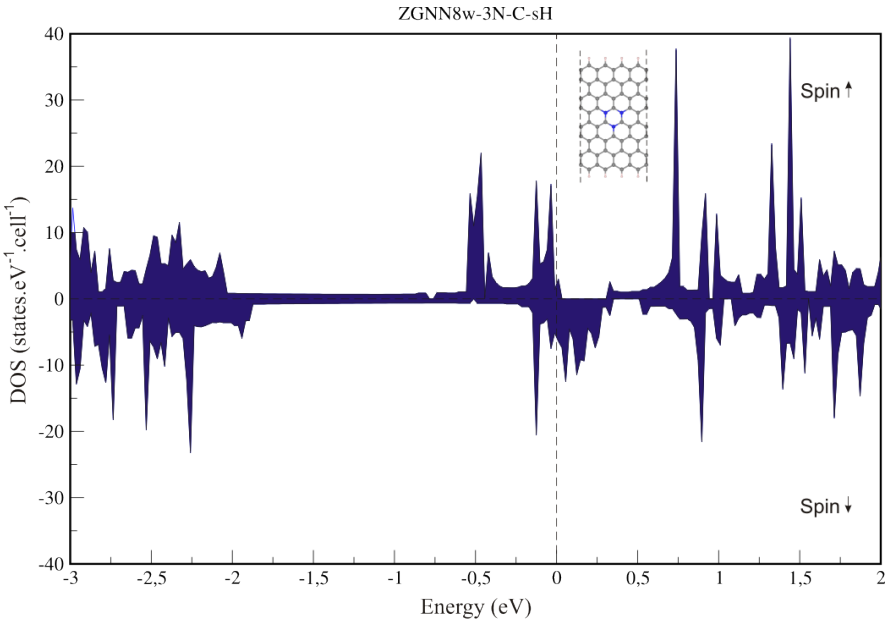

Figure 2.44: Density of states of ZGNN8w-3N-C-sH. Inset shows the structure of ZGNN8w-3N-C-sH.

Table 2.11: Calculated properties of *GNN-3N-C-sH*, E_{bg} (↑) is band gap energy for spin up and E_{bg} (↓) for spin down.

Name	E_{bg} (↑) [eV]	E_{bg} (↓) [eV]	Total mag. mom.	Local mag. mom. [μ_B]
AGNN8w-3N-C-sH	-	-	1.000	0.495
AGNN10w-3N-C-sH	-	-	0.231	0.130
AGNN12w-3N-C-sH	-	-	1.000	0.566
AGNN14w-3N-C-sH	-	-	0.437	0.247
ZGNN6w-3N-C-sH	-	-	1.180	0.647
ZGNN8w-3N-C-sH	-	-	2.841	1.510
ZGNN10w-3N-C-sH	-	-	3.000	1.594
ZGNN12w-3N-C-sH	-	-	3.000	1.590

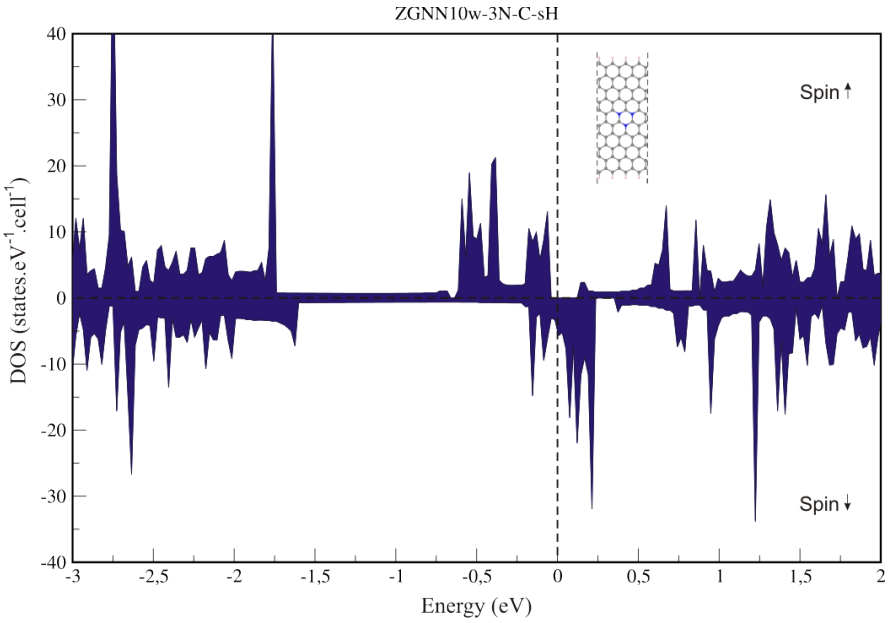

Figure 2.45: Density of states of ZGNN10w-3N-C-sH. Inset shows the structure of ZGNN10w-3N-C-sH.

In summary, this chapter reports our results of *GNNs* with three hetero atoms in the structure in the triangular configuration.

Boron doped *AGNNs* show electronic properties which are dependent on the width of *AGNNs*. The most narrow structure AGNN7w-3B-C is semiconductive and AGNN8w-3B-C is half-metal. All wider B-doped nanoribbons are metals. Magnetic properties are quite complex. All DOS plots show spin splitting near the Fermi level except the AGNN10w-3B-C, which is the only one nonmagnetic. All other tested boron doped *AGNNs* have magnetic moments which change with the width of *AGNNs*. The electronic properties of H-passivated *AGNNs* with three boron atoms in the structure are dependent on the width. Structures AGNN8w-3B-C-sH and AGNN12w-3B-C-sH are half-metals and remaining structures (*i.e.*, AGNN10w-3B-C-sH and

AGNN14w-3B-C-sH) have metallic character. The magnetic moments of H-passivated *AGNNs* change significantly with the widths.

B-doped *ZGNNs* also have electronic properties dependent on the width. The most narrow nanoribbon ZGNN6w-3B-C is a metal, but all wider *ZGNNs* are half metallic. Concerning the magnetic properties, all *ZGNNs* show magnetic moments reaching higher values than in the case of *ZGNNs* containing two boron atoms in para position. Passivated *ZGNNs* are metals and their magnetic moments increase with the widths, except the widest ZGNN12w-3B-C-sH, for which it is slightly decreased.

All nitrogen doped *AGNNs* are metals. The magnetic moments changes significantly with the widths however no clear trend of this change has been found. In case of H-passivated AGNNs containing three nitrogen atoms arranged in triangular configuration electronic properties depend on the widths as in case of B-doped AGNNs with H-passivated edges. AGNN8w-3N-C-sH and AGNN12w-3N-C-sH are half-metallic. On contrary, AGNN10w-3N-C-sH and AGNN12w-3N-C-sH are metals. Magnetic moments reach the higher values for the half-metallic structures that for metals.

The most narrow nanoribbon ZGNN6w-3N-C is metal but all wider *ZGNNs* are half-metals. Also the magnetic moments are nearly the same as in the case of B-doped *ZGNNs*. But they have higher values in comparison with pristine *ZGNNs*. After edge passivation, narrow *ZGNNs* (*i.e.*, ZGNN6w-3N-C-sH and ZGNN8w-3N-C-sH) are metallic but the wider *ZGNNs* (*i.e.*, ZGNN10w-3N-C-sH and ZGNN12w-3N-C-sH) are half-metals. In comparison with boron doped *ZGNNs* with edges passivated by hydrogen atoms, the N-doped *ZGNNs* reach higher values of magnetic moments.

2.4.3 Brief discussion of other tested structures

This section reports results of two more configurations, which were tested to take into account random nature of dopation.

3 hetero atoms in configuration B

Another motif of dopant atoms in *GNNs* which has been tested is three dopant atoms in triangular configuration denoted by "B" and shown in Figure 2.46.

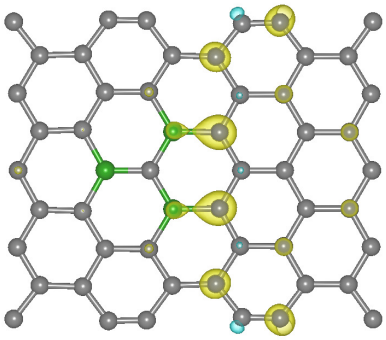

Figure 2.46: Spin density of AGNN8w-3B-B in the ground state with isosurfaces level at 4×10^{-3} eÅ^{-3}. The spin density for spin up and spin down is represented by yellow and blue colors, respectively.

Narrow *AGNNs* (*i.e.*, AGNN7w-3B-B and AGNN8w-3B-B) are half-metals and all wider *AGNNs* have metallic character. Figure 2.47 shows DOS plot of AGNN8w-3B-B with strong spin imbalance at the Fermi level, which is the sign of magnetism. Magnetic moments of all structures are listed in Table 2.12 and depend on the widths. But two structures, AGNN10w-3B-B and AGNN12w-3B-B, show no magnetism.

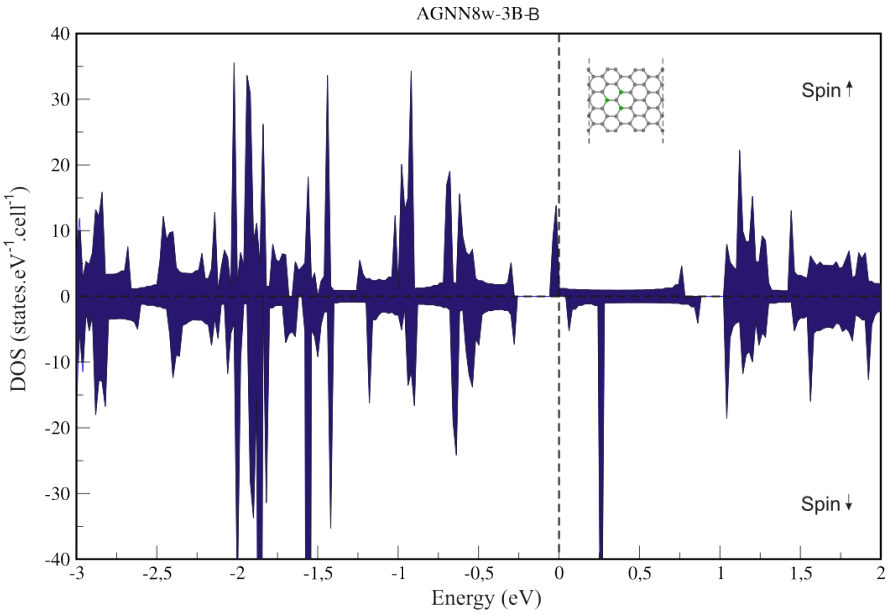

Figure 2.47: Density of states of AGNN8w-3B-B. Inset shows the structure of AGNN8w-3B-B.

H-passivated *AGNNs* with B configuration of boron atoms have the same electronic properties as in the case of B-doped AGNNs with bare edges. Narrow nanoribbon AGNN8w-3B-B-sH is still half-metal and its magnetism persists unchanged. All remaining structures keep their metallic character. Interestingly enough, passivated AGNN10w-3B-B-sH shows weak magnetism, but AGNN12w-3B-B-sH is nonmagnetic.

ZGNNs containing three boron atoms in the B configurations are metallic (Figure 2.48). Magnetic moments are listed in Table 2.12 and they change slightly with the width of *ZGNNs* without clear trend. Figure 2.49 shows that imbalance in the spin density is situated along the both edges. All *ZGNNs* keep their metallic character even after edge passivation. Concerning the magnetic properties, magnetic moments are strongly suppressed after

Table 2.12: Calculated properties of *GNN-3B-B*, E_f is formation energy, E_{bg} (↑) is band gap energy for spin up and E_{bg} (↓) for spin down.

Name	E_f [eV]	E_{bg} (↑) [eV]	E_{bg} (↓) [eV]	Total mag. mom.	Local mag. mom. [μ_B]
AGNN7w-3B-B	2.63	-	-	1.000	0.504
AGNN8w-3B-B	2.79	-	-	1.000	0.513
AGNN10w-3B-B	2.90	-	-	0.000	0.000
AGNN11w-3B-B	2.95	-	-	0.587	0.298
AGNN12w-3B-B	2.98	-	-	0.000	0.000
AGNN13w-3B-B	2.98	-	-	0.802	0.407
AGNN14w-3B-B	2.98	-	-	0.768	0.392
ZGNN6w-3B-B	2.91	-	-	9.793	5.617
ZGNN8w-3B-B	3.04	-	-	10.427	5.906
ZGNN10w-3B-B	3.14	-	-	10.291	5.836
ZGNN12w-3B-B	3.05	-	-	10.519	5.943

H-passivation (Table 2.14) but they are nearly the same as in the case of H-passivated *ZGNNs* containing three boron atoms in triangular configuration C.

The formation energy of B-doped *GNNs* varies within 12% (*AGNNs*) and 8% (*ZGNNs*) with the ribbons width as it stands in Table 2.12.

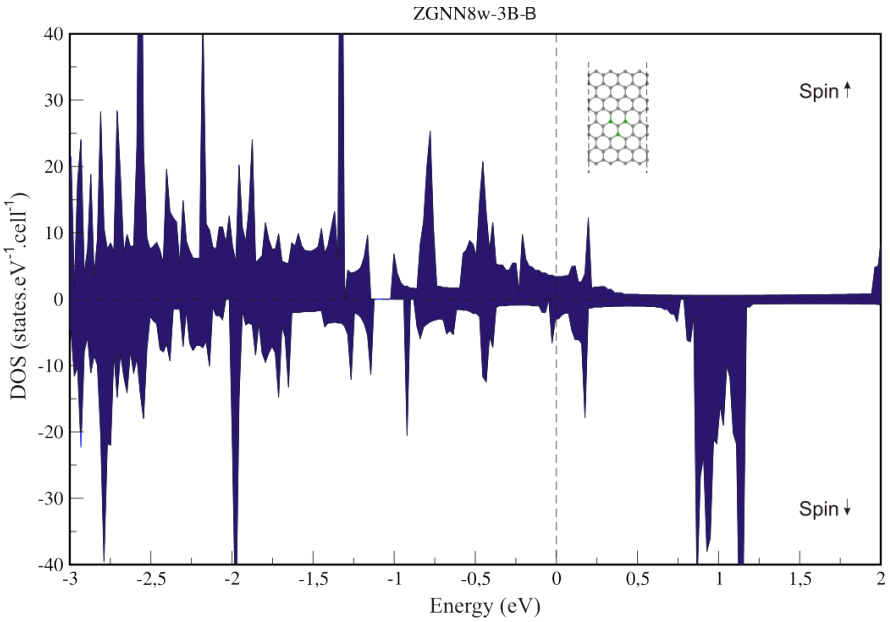

Figure 2.48: Density of states of ZGNN8w-3B-B. Inset shows the structure of ZGNN8w-3B-B.

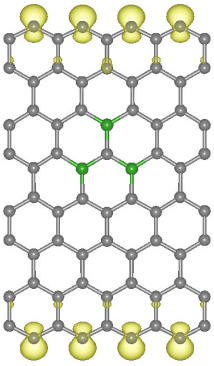

Figure 2.49: Spin density of ZGNN8w-3B-B in the ground state with isosurfaces level at 4×10^{-3} eÅ^{-3}. The spin density for spin up is represented by yellow color.

Next, the same motif has been tested by using nitrogen as a dopant element. All tested *AGNNs* with bare edges containing three nitrogen atoms arranged in B configuration show metallic character. Figure 2.51 displays DOS plot of AGNN8w-3N-B with strong spin splitting near the Fermi level which is inherent to all N-doped *AGNNs*. Magnetic moments are listed in Table 2.13 and they depend on the widths. The structure AGNN10w-3N-B shows weaker magnetism in comparison with remaining N-doped *AGNNs*.

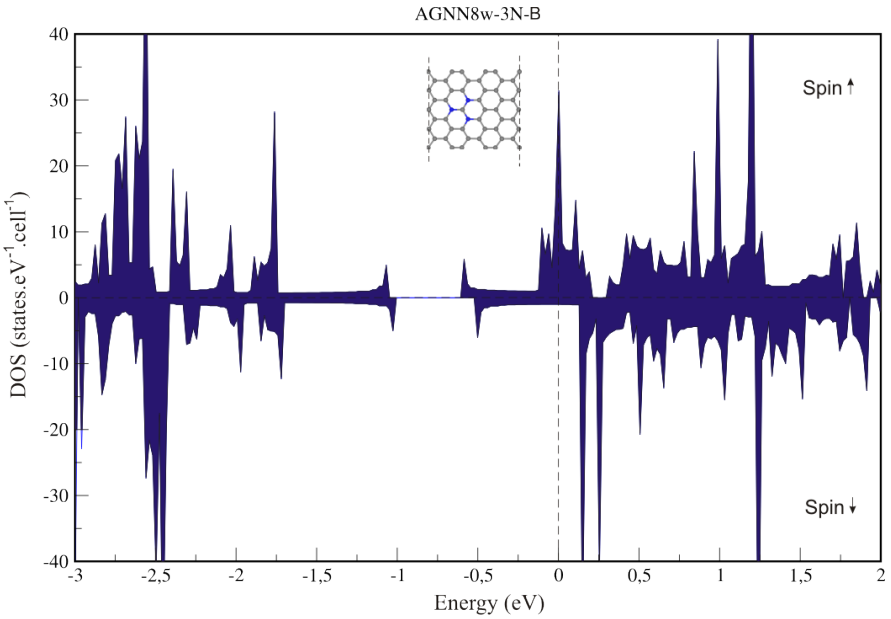

Figure 2.50: Density of states of AGNN8w-3N-B. Inset shows the structure of AGNN8w-3N-B.

Nitrogen doped *AGNNs* with edges passivated by hydrogen atoms became half-metals. Magnetic moments of the corresponding structures are listed in Table 2.15 and they are slightly suppressed in comparison with N-doped *AGNNs* with bare edges.

N-doped *ZGNNs* with edges passivated by hydrogen atoms have electronic

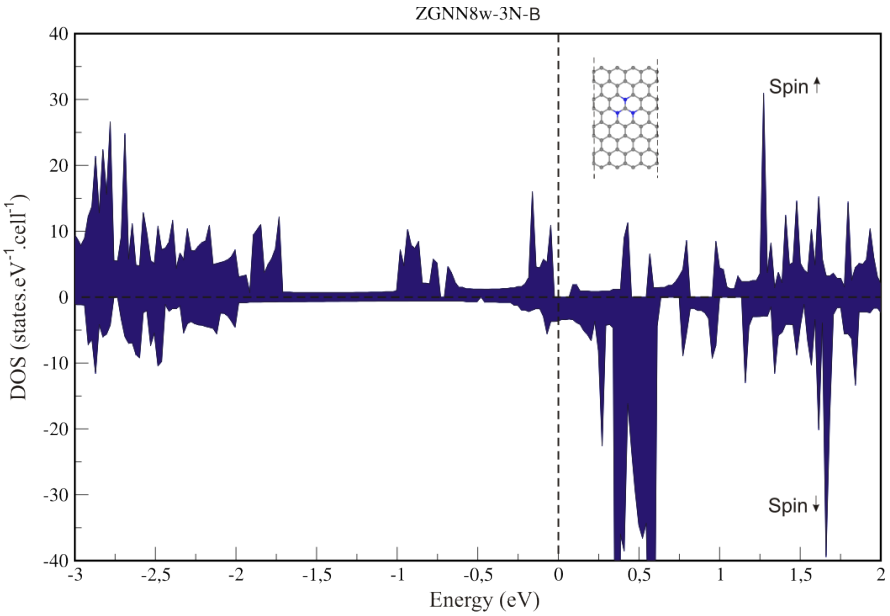

Figure 2.51: Density of states of ZGNN8w-3N-B. Inset shows the structure of ZGNN8w-3N-B.

properties dependent on the width. Narrow nanoribbons, *i.e.* ZGNN6w-3N-B-sH and ZGNN8w-3N-B-sH keep their metallic character, but wider nanoribbons, *i.e.* ZGNN10w-3N-B-sH and ZGNN12w-3N-B-sH are half-metallic. Magnetic moments (Table 2.15) reach higher values in comparison with passivated B-doped *ZGNNs*.

The formation energy of N-doped *GNNs* varies within only 2% in the both types of *GNNs* with the ribbons width as it stands in Table 2.13.

Table 2.13: Calculated properties of *GNN-3N-B*, E_f is formation energy, E_{bg} (↑) is band gap energy for spin up and E_{bg} (↓) for spin down.

Name	E_f [eV]	E_{bg} (↑) [eV]	E_{bg} (↓) [eV]	Total mag. mom.	Local mag. mom. [μ_B]
AGNN7w-3N-B	3.91	-	-	1.313	0.706
AGNN8w-3N-B	3.95	-	-	1.690	0.922
AGNN10w-3N-B	3.96	-	-	0.398	0.209
AGNN11w-3N-B	3.93	-	-	0.966	0.537
AGNN12w-3N-B	3.95	-	-	0.777	0.440
AGNN13w-3N-B	3.91	-	-	0.827	0.466
AGNN14w-3N-B	3.90	-	-	1.430	0.796
ZGNN6w-3N-B	3.89	-	-	9.704	5.502
ZGNN8w-3N-B	3.88	-	-	11.000	6.223
ZGNN10w-3N-B	3.92	-	-	11.000	6.235
ZGNN12w-3N-B	3.88	-	-	10.251	6.366

Table 2.14: Calculated properties of *GNN-3B-B-sH*, E_{bg} (↑) is band gap energy for spin up and E_{bg} (↓) for spin down.

Name	E_{bg} (↑) [eV]	E_{bg} (↓) [eV]	Total mag. mom.	Local mag. mom. [μ_B]
AGNN8w-3B-B-sH	-	-	1.000	0.501
AGNN10w-3B-B-sH	-	-	0.018	0.009
AGNN12w-3B-B-sH	-	-	0.000	0.000
AGNN14w-3B-B-sH	-	-	0.646	0.329
ZGNN6w-3B-B-sH	-	-	1.260	0.647
ZGNN8w-3B-B-sH	-	-	2.277	1.162
ZGNN10w-3B-B-sH	-	-	2.270	1.166
ZGNN12w-3B-B-sH	-	-	2.388	1.228

Table 2.15: Calculated properties of *GNN-3N-B-sH*, E_{bg} (↑) is band gap energy for spin up and E_{bg} (↓) for spin down.

Name	E_{bg} (↑) [eV]	E_{bg} (↓) [eV]	Total mag. mom.	Local mag. mom. [μ_B]
AGNN8w-3N-B-sH	-	-	1.000	0.555
AGNN10w-3N-B-sH	-	-	0.451	0.253
AGNN12w-3N-B-sH	-	-	0.860	0.482
AGNN14w-3N-B-sH	-	-	0.691	0.387
ZGNN6w-3N-B-sH	-	-	0.365	0.175
ZGNN8w-3N-B-sH	-	-	2.660	1.406
ZGNN10w-3N-B-sH	-	-	3.000	1.591
ZGNN12w-3N-B-sH	-	-	3.142	1.666

3 hetero atoms in configuration D

The final tested motif of dopant atoms is denoted by "D" and shown in Figure 2.52. This particular configuration was tested only on *AGNNs*. All *AGNNs* nanoribbons containing three boron atoms in configuration D are metallic. Figure 2.53 shows DOS plot of AGNN10w-3B-D. There is no spin splitting near the Fermi level and only AGNN10w-3B-D and AGNN13w-3B-D exhibit weak magnetism, all remaining B-doped *AGNNs* are non-magnetic (Table 2.16).

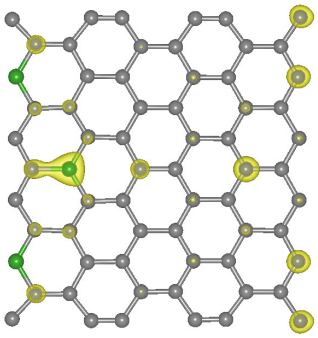

Figure 2.52: Spin density of AGNN10w-3B-D in the ground state with isosurfaces level at 3×10^{-4} eÅ^{-3}. The spin density for spin up is represented by yellow color.

The most narrow AGNN8w-3B-D-sH with edges passivated by hydrogen atoms shows half-metallic character, but all wider H-passivated *AGNNs* are metallic. Interestingly enough, narrow structures AGNN8w-3B-D-sH and AGNN10w-3B-D-sH are magnetic, but in the case of AGNN10w-3B-D-sH the magnetic moments are suppressed (Figure 2.54). All wider H-passivated *AGNNs* are non-magnetic (Table 2.18).

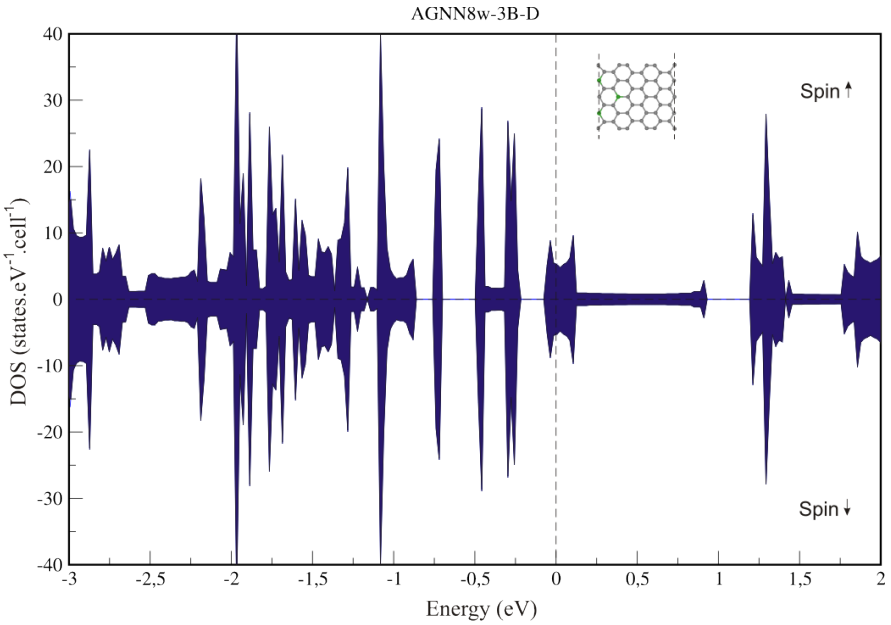

Figure 2.53: Density of states of AGNN8w-3B-D. Inset shows the structure of AGNN8w-3B-D.

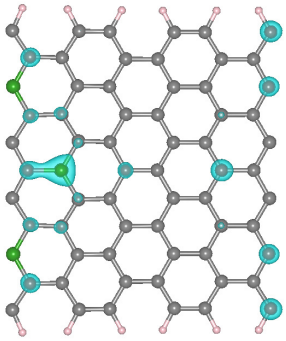

Figure 2.54: Spin density of AGNN10w-3B-D-sH in the ground state with isosurfaces level at 8×10^{-5} eÅ^{-3}. The spin density for spin up is represented by yellow color.

The formation energy of B-doped *AGNNs* varies within 17% with the ribbons width as it stands in Table 2.16. This is the highest value of formation energy of all tested structures.

Table 2.16: Calculated properties of *GNN-3B-D*, E_f is formation energy, E_{bg} (↑) is band gap energy for spin up and E_{bg} (↓) for spin down.

Name	E_f [eV]	E_{bg} (↑) [eV]	E_{bg} (↓) [eV]	Total mag. mom.	Local mag. mom. [μ_B]
AGNN7w-3B-D	2.41	-	-	0.000	0.000
AGNN8w-3B-D	2.70	-	-	0.000	0.000
AGNN10w-3B-D	2.62	-	-	0.024	0.012
AGNN11w-3B-D	2.62	-	-	0.000	0.000
AGNN12w-3B-D	2.64	-	-	0.000	0.000
AGNN13w-3B-D	2.70	-	-	0.012	0.001
AGNN14w-3B-D	2.89	-	-	0.000	0.000

The same motif was also tested with nitrogen as a dopant element. *AGNNs* containing three nitrogen atoms in D configuration are metallic. Figure 2.55 shows DOS plot with strong imbalance near the Fermi level, which is the sign of the magnetism. Magnetic moments are listed in Table 2.17 and for the narrow nanoribbons they are nearly identical. But the magnetic moments of AGNN12w-3N-D and the wider nanoribbons are decreased in comparison with narrow structures (*i.e.*, AGNN7w-3N-D - AGNN11w-3N-D).

H-passivated AGNNs containing three nitrogen atoms in D configuration are metallic. But only two narrow nanoribbons (*i.e.* AGNN8w-3N-D-sH and AGNN10w-3N-D-sH) are magnetic, which is the same as in the case of *AGNNs* with three boron atoms arranged in the same motif. Wider

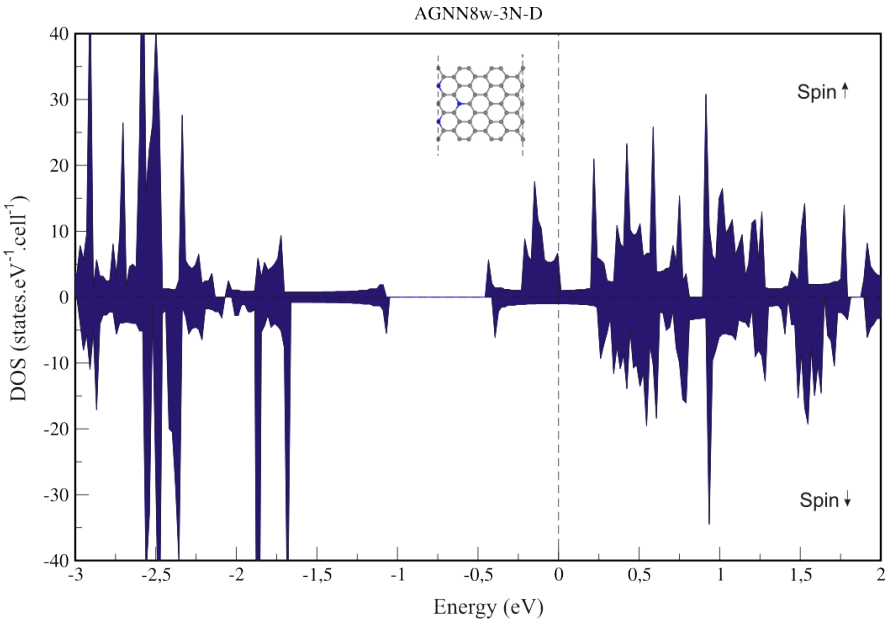

Figure 2.55: Density of states of AGNN8w-3N-D. Inset shows the structure of AGNN8w-3N-D.

Table 2.17: Calculated properties of *GNN-3N-D*, E_f is formation energy, E_{bg} (↑) is band gap energy for spin up and E_{bg} (↓) for spin down.

Name	E_f [eV]	E_{bg} (↑) [eV]	E_{bg} (↓) [eV]	Total mag. mom.	Local mag. mom. [μ_B]
AGNN7w-3N-D	3.54	-	-	1.840	1.006
AGNN8w-3N-D	3.66	-	-	1.922	1.045
AGNN10w-3N-D	3.69	-	-	1.939	1.052
AGNN11w-3N-D	3.68	-	-	1.875	1.019
AGNN12w-3N-D	3.69	-	-	0.742	0.390
AGNN13w-3N-D	3.66	-	-	0.679	0.357
AGNN14w-3N-D	3.78	-	-	0.457	0.239

nanoribbons, *i.e.* AGNN12w-3B-D-sH and AGNN14w-3B-D-sH became non-magnetic after edge passivation by hydrogen atoms (Table 2.19).

The formation energy of N-doped *AGNNs* varies within 4% with the ribbons width as it stands in Table 2.17.

Table 2.18: Calculated properties of *GNN-3B-D-sH*, E_{bg} (↑) is band gap energy for spin up and E_{bg} (↓) for spin down.

Name	E_{bg} (↑) [eV]	E_{bg} (↓) [eV]	Total mag. mom.	Local mag. mom. [μ_B]
AGNN8w-3B-D-sH	-	-	1.000	0.505
AGNN10w-3B-D-sH	-	-	-0.093	-0.046
AGNN12w-3B-D-sH	-	-	0.000	0.000
AGNN14w-3B-D-sH	-	-	0.000	0.000

Table 2.19: Calculated properties of *GNN-3N-D-sH*, E_{bg} (↑) is band gap energy for spin up and E_{bg} (↓) for spin down.

Name	E_{bg} (↑) [eV]	E_{bg} (↓) [eV]	Total mag. mom.	Local mag. mom. [μ_B]
AGNN8w-3N-D-sH	-	-	0.030	0.017
AGNN10w-3N-D-sH	-	-	0.074	0.041
AGNN12w-3N-D-sH	-	-	0.000	0.000
AGNN14w-3N-D-sH	-	-	0.000	0.000

Conclusion

In this thesis we studied electronic and magnetic properties of graphene nanoribbons with armchair and zigzag edges. Pristine armchair graphene nanoribbons are nonmagnetic semiconductors. The band gaps are dependent on the widths of nanoribbons and show cusps. Similarly, zigzag graphene nanoribbons are semiconductive and the size of the band gap is changing with the width of nanoribbons without clear trend. Nanoribbons with zigzag edges are magnetic with antiferromagnetic interaction between the edges. But the energy difference between ferromagnetic and antiferromagnetic ordering is low and it decreases with increasing width od zigzag graphene nanoribbons.

Next, the influence of edge passivation by hydrogen atoms on the electronic and magnetic properties of graphene nanoribbons was studied. Passivated graphene nanoribbons are still semiconductive, but the size of the band gaps is decreased in all studied nanoribbons of both types. In case of armchair nanoribbons, the dependence of band gap on the width still show cusps. Compared to that, the dependence of band gap energy of H-passivated zigzag nanoribbons is increasing with the widths. Magnetic moments along the edges are reduced after edge passivation. Howerver the antiferromagnetic ordering remains unchanged after edge passivation, the energy difference between the ferromagnetic and antiferromagnetic ordering is even decreased in

comparison with nanoribbons with bare edges.

Further, we studied in details the properties of nanoribbons with bare edges and also with passivated edges doped by boron and nitrogen. Boron atom, which has one electron less than carbon, should induce p-type behavior in graphene lattice. In case of nitrogen one electron remains unpaired, thus n-type behavior is expected.

Boron and nitrogen doped graphene nanoribbons have electronic properties dependent on the motif of hetero atoms substituted in the structure of nanoribbons and also the width of nanoribbons plays the key role. Therefore, the electronic properties are in many cases different from behavior of doped infinite graphene sheet. It should be pointed out that edge passivation by hydrogen atoms also changes electronic state in many cases in comparison with nanoribbons containing the same motif of dopant atoms with bare edges.

Magnetic properties of doped graphene nanoribbons are also quite complex. Generally, dopation of armchair graphene nanoribbons by boron atoms induces weaker magnetism in comparison with nitrogen doped nanoribbons. The magnetic moments of doped armchair nanoribbons change with the widths. Nevertheless no clear trend of this behavior was found. The dependence of magnetic state on the symmetry of doped armchair graphene nanoribbons has been found only in the nanoribbons containing two nitrogen atoms in para possition. Doped zigzag nanoribbons show significantly stronger magnetism than doped nanoribbons with armchair edges. Boron doped zigzag nanoribbons have nearly the same magnetic moments as nitrogen doped nanoribbons. Doped zigzag nanoribbons with edges passivated by hydrogen atoms have magnetic moments suppressed in comparison with

doped zigzag nanoribbons with bare edges.

Nevertheless, further study is still needed and for further research we can suggest the calculation of the J-parameter to get information about the Curie temperature. Also the study of co-dopation by boron and nitrogen atoms might be interesting.

Bibliography

[1] Kroto, H. W.; Heath, J. R.; O'Brien, S. C.; Curl R. F.; Smalley, R. E. *C-60 - Buckinsterfullerene.* NATURE, 1985, vol. 318, issue 6042, 162-163, DOI: 10.1038/318162a0.

[2] Kratschmer, W.; Lamb, L. D.; Fostiropoulos, K.; Huffman, D. R. *Solid C-60 - a new form of carbon.* NATURE, 1990, vol. 347, issue 6291, 354-358, DOI: 10.1038/347354a0.

[3] Novoselov, K.S.; Geim, A.K.; Morozov, S.V.; Jiang, D.; Zhang, Y.; Dubonos, S.V.; Grigorieva, I.V.; Firsov, A.A. *Electric field effect in atomically thin carbon films.* SCIENCE, 2004, vol. 306, issue 5696, 666-669, DOI: 10.1126/science.1102896.

[4] Yazyev, O.V.; Helm, L. *Defect-induced magnetism in graphene.* PHYSICAL REVIEW B, 2007, vol. 75, issue 12, DOI: 10.1103/PhysRevB.75.125408.

[5] Tucek, J.; Blonski, P.; Sofer, Z.; Simek, P.; Petr, M. Pumera, M.; Otyepka, M.; Zboril, R. *Sulfur doping induces strong ferromagnetic ordering in graphene: Effect of concentration and substitution mech-*

anism. ADVANCED MATERIALS, 2016, vol. 28, issue 25, 5045-5053, DOI: 10.1002/adma.201600939.

[6] Rani, P.; Jindal, V.K. *Designing band gap of graphene by B and N dopant atoms.* RSC ADVANCES, 2013, vol. 3, issue 3, 802-812, DOI: 10.1039/c2ra22664b.

[7] Enoki, T.; Takai, K.; Kiguchi, M. *Magnetic edge state of nanographene and unconventional nanographene-based host-guest systems.* BULLETIN OF THE CHEMICAL SOCIETY OF JAPAN, 2012, vol. 85, issue 3, 249-264, DOI: 10.1246/bcsj.20110236.

[8] Terrones, M.; Botello-Mendez, A.R.; Campos-Delgado, J.; Lopez-Urias, F.; Vega-Cantu, Y.I.; Rodriguez-Macias, F.J.; Elias, A.L.; *Graphene and graphite nanoribbons: Morphology, properties, synthesis, defects and applications.* NANO TODAY, 2010, vol. 5, issue 4, 351-372, DOI: 10.1016/j.nantod.2010.06.010.

[9] Yazyev, O.V. *Emergence of magnetism in graphene materials and nanostructures.* REPORTS ON PROGRESS IN PHYSICS, 2010, vol. 73, issue 5, DOI: 10.1088/0034-4885/73/5/056501.

[10] Kresse, G.; Furthmuller, J. *Efficient iterative schemes for ab initio total-energy calculations using a plane-wave basis set.* PHYSICAL REVIEW B, 1996, vol. 54, issue 16, 11169-11186, DOI: 10.1103/PhysRevB.54.11169.

[11] Kresse, G.; Joubert, D. *From ultrasoft pseudopotentials to the projector augmented-wave method.* PHYSICAL REVIEW B, 1999, vol. 59, issue 3, 1758-1775, DOI: 10.1103/PhysRevB.59.1758.

[12] Kunstmann, J.; Ozdogan, C.; Quandt, A.; Fehske, H. *Stability of edge states and edge magnetism in graphene nanoribbons.* PHYSICAL REVIEW B, 2011, vol. 83, issue 4, DOI: 10.1103/PhysRevB.83.045414.

[13] Georgakilas, V.; Perman, J.A.; Tucek, J.; Zboril, R. *Broad family of carbon nanoallotropes: classification, chemistry, and applications of fullerenes, carbon dots, nanotubes, graphene, nanodiamonds, and combined superstructures.* CHEMICAL REVIEWS, 2015, vol. 115, issue 11, 4744-4822, DOI: 10.1021/cr500304f.

[14] Zeynalov, E.B.; Allen, N.S.; Salmanova, N.I. *Radical scavenging efficiency of different fullerenes C-60-C-70 and fullerene soot.* POLYMER DEGRADATION AND STABILITY, 2009, vol. 94, issue 8, DOI: 10.1016/j.polymdegradstab.2009.04.027.

[15] Zeynalov, E.B.; Kossmehl, G. *Fullerene C-60 as an antioxidant for polymers.* POLYMER DEGRADATION AND STABILITY, 2001, vol. 71, issue 2, DOI: 10.1016/S0141-3910(00)00109-9.

[16] Kroto, H. W.; *The stability of the fullerenes C-24, C-28, C-32, C-36, C-50, C-60 AND C-70.* NATURE, 1987, vol. 329, issue 6139, 529-531, DOI: 10.1038/329529a0.

[17] Hebard, A.F.; Rosseinsky, M.J.; Haddon, R.C.; Murphy, D.W.; Glarum, S.H.; Palstra, T.T.M.; Ramirez, A.P.; Kortan, A.R. *Superconductivity*

at 18-K in potassium-doped C-60. NATURE, 1991, vol. 350, issue 6319, 600-601, DOI: 10.1038/350600a0.

[18] Tanigaki, K.; Ebbesen, T.W.; Saito, S.; Mizuki, J.; Tsai, J.S.; Kubo, Y.; Kuroshima, S. *Superconductivity at 33-K IN CSXRBYC60.* NATURE, 1991, vol. 352, issue 6332, 222-223, DOI: 10.1038/352222a0.

[19] Sano, N.; Wang, H.; Chhowalla, M.; Alexandrou, I.; Amaratunga, G.A.J. *Nanotechnology - Synthesis of carbon 'onions' in water.* NATURE, 2001, vol. 414, issue 6863, 506-507, DOI: 10.1038/35107141.

[20] Pech, D.; Brunet, M.; Durou, H.; Huang, P.H.; Mochalin, V.; Gogotsi, Y.; Taberna, P.L.; Simon, P. *Ultrahigh-power micrometre-sized supercapacitors based on onion-like carbon.* NATURE NANOTECHNOLOGY, 2010, vol. 5, issue 9, 651-654, DOI: 10.1038/nnano.2010.162.

[21] Sun, Y.P.; Zhou, B.; Lin, Y.; Wang, W.; Fernando, K.A.S.; Pathak, P.; Meziani, M.J.; Harruff, B.A.; Wang, X. Wang, H.F. *Quantum-sized carbon dots for bright and colorful photoluminescence.* JOURNAL OF THE AMERICAN CHEMICAL SOCIETY, 2006, vol. 128, issue 24, 7756-7757, DOI: 10.1021/ja062677d.

[22] Cao, L.; Wang, X.; Meziani, M.J.; Lu, F.S.; Wang, H.F.; Luo, P.J.G.; Lin, Y.; Harruff, B.A.; Veca, L.M.; Murray, D. *Carbon dots for multiphoton bioimaging.* JOURNAL OF THE AMERICAN CHEMICAL SOCIETY, 2007, vol. 129, issue 37, DOI: 10.1021/ja073527l.

[23] Ritter, K.A.; Lyding, J.W. *The influence of edge structure on the electronic properties of graphene quantum dots and nanoribbons.* NATURE MATERIALS, 2009, vol. 8, issue 3, 235-242, DOI: 10.1038/NMAT2378.

[24] Kim, S.; Hwang, S.W.; Kim, M.K.; Shin, D.Y.; Shin, D.H.; Kim, C.O.; Yang, S.B.; Park, J.H.; Hwang, E.; Choi, S.H. *Anomalous behaviors of visible luminescence from graphene quantum dots: Interplay between size and shape.* ACS NANO, 2012, vol. 6, issue 9, 8203-8208, DOI: 10.1021/nn302878r.

[25] Li, Y.; Hu, Y.; Zhao, Y.; Shi, G.; Deng, L.; Hou, Y.; Qu, L. *An electrochemical avenue to green-luminescent graphene quantum dots as potential electron-acceptors for photovoltaics.* ADVANCED MATERIALS, 2011, vol. 23, 776–780, DOI: 10.1002/adma.201003819.

[26] Zhuo, S.J.; Shao, M.W.; Lee, S.T. *Upconversion and downconversion fluorescent graphene quantum dots: Ultrasonic preparation and photocatalysis.* ACS NANO, 2012, vol. 6, issue 2, 1059-1064, DOI: 10.1021/nn2040395.

[27] Mochalin, V.N.; Shenderova, O.; Ho, D.; Gogotsi, Y. *The properties and applications of nanodiamonds.* NATURE NANOTECHNOLOGY, 2012, vol. 7, issue 1, 11-23, DOI: 10.1038/NNANO.2011.209.

[28] Williams, O. A. *Nanocrystalline diamond.* DIAMOND AND RELATED MATERIALS, 2011, vol. 20, issue 5-6, 621-640, DOI: 10.1016/j.diamond.2011.02.015.

[29] Jelezko, F.; Wrachtrup, J. *Single defect centres in diamond: A review.* PHYSICA STATUS SOLIDI A-APPLICATIONS AND MATERIALS SCIENCE, 2006, vol. 203, issue 13, 3207-3225, DOI: 10.1002/pssa.200671403.

[30] Muller, T.; Aharonovich, I.; Lombez, L.; Alaverdyan, Y.; Vamivakas, A.N.; Castelletto, S.; Jelezko, F.; Wrachtrup, J. *Wide-range electrical tunability of single-photon emission from chromium-based colour centres in diamond.* NEW JOURNAL OF PHYSICS, 2011, vol. 13, DOI: 10.1088/1367-2630/13/7/075001.

[31] Iijima, S. *Helical microtubules of graphitic carbon.* NATURE, 1991, vol. 354, issue 6348, 56-58, DOI: 10.1038/354056a0.

[32] Iijima, S.; Ichihashi, T. *Single-shell carbon nanotubes of 1 nm diameter.* NATURE, 1993, vol. 363, issue 6430, 603-605, DOI: 10.1038/363603a0.

[33] Belin, T.; Epron, F. *Characterization methods of carbon nanotubes: a review.* MATERIALS SCIENCE AND ENGINEERING B-SOLID STATE MATERIALS FOR ADVANCED TECHNOLOGY, 2005, vol. 119, issue 2, 105-118, DOI: 10.1016/j.mseb.2005.02.046.

[34] Takesue, I.; Haruyama, J.; Kobayashi, N.; Chiashi, S.; Maruyama, S.; Sugai, T.; Shinohara, H. *Superconductivity in entirely end-bonded multiwalled carbon nanotubes.* PHYSICAL REVIEW LETTERS, 2006, vol. 96, issue 5, DOI: 10.1103/PhysRevLett.96.057001.

[35] Melechko, A.V.; Merkulov, V.I.; McKnight, T.E.; Guillorn, M.A.; Klein, K.L.; Lowndes, D.H.; Simpson, M.L. *Vertically aligned carbon*

nanofibers and related structures: Controlled synthesis and directed assembly. JOURNAL OF APPLIED PHYSICS, 2005, vol. 97, issue 4, DOI: 10.1063/1.1857591.

[36] Ramos, A.; Camean, I.; Garcia, A.B. *Graphitization thermal treatment of carbon nanofibers.* CARBON, 2013, vol. 59, 2-32, DOI: 10.1016/j.carbon.2013.03.031.

[37] Serp, P.; Corrias, M.; Kalck, P. *Carbon nanotubes and nanofibers in catalysis.* APPLIED CATALYSIS A-GENERAL, 2003, vol. 253, issue 2, 337-358, DOI: 10.1016/S0926-860X(03)00549-0.

[38] Wang, B.; Qiu, J.H.; Feng, H.X.; Sakai, E.; Komiyama, T. *Nitrogen doped carbon nanowires prepared from polypyrrole nanowires for potential application in supercapacitors.* JOURNAL OF ELECTROANALYTICAL CHEMISTRY, 2016, vol. 775, 219-227, DOI: 10.1016/j.jelechem.2016.06.006.

[39] Cao, Y.L.; Xiao, L.F.; Sushko, M.L.; Wang, W.; Schwenzer, B.; Xiao, J.; Nie, Z.M.; Saraf, L.V. *Sodium ion insertion in hollow carbon nanowires for battery applications.* NANO LETTERS, 2012, vol. 12, issue 7, 3783-3787, DOI: 10.1021/nl3016957.

[40] Nakada, K.; Fujita, M.; Dresselhaus, G.; Dresselhaus, M.S. *Edge state in graphene ribbons: Nanometer size effect and edge shape dependence.* PHYSICAL REVIEW B, 1996, vol. 54, issue 24, 17954-17961, DOI: 10.1103/PhysRevB.54.17954.

[41] Iijima, S.; Yudasaka, M.; Yamada, R.; Bandow, S.; Suenaga, K.; Kokai, F.; Takahashi, K. *Nano-aggregates of single-walled graphitic carbon nano-horns.* CHEMICAL PHYSICS LETTERS, 1999, vol. 309, issue 3-4, 165-170, DOI: 10.1016/S0009-2614(99)00642-9.

[42] Kolesnikov, D.V.; Osipov, V.A. *Electronic structure of carbon nanohorns near the Fermi level.* JETP LETTERS, 2004, vol. 79, issue 11, 532-536, DOI: 10.1134/1.1787100.

[43] Novoselov, K.S.; Jiang, Z.; Zhang, Y.; Morozov, S.V.; Stormer, H.L.; Zeitler, U.; Maan, J.C.; Boebinger, G.S.; Kim, P.; Geim, A.K. *Room-temperature quantum hall effect in graphene.* SCIENCE, 2007, vol. 315, issue 5817, 1379, DOI: 10.1126/science.1137201.

[44] Berger, C.; Song, Z.M.; Wu, X.S.; Brown, N.; Naud, C.; Mayou, D.; Li, T.B.; Hass, J.; Marchenkov, A.N. *Electronic confinement and coherence in patterned epitaxial graphene.* SCIENCE, 2006, vol. 312, issue 5777, 1191-1196, DOI: 10.1126/science.1156965.

[45] Novoselov, K.S.; Geim, A.K.; Morozov, S.V; Jiang, D.; Katsnelson, M.I.; Grigorieva, I.V.; Dubonos, S.V.; Firsov, A.A. *Two-dimensional gas of massless Dirac fermions in graphene.* NATURE, 2005, vol. 438, issue 7065, 197-200, DOI: 10.1038/nature04233.

[46] Zhu, Y.W.; Murali, S.; Cai, W.W.; Li, X.S.; Suk, J.W.; Potts, J.R.; Ruoff, R.S. *Graphene and graphene oxide: Synthesis, properties, and applications.* ADVANCED MATERIALS, 2010, vol. 22, issue 35, 3906-3924, DOI: 110.1002/adma.201001068.

[47] Balandin, A.A.; Ghosh, S.; Bao, W.Z.; Calizo, I.; Teweldebrhan, D.; Miao, F.; Lau, C.N. *Superior thermal conductivity of single-layer graphene.* NANO LETTERS, 2008, vol. 8, issue 3, 902-907, DOI: 0.1021/nl0731872.

[48] Nair, R.R.; Blake, P.; Grigorenko, A.N.; Novoselov, K.S.; Booth, T.J.; Stauber, T.; Peres, N.M.R.; Geim, A.K. *Fine structure constant defines visual transparency of graphene.* SCIENCE, 2008, vol. 320, issue 5881, 1308-1308, DOI: 10.1126/science.1125925.

[49] Schedin, F.; Geim, A.K.; Morozov, S.V.; Hill, E.W.; Blake, P.; Katsnelson, M.I.; Novoselov, K.S. *Detection of individual gas molecules adsorbed on graphene.* NATURE MATERIALS, 2007, vol. 6, issue 9, 652-655, DOI: 10.1038/nmat1967.

[50] Geim, A.K.; Novoselov, K.S. *The rise of graphene.* NATURE MATERIALS, 2007, vol. 6, issue 3, 183-191, DOI: 10.1038/nmat1849.

[51] Terrones, M.; Botello-Mendez, A.R.; Campos-Delgado, J.; Lopez-Urias, F.; Vega-Cantu, Y.I.; Rodriguez-Macias, F.J.; Elias, A.L.; Munoz-Sandoval, E.; Cano-Marquez, A.G *Graphene and graphite nanoribbons: Morphology, properties, synthesis, defects and applications.* NANO TODAY, 2010, vol. 5, issue 4, 351-372, DOI: 10.1016/j.nantod.2010.06.010.

[52] Haddon, R.C.; Pasquarello, A. *Magnetic properties of carbon structures.* PHYSICAL REVIEW B, 1994, vol. 50, issue 22, 16459-16463, DOI: 10.1103/PhysRevB.50.16459.

[53] Makarova T.L. *Magnetic properties of carbon structures.* SEMICONDUCTORS, 2004, vol. 38, issue 6, 615-638, DOI: 10.1134/1.1766362.

[54] Allemand, P.M.; Khemani, K.C.; Koch, A.; Wudl, F.; Holczer, K.; Donovan, S.; Gruner G.; Thompson, J.D. *Organic molecular soft ferromagnetism in a fullerene-C60.* SCIENCE, 1991, vol. 253, issue 5017, 301-303, DOI: 10.1126/science.253.5017.301.

[55] Makarova, T.L.; Sundqvist, B.; Hohne, R.; Esquinazi, P.; Kopelevich, Y.; Scharff, P.; Davydov, V.A.; Kashevarova, L.S. *Magnetic carbon.* NATURE, 2001, vol. 413, issue 6857, 716-718, DOI: 10.1038/35099527.

[56] Wood, R.A.; Lewis, M.H.; Lees, M.R.; Bennington, S.M.; Cain, M.G.; Kitamura, N. *Ferromagnetic fullerene.* JOURNAL OF PHYSICS-CONDENSED MATTER, 2002, vol. 14, issue 22, 385-391, DOI: 10.1088/0953-8984/14/22/101.

[57] Makarova, T.L.; Zagaynova, V.S.; Spitsina, N.G. *Fullerene-induced magnetization training effect in single molecular magnet.* PHYSICA STATUS SOLIDI B-BASIC SOLID STATE PHYSICS, 2010, vol. 247, issue 11-12, 3018-3021, DOI: 10.1002/pssb.201000115.

[58] Ajiki, H.; Ando, T. *Magnetic properties of carbon nanotubes.* JOURNAL OF THE PHYSICAL SOCIETY OF JAPAN, 1993, vol. 62, issue 7, 2470-2480, DOI: 10.1143/JPSJ.62.2470.

[59] Ma, Y.C.; Lehtinen, P.O.; Foster, A.S.; Nieminen, R.M. *Magnetic properties of vacancies in graphene and single-walled carbon nanotubes.*

NEW JOURNAL OF PHYSICS, 2004, vol. 6, DOI: 10.1088/1367-2630/6/1/068.

[60] Wu, R.Q.; Liu, L.; Peng, G.W.; Feng, Y.P. *Magnetism in BN nanotubes induced by carbon doping.* APPLIED PHYSICS LETTERS, 2005, vol. 86, issue 12, DOI: 10.1063/1.1890477.

[61] Tucek, J.; Kemp, K.C.; Kim, K.S.; Zboril, R. *Iron-oxide-supported nanocarbon in lithium-ion batteries, medical, catalytic, and environmental applications.* ACS NANO, 2014, vol. 8, issue 8, 7571-7612, DOI: 10.1021/nn501836x.

[62] Sitharaman, B.; Kissell, K.R.; Hartman, K.B.; Tran, L.A.; Baikalov, A.; Rusakova, I.; Sun, Y.; Khant, H.A. *Superparamagnetic gadonanotubes are high-performance MRI contrast agents.* CHEMICAL COMMUNICATIONS, 2005, issue 31, 3915-3917, DOI: 10.1039/b504435a.

[63] Korneva, G.; Ye, H.H.; Gogotsi, Y.; Halverson, D; Friedman, G.; Bradley, J.C.; Kornev, K.G. *Carbon nanotubes loaded with magnetic particles.* NANO LETTERS, 2005, volume 5, issue 5, 879-884, DOI: 10.1021/nl0502928.

[64] Yazyev O.V. *Emergence of magnetism in graphene materials and nanostructures.* REPORTS ON PROGRESS IN PHYSICS, 2010, volume 73, issue 5, DOI: 10.1088/0034-4885/73/5/056501.

[65] Banhart, F.; Kotakoski, J.; Krasheninnikov, A.V. *Structural defects in graphene.* ACS NANO, 2011, volume 5, issue 1, 26-41, DOI: 10.1021/nn102598m.

[66] Pereira, V.M.; Guinea, F.; dos Santos, J.M.; Peres, N.M.; Castro Neto, A.H. *Disorder induced localized states in graphene.* PHYSICAL REVIEW LETTERS, 2006, volume 96, issue 3, DOI: 10.1103/PhysRevLett.96.036801.

[67] Krasheninnikov, A.V.; Lehtinen, P.O.; Foster, A.S.; Nieminen, R.M. *Bending the rules: Contrasting vacancy energetics and migration in graphite and carbon nanotubes.* CHEMICAL PHYSICS LETTERS, 2006, volume 418, issue 1-3, 132-136, DOI: 10.1016/j.cplett.2005.10.106.

[68] Dai, X.Q.; Zhao, J.H.; Xie, M.H.; Tang, Y.N.; Li, Y.H.; Zhao, B. *First-principle study of magnetism induced by vacancies in graphene.* EUROPEAN PHYSICAL JOURNAL B, 2011, volume 80, issue 3, 343-349, DOI: 10.1140/epjb/e2011-10955-x.

[69] Nair, R.R.; Sepioni, M.; Tsai, I.L.; Lehtinen, O.; Keinonen, J.; Krasheninnikov, A.V.; Thomson, T.; Geim, A.K. *Spin-half paramagnetism in graphene induced by point defects.* NATURE PHYSICS, 2012, volume 8, issue 3, 199-202, DOI: 10.1038/NPHYS2183.

[70] Ugeda, M. M.; Brihuega, I.; Guinea, F.; Gomez-Rodriguez, J.M. *Missing atom as a source of carbon magnetism.* PHYSICAL REVIEW LETTERS, 2006, volume 104, issue 9, DOI: 10.1103/PhysRevLett.104.096804.

[71] Lieb, E.H. *Two theorems on the Hubbard model.* PHYSICAL REVIEW LETTERS, 1989, volume 62, issue 10, DOI: 10.1103/PhysRevLett.62.1201.

[72] Vozmediano, M.A.H.; Lopez-Sancho, M.P.; Stauber, T.; Guinea, F. *Local defects and ferromagnetism in graphene layers.* PHYSICAL REVIEW B, 2005, volume 72, issue 15, DOI: 10.1103/PhysRevB.72.155121.

[73] Palacios, J.J.; Fernandez-Rossier, J.; Brey, L. *Vacancy-induced magnetism in graphene and graphene ribbons.* PHYSICAL REVIEW B, 2005, volume 77, issue 19, DOI: 10.1103/PhysRevB.77.195428.

[74] Nair, R.R.; Tsai, I.L.; Sepioni, M.; Lehtinen, O.; Keinonen, J.; Krasheninnikov, A.V.; Neto, A.H.C.; Katsnelson, M.I.; Geim, A.K. *Dual origin of defect magnetism in graphene and its reversible switching by molecular doping.* NATURE COMMUNICATIONS, 2010, volume 4, DOI: 10.1038/ncomms3010.

[75] Mali, K.S.; Greenwood, J.; Adisoejoso, J.; Philipson, R.; De Feyter, S. *Nanostructuring graphene for controlled and reproducible functionalization.* NANOSCALE, 2015, volume 7, issue 5, 1566-1585 DOI: 10.1039/c4nr06470d.

[76] Karthika, P.; Rajalakshmi, N.; Dhathathreyan, K.S. *Phosphorus-doped exfoliated graphene for supercapacitor electrodes.* JOURNAL OF NANOSCIENCE AND NANOTECHNOLOGY, 2013, volume 13, DOI: 10.1166/jnn.2013.7112.

[77] Santos, E.J.G.; Ayuela, A.; Sanchez-Portal, D. *First-principles study of substitutional metal impurities in graphene: structural, electronic and magnetic properties.* NEW JOURNAL OF PHYSICS, 2010, volume 12, DOI: 10.1088/1367-2630/12/5/053012.

[78] Qu, L.T.; Liu, Y.; Baek, J.B.; Dai, L.M. *Nitrogen-doped graphene as efficient metal-free electrocatalyst for oxygen reduction in fuel cells.* ACS NANO, 2010, volume 4, issue 3, DOI: 10.1021/nn901850u.

[79] Blonski, P.; Tuček, J.; Sofer, Z.; Mazánek, V.; Petr, M.; Pumera, M.; Otyepka M,; Zbořil, R. *Doping ith graphitic nitrogen triggers ferromagnetism in graphene.* JOURNAL OF THE AMERICAN CHEMICAL SOSIETY, 2017, volume 139, issue 8, 3171-3180, DOI: 10.1021/jacs.6b12934.

[80] Wang, Z.G.; Qin, S.J.; Wang, C.L. *Electronic and magnetic properties of single-layer graphene doped by nitrogen atoms.* EUROPEAN PHYSICAL JOURNAL B, 2014, volume 87, issue 4, DOI: 10.1140/epjb/e2014-40719-y.

[81] Wakabayashi, K.; Fujita, M.; Ajiki, H.; Sigrist, M. *Electronic and magnetic properties of nanographite ribbons.* PHYSICAL REVIEW B, 1999, volume 59, issue 12, DOI: 10.1103/PhysRevB.59.8271.

[82] Enoki, T.; Kobayashi, Y.; Fukui, K.I. *Electronic structures of graphene edges and nanographene.* INTERNATIONAL REVIEWS IN PHYSICAL CHEMISTRY, 2007, volume 26, issue 4, DOI: 10.1080/01442350701611991.

[83] Swain, A.K.; Bahadur, D. *Deconvolution of mixed magnetism in multilayer graphene.* APPLIED PHYSICS LETTERS, 2014, volume 104, issue XX, DOI: 10.1063/1.4884426.

[84] Magda, G.Z.; Jin, X.Z.; Hagymasi, I.; Vancso, P.; Osvath, Z.; Nemes-Incze, P.; Hwang, C.Y.; Biro, L.P. *Room-temperature magnetic order on zigzag edges of narrow graphene nanoribbons.* NATURE, 2014, volume 514, issue 7524, DOI: 10.1038/nature13831.

[85] Kan, M.; Zhou, J.; Sun, Q.; Wang, Q.; Kawazoe, Y.; Jena, P. *Tuning magnetic properties of graphene nanoribbons with topological line defects: From antiferromagnetic to ferromagnetic.* PHYSICAL REVIEW B, 2012, volume 85, issue 15, DOI: 10.1103/PhysRevB.85.155450.

[86] Elias, D.C.; Nair, R.R.; Mohiuddin, T.M.; Morozov, S.V.; Blake, P.; Halsall, M.P.; Ferrari, A.C.; Boukhvalov, D.W.; Katsnelson, M.I.; Geim, A.K.; Novoselov, K.S. *Control of graphene's properties by reversible hydrogenation: evidence for graphane.* SCIENCE, 2009, volume 323, issue 5941, DOI: 10.1126/science.1167130.

[87] Eng, A.Y.S.; Poh, H.L.; Sanek, F.; Marysko, M.; Matejkova, S.; Sofer, Z.; Pumera, M. *Searching for magnetism in hydrogenated graphene: using highly hydrogenated graphene prepared via birch reduction of graphite oxides.* ACS NANO, 2013, volume 7, issue 7, DOI: 10.1021/nn4016289.

[88] Joshi, R.K.; Alwaarappan, S.; Yoshimura, M.; Sahajwalla, V.; Nishina, Y. *Graphene oxide: the new membrane material.* APPLIED MATERIALS TODAY, 2015, DOI: 10.1016/j.apmt.2015.06.002.

[89] Zboril, R.; Karlicky, F.; Bourlinos, A.B.; Steriotis, T.A.; Stubos, A.K.; Georgakilas, V.; Safarova, K.; Jancik, D.; Trapalis, C.; Otyepka, M. *Graphene fluoride: A stable stoichiometric graphene derivative and its*

chemical conversion to graphene SMALL, 2010, volume 6, issue 24, DOI: 10.1002/smll.201001401.

[90] Urbanová, V.;, Holá, K.; Bourlinos A.B.; Čépe, K.; Ambrosi, A.; Loo, A.H.; Pumera, M.; Karlický, F.; Otyepka, M.; Zbořil, R. *Thiofluorographene-hydrophilic graphene derivative with semiconducting and genosensing properties.* ADVANCED MATERIALS, 2015, volume 27, issue 14, DOI: 10.1002/adma.201500094.

[91] Urbanová, V.;, Holá, K.; Bourlinos A.B.; Čépe, K.; Ambrosi, A.; Loo, A.H.; Pumera, M.; Karlický, F.; Otyepka, M.; Zbořil, R. *Thiofluorographene-hydrophilic graphene derivative with semiconducting and genosensing properties.* ADVANCED MATERIALS, 2015, volume XX, issue XX, DOI: 10.1002/adma.201500094.

[92] Kuila, T.; Bose, S.; Mishra, A.K.; Khanra, P.; Kim, N.H.; Lee, J.H. *Chemical functionalization of graphene and its applications.* PROGRESS IN MATERIALS SCIENCE, 2015, volume 57, issue 7, DOI: 10.1016/j.pmatsci.2012.03.002.

[93] Berashevich, J.; Chakraborty, T. *Sustained ferromagnetism induced by H-vacancies in graphane.* NANOTECHNOLOGY, 2010, volume 21, issue 35, DOI: 10.1088/0957-4484/21/35/355201.

[94] Sahin, H.; Ataca, C.; Ciraci, S. *Electronic and magnetic properties of graphane nanoribbons.* PHYSICAL REVIEW B, 2010, volume 81, issue 20, DOI: 10.1103/PhysRevB.81.205417.

[95] Eng, A.Y.S.; Poh, H.L.; Šaněk, F.; Maryško, M.; Matějková, S.; Sofer, Z.; Pumera, M. *Searching for magnetism in hydrogenated graphene: using highly hydrogenated graphene prepared via birch reduction of graphite oxides.* ACS NANO, 2013, volume 7, issue 7, DOI: 10.1021/nn4016289.

[96] Sun, P.; Wang, K.; Wei, J.; Zhong, M.; Wu, D.; Zhu, H. *Magnetic transitions in graphene derivatives.* NANO RESEARCH, 2014, volume 7, issue 10, DOI: 10.1007/s12274-014-0512-1.

[97] Tuček, J.; Holá, K.; Bourlinos A.B.; Blonski, P.; Bakandritsos, A.; Ugolotti, J.; Dubecký, M.; Karlický, F.; Ranc, V.; Čépe, K.; Otyepka, M.; Zbořil, R. *Room temperature organic magnets derived from sp^3 functionalized graphene.* NATURE COMMUNICATIONS, 2017, volume 8, DOI: 10.1038/ncomms14525.

[98] Born, M.; Oppenheimer, R. *Zur quantentheorie der molekeln.* ANNALEN DER PHYSIK, 1927, volume 389, issue 20, 457-484, DOI: 10.1002/andp.19273892002.

[99] Lieb, E.H.; Simmon, B. *The Thomas-Fermi theory of atoms, molecules and solids.* REVIEWS OF MODERN PHYSICS, 1981, volume 603, issue 53, DOI: 10.1016/0001-8708(77)90108-6.

[100] Hohenberg, P.; Kohn, W. *Inhomogeneous electron gas.* PHYSICAL REVIEW, 1964, volume 136, DOI: 10.1103/PhysRev.136.B864.

[101] Gross, A. *Theoretical surface science: a microscopic perspective.* 2nd ed. London: Springer, 2009. ISBN: 978-3-540-68966-9, DOI: 10.1007/978-3-540-68969-0

[102] Sasioglu, E. *First-principles study of the exchange interactions and Curie temperature in Heusler alloys.* Disertation, Faculty of Mathematics and Natural Sciences and Technology of the Martin Luther University, Halle-Wittenberg, 2006.

[103] Perdew, J.P.; Yue, W. *Accurate and simple density functional for the electronic exchange energy: Generalized gradient approximation.* PHYSICAL REVIEW B, 1986, volume 40, DOI: 10.1103/PhysRevB.33.8800.

[104] Perdew, J.P.; Chevary, J.A.; Vosko, S.H.; Jackson, K.A.; Pederson, M.R.; Singh, D.J.; Fiolhais, C. *Atoms, molecules, solids, and surfaces: Applications of the generalized gradient approximation for exchange and correlation.* PHYSICAL REVIEW B, 1992, volume 48, DOI: 10.1103/PhysRevB.46.6671.

[105] Bhandary, S. *First principles studies of functional materials based on graphene and organometallics.* Disertation, Faculty of Science and Technology of the Uppsala University, ISBN 978-91-554-8869-7.

[106] Argaman, N.; Makov, A. *Density functional theory: An introduction.* American Journal of Physics. 2000, ISSN 00029505, DOI: 10.1119/1.19375.

[107] Thonhauser, T. *Theory of orbital magnetization in solids.* International Journal of Modern Physics B. 2011.

[108] Zeller. R. *Spin-polarized DFT calculations and magnetism.* John von Neumann Institute for Computing, Jülich, Computational Nanoscience, 2006, NIC Series, Vol. 31, ISBN 3-00-017350-1.

[109] von Barth, U.; Hedin, L. *A local exchange-correlation potential for the spin polarized case.* SOLID STATE PHYSICS, 1972, volume 5, issue 13, 1629-1642.

[110] Perdew, J.P.; Zunger, A. *Self-interaction correction of density-functional theory for many electron systems.* PHYSICAL REVIEW B, 1981, volume 23, 5048-5079.

[111] Perdew, J.P.; Burke, K.; Ernzerhof, M. *Generalized gradient approximation made simple.* PHYSICAL REVIEW LETTERS, 1996, volume 77, issue 13, 3865-3868.

[112] Bloch, F. *Pseudopotential – Wikipedia, the free encyclopedia.* Accessed on-line: *http://en.wikipedia.org/wiki/Pseudopotential*

[113] Phillips, J.C.; Kleinman, L. *New Method for calculating wave functions in crystals and molecules.* PHYSICAL REVIEW LETTERS, 1959, DOI: 10.1103/PhysRev.116.287.

[114] Hammann, D.R.; Schlüre, M.; Chaing, C. *Norm-conserving Pseudopotentials.* PHYSICAL REVIEW LETTERS, 1979, volume 43, issue 1494, DOI: 10.1103/PhysRevLett.43.1494.

[115] Quester, W. *Quantum mechanics of electrons in crystal lattices.*Z. Physik, 1929, volume 52, DOI:10.1007/BF01339455.

[116] Karhánek, D. *Self-assembled monolayers studied by density-functional theory.* Disertation, Computational Materials Physics, University of Vienna, Austria.

[117] Blöchl, P.E. *Projector augmented-wave method.*Physical review B, 1994, volume 50, DOI: 10.1103/PhysRevB.50.17953.

[118] Kresse, G.; Joubert, D. *From ultrasoft pseudopotentials to the projector augmented-wave method.*Physical review B, 1998, volume 59, DOI: 10.1103/PhysRevB.59.1758.

[119] Kollman, B. *Shockley surface states calculated within density functional theory.* Master thesis, institute for physics, University in Gratz, Austria, 2014.

[120] Grüneis, A. *Diagrammatic techniques for extend systems: MP2 and CCSD.* Disertation, Computational Materials Physics, University of Vienna, Austria, 2011.

[121] Blöchl, P.E.; Jepsen, O.; Andersen, O.K. *Improved tetrahedron method for Brillouin-zone integrations.*Physical review B, 1994, volume 49, DOI: 10.1103/PhysRevB.49.16223

[122] http://www.iue.tuwien.ac.at/phd/goes/dissse14.html

[123] Li, X.; Wang, X.; Zhang, L.; Lee, S.; *Chemically derived, ultrasmooth graphene nanoribbon semiconductors.* SCIENCE, 2008, DOI: 10.1126/science.1150878

[124] Barone V.; Hod, O.; Scuseria G. *Electronic structure and stability of semiconducting graphene nanoribbons.* NANO LETTERS, 2006, DOI: 10.1021/nl0617033

[125] Son, Y.; Cohen, M.L; Louie S.G. *Energy Gaps in Graphene Nanoribbons.*PHYSICAL REVIEW LETTERS, 2006, DOI: 10.1103/PhysRevLett.97.216803

[126] Ma, F.; Guo, Z.; Xu, K.; Chu, P. *First-principles study of energy band structure of armchair graphene nanoribbons.* SOLID STATE COMMUNICATIONS, 2012, DOI: 10.1016/j.ssc.2012.04.058

[127] Wassman, T.; Seitsonen A.P.; Saitta, M.A.; Lazzeri, M.; Mauri, F. *Structure, stability, edge states, and aromaticity of graphene ribbons.* PHYSICAL REVIEW LETTERS, 2008, DOI: 10.1103/PhysRevLett.101.096402

[128] Lazar, P.; Zbořil, R.; Pumera, M.; Otyepka, M. *Chemical nature of boron and nitrogen dopant atoms in graphene strongly influences its electronic properties.* PHYSICAL CHEMISTRY CHEMICAL PHYSICS, 2014, DOI: 10.1039/c4cp01638f

[129] Blonski, P. Private communication.

Supplementary information

DOS of pristine nanoribbons

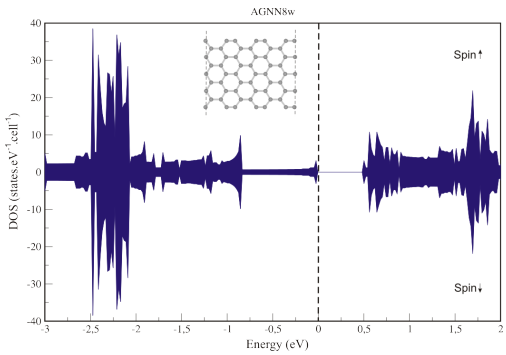

Figure 56: DOS of AGNN8w.

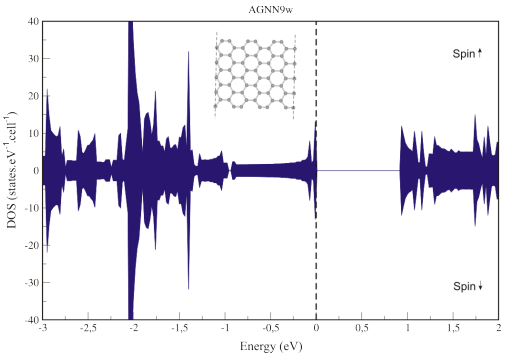

Figure 57: DOS of AGNN9w.

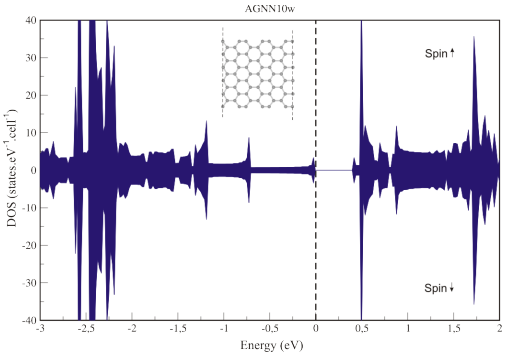

Figure 58: DOS of AGNN10w.

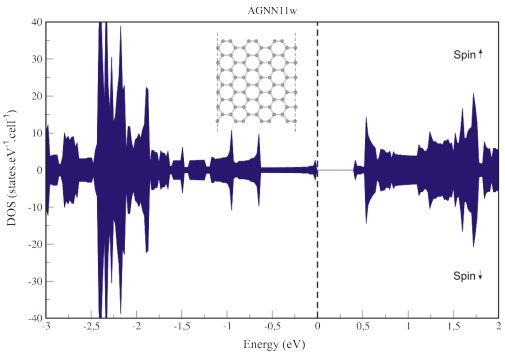

Figure 59: DOS of AGNN11w.

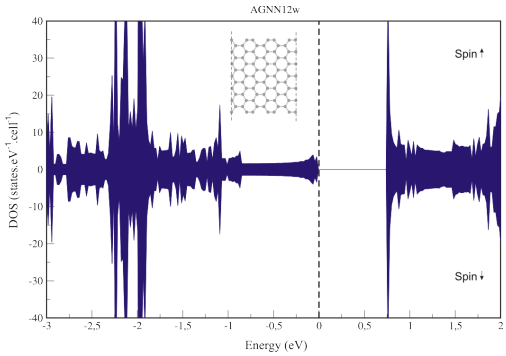

Figure 60: DOS of AGNN12w.

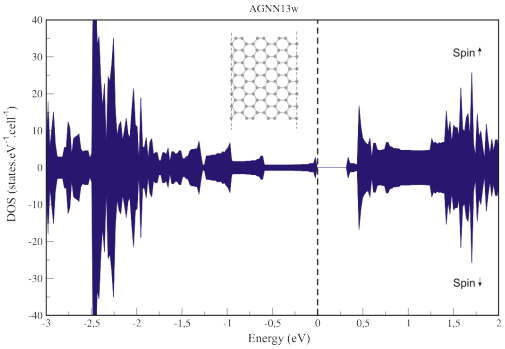

Figure 61: DOS of AGNN13w

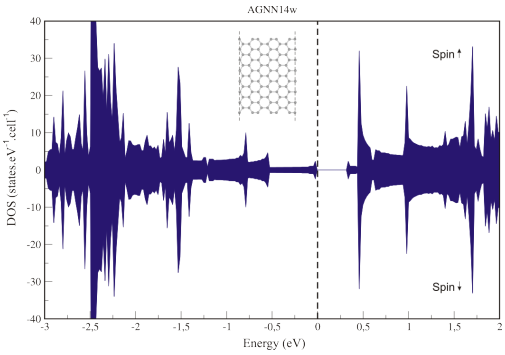

Figure 62: DOS of AGNN14w.

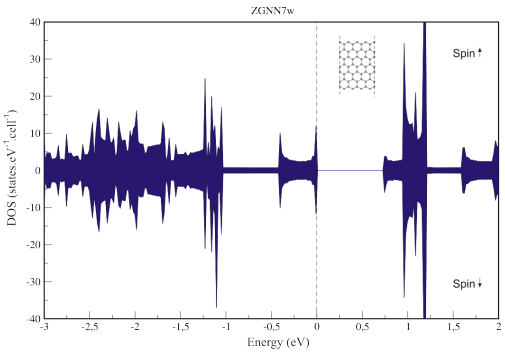

Figure 63: DOS of ZGNN7w.

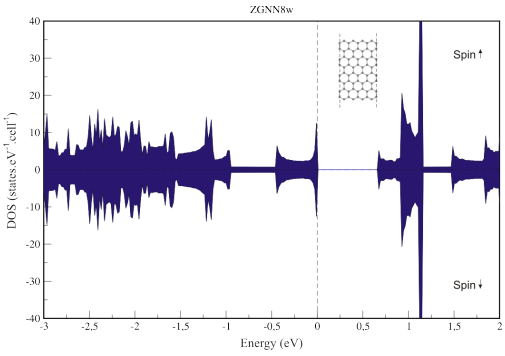

Figure 64: DOS of ZGNN8w.

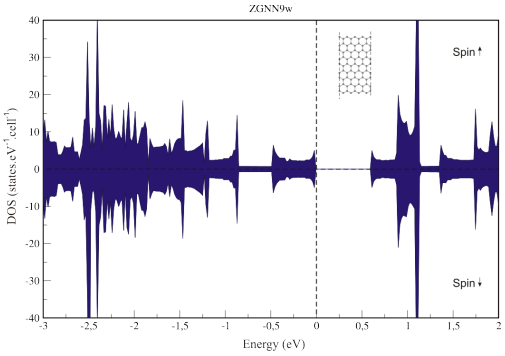

Figure 65: DOS of ZGNN9w.

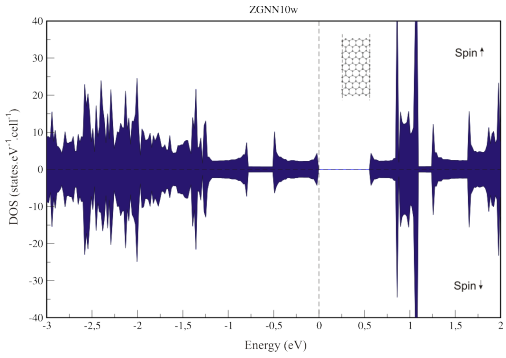

Figure 66: DOS of ZGNN10w.

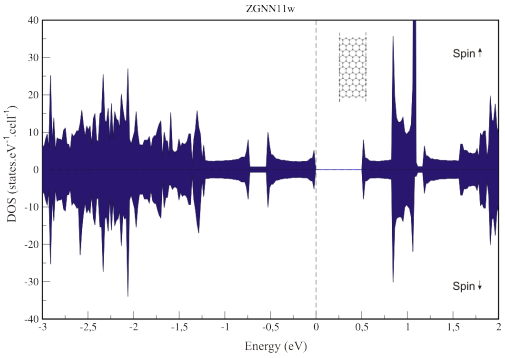

Figure 67: DOS of ZGNN11w.

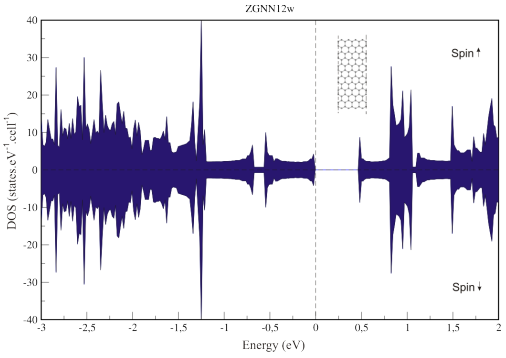

Figure 68: DOS of ZGNN12w.

DOS of pristine nanoribbons with passivated edges by hydrogen

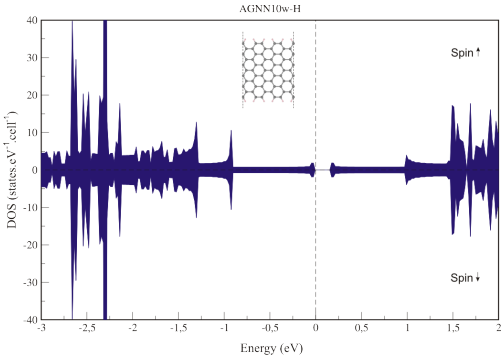

Figure 69: DOS of AGNN10w-H.

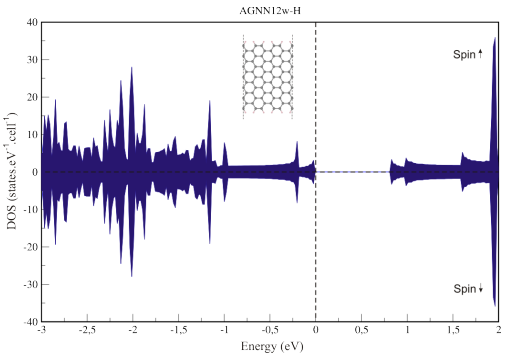

Figure 70: DOS of AGNN12w-H.

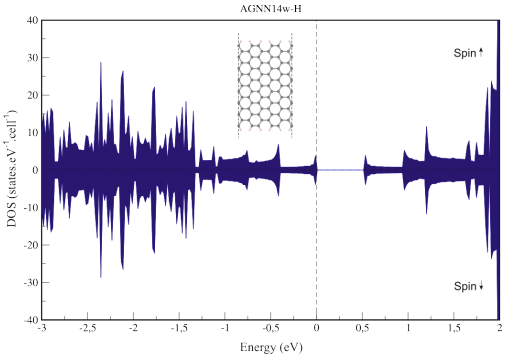

Figure 71: DOS of AGNN14w-H.

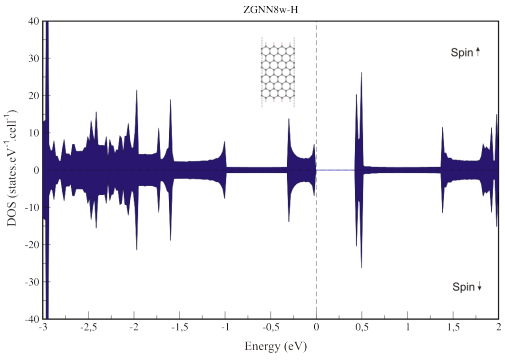

Figure 72: DOS of ZGNN8w-H.

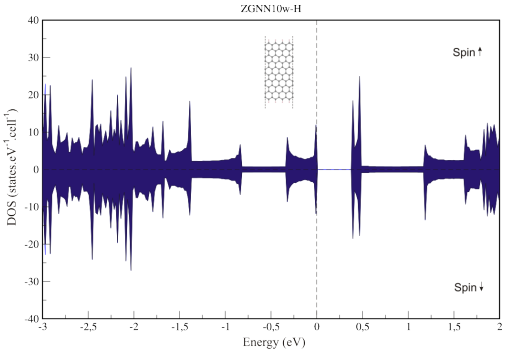

Figure 73: DOS of ZGNN10w-H.

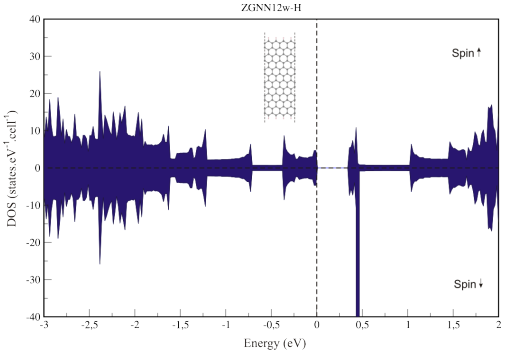

Figure 74: DOS of ZGNN12w-H.

DOS of *GNNs* with two hetero atoms in para position

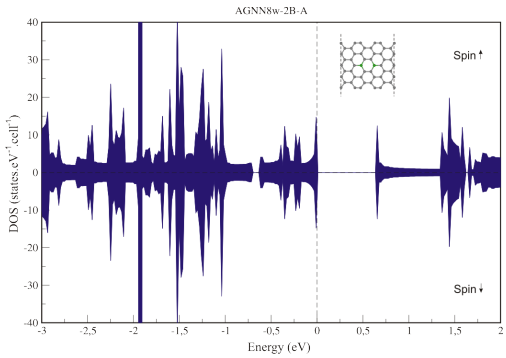

Figure 75: DOS of AGNN8w-2B-A.

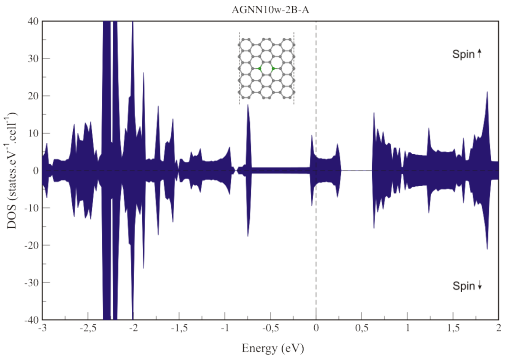

Figure 76: DOS of AGNN10w-2B-A.

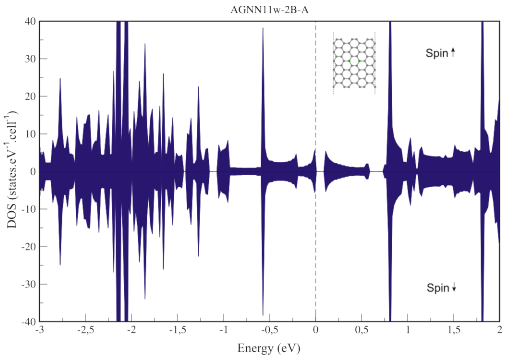

Figure 77: DOS of AGNN11w-2B-A.

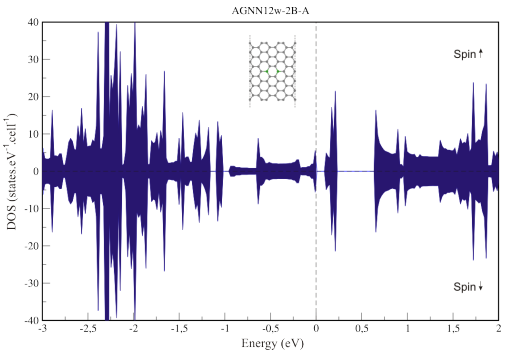

Figure 78: DOS of AGNN12w-2B-A.

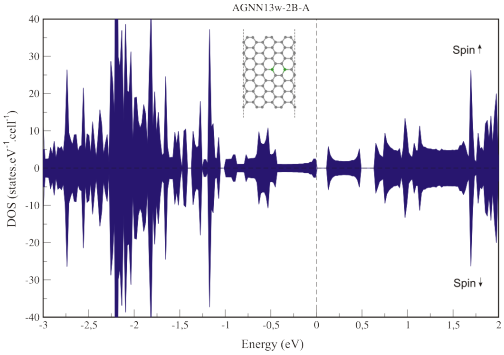

Figure 79: DOS of AGNN13w-2B-A.

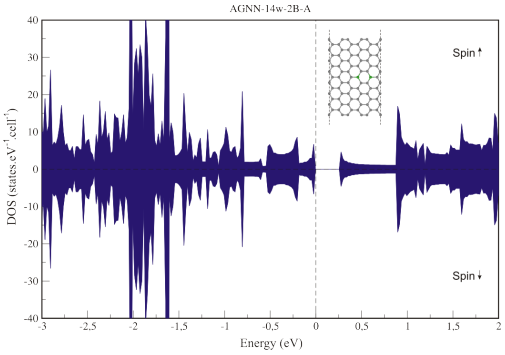

Figure 80: DOS of AGNN14w-2B-A

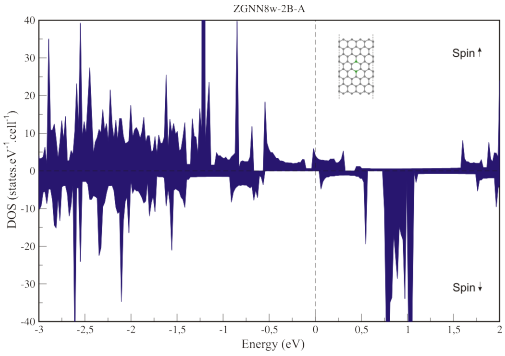

Figure 81: DOS of ZGNN8w-2B-A.

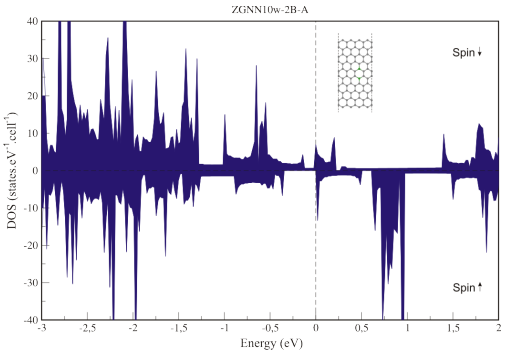

Figure 82: DOS of ZGNN10w-2B-A.

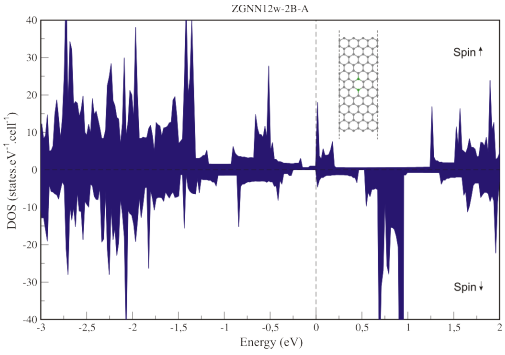

Figure 83: DOS of ZGNN12w-2B-A.

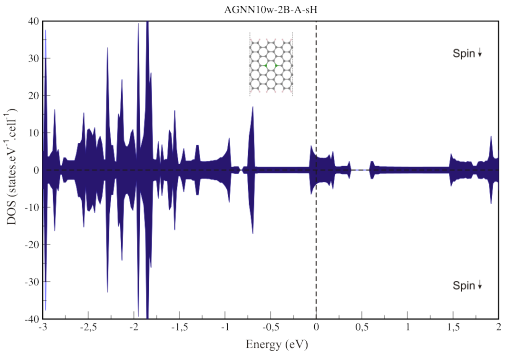

Figure 84: DOS of AGNN10w-2B-A-sH.

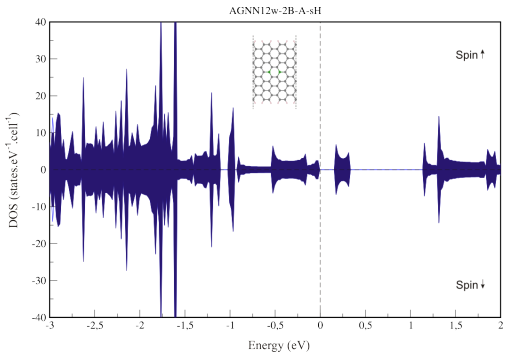

Figure 85: DOS of AGNN12w-2B-A-sH

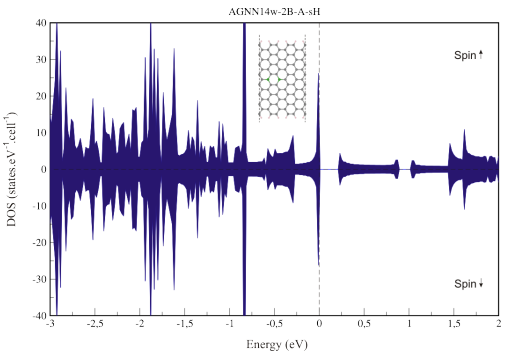

Figure 86: DOS of AGNN14w-2B-A-sH

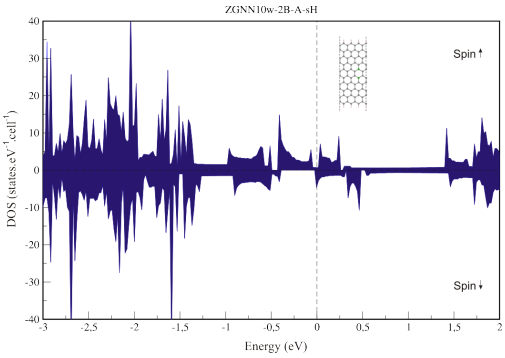

Figure 87: DOS of ZGNN10w-2B-A-sH.

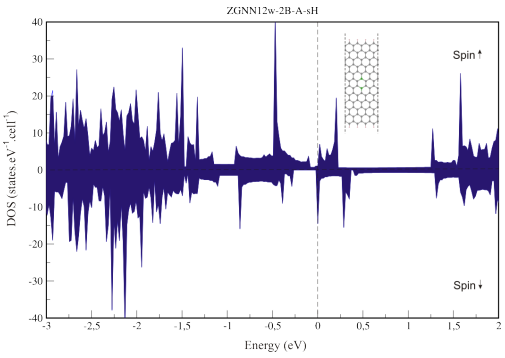

Figure 88: DOS of ZGNN12w-2B-A-sH.

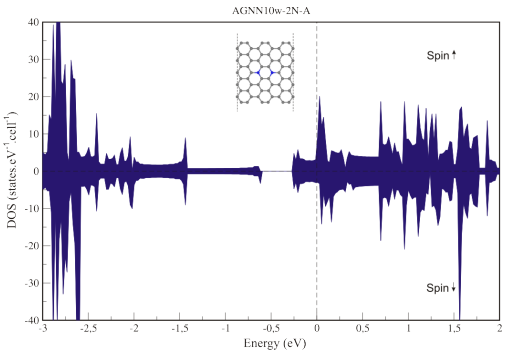

Figure 89: DOS of AGNN10w-2N-A.

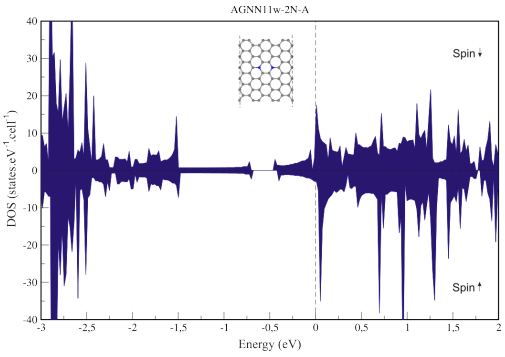

Figure 90: DOS of AGNN11w-2N-A.

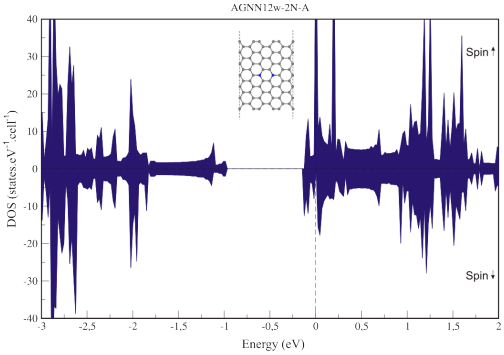

Figure 91: DOS of AGNN12w-2N-A.

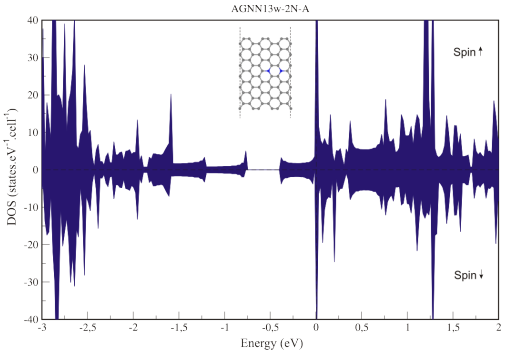

Figure 92: DOS of AGNN13w-2N-A.

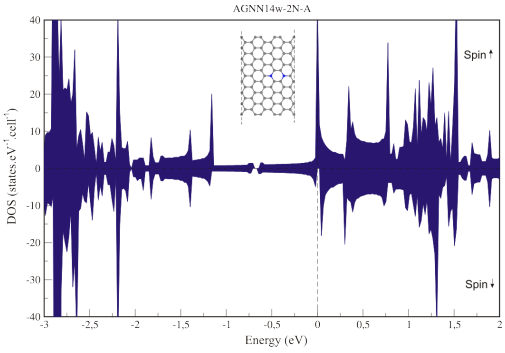

Figure 93: DOS of AGNN14w-2N-A.

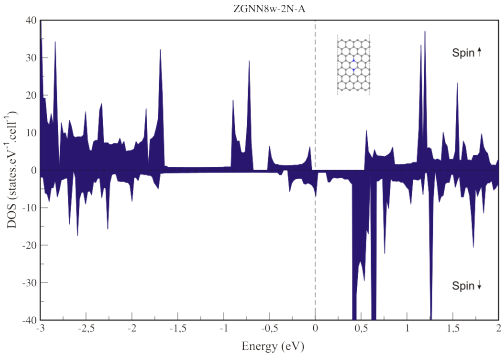

Figure 94: DOS of ZGNN8w-2B-A.

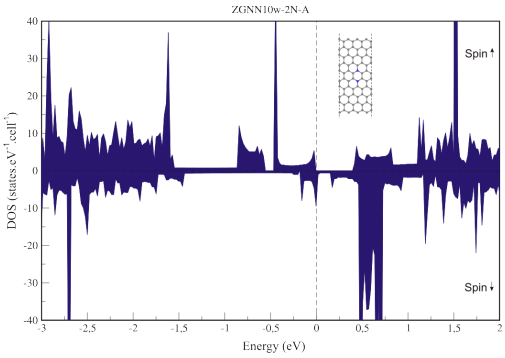

Figure 95: DOS of ZGNN10w-2N-A.

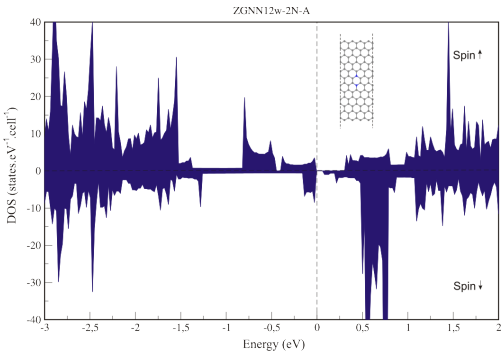

Figure 96: DOS of ZGNN12w-2N-A.

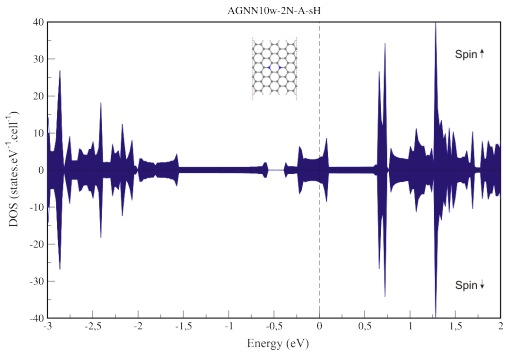

Figure 97: DOS of AGNN10w-2N-A-sH.

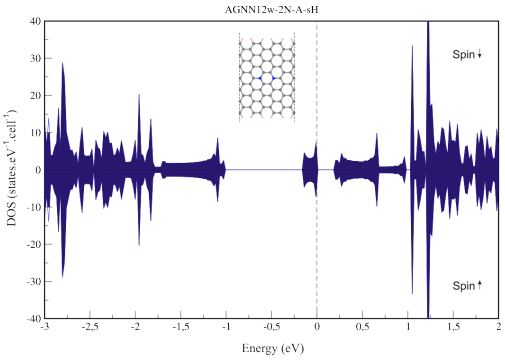

Figure 98: DOS of AGNN12w-2N-A-sH.

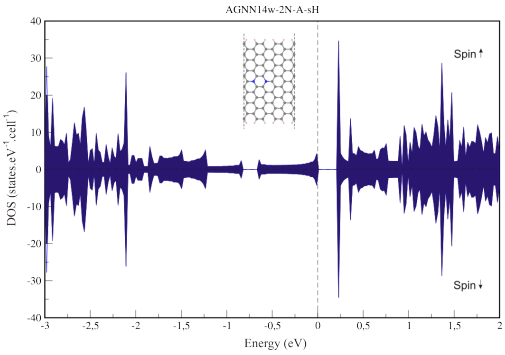

Figure 99: DOS of AGNN14w-2N-A-sH.

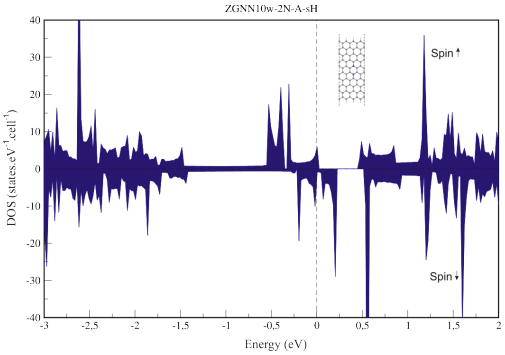

Figure 100: DOS of ZGNN10w-2B-A-sH.

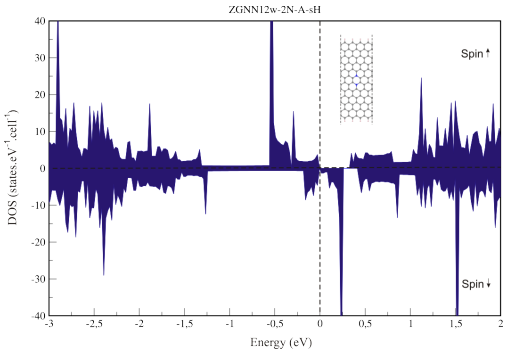

Figure 101: DOS of ZGNN12w-2N-A-sH.

DOS of *GNNs* with 3 heteroatoms in configuration C

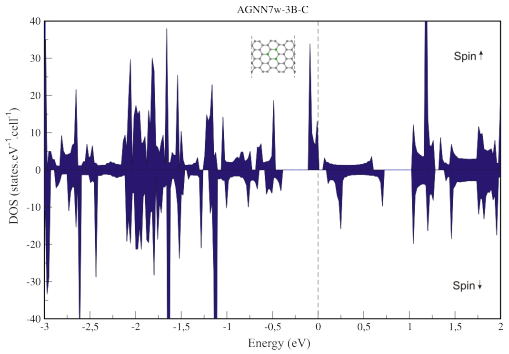

Figure 102: DOS of AGNN7w-3B-C.

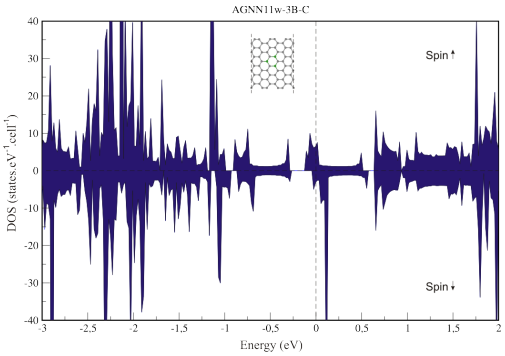

Figure 103: DOS of AGNN11w-3B-C.

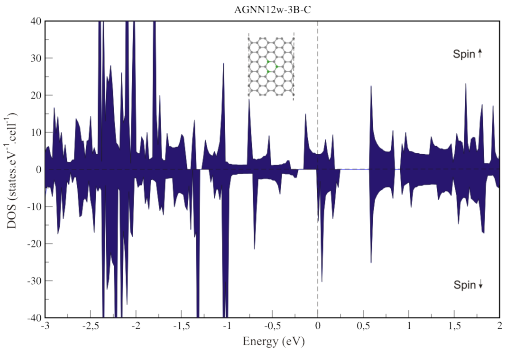

Figure 104: DOS of AGNN13w-3B-C.

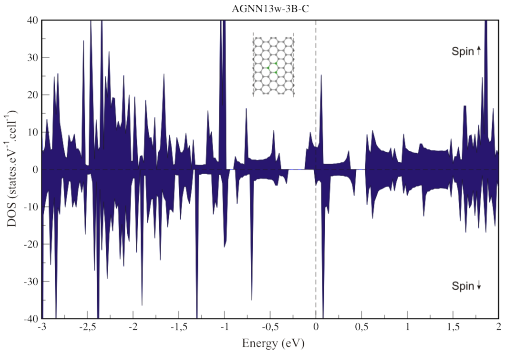

Figure 105: DOS of AGNN13w-3B-C.

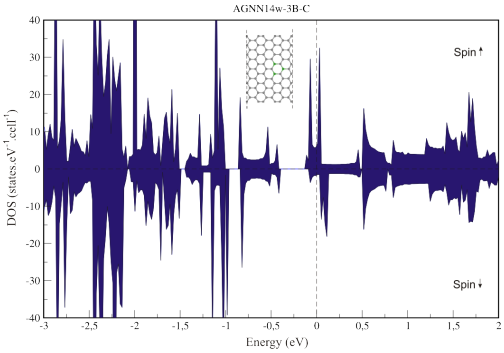

Figure 106: DOS of AGNN14w-3B-C.

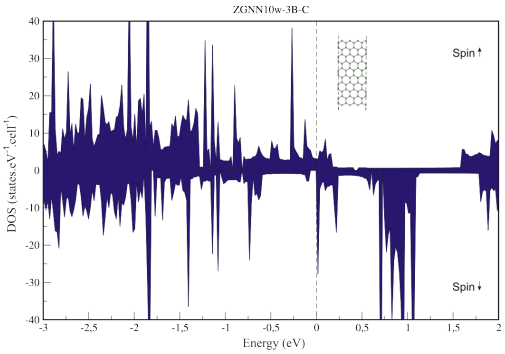

Figure 107: DOS of ZGNN10w-3B-C.

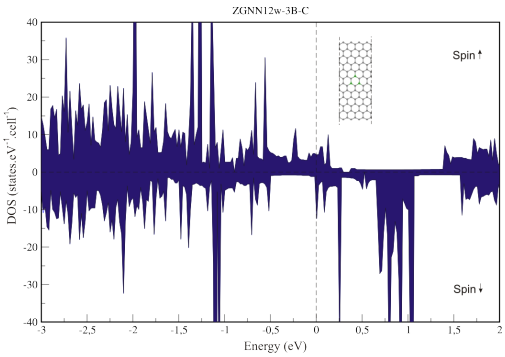

Figure 108: DOS of ZGNN12w-3B-C.

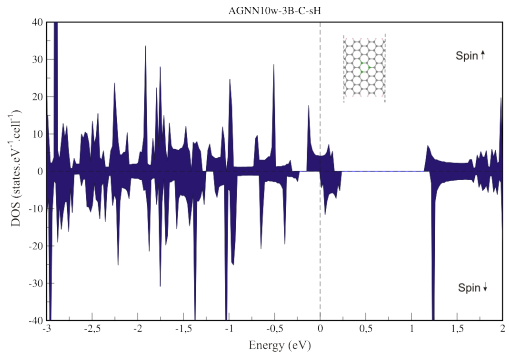

Figure 109: DOS of AGNN12w-3B-C-sH.

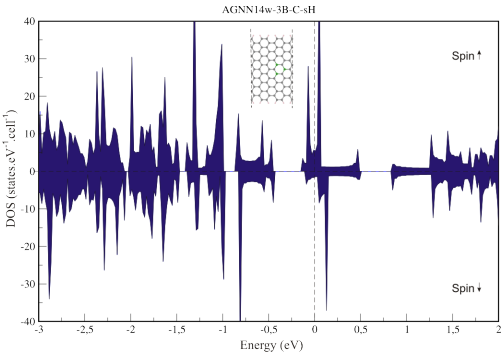

Figure 110: DOS of AGNN14w-3B-C-sH.

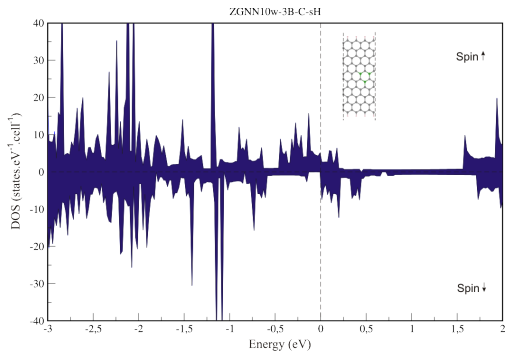

Figure 111: DOS of ZGNN10w-3B-C-sH.

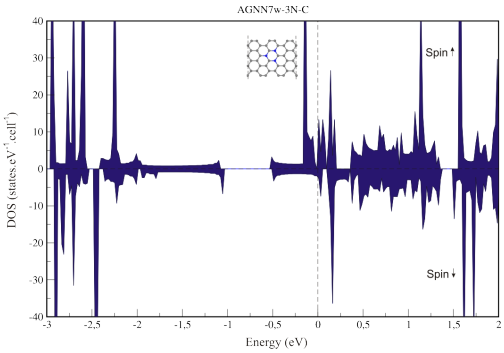

Figure 112: DOS of AGNN7w-3N-C.

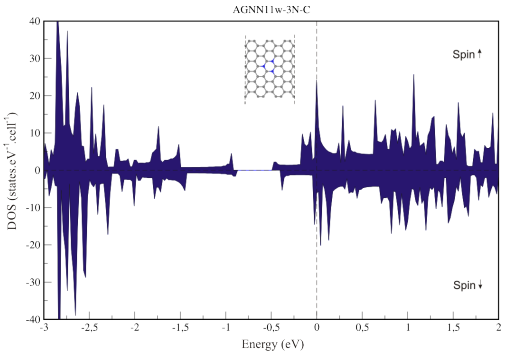

Figure 113: DOS of AGNN11w-3N-C.

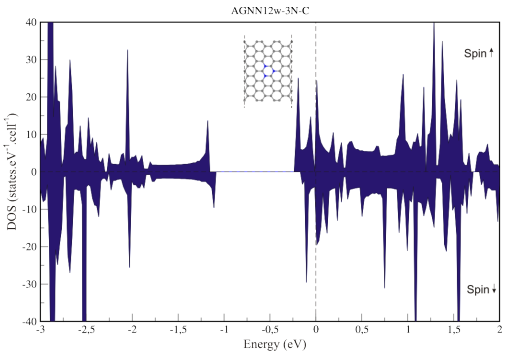

Figure 114: DOS of AGNN12w-3N-C.

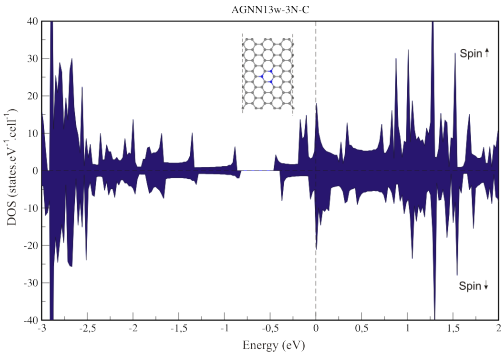

Figure 115: DOS of AGNN13w-3B-C.

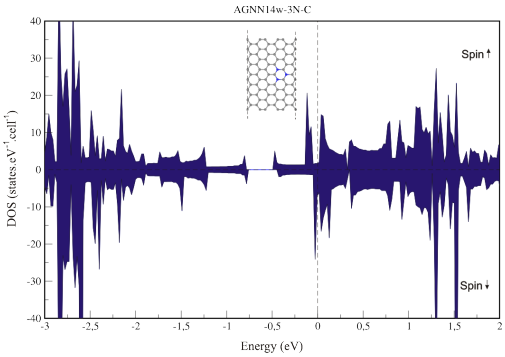

Figure 116: DOS of AGNN14w-3N-C.

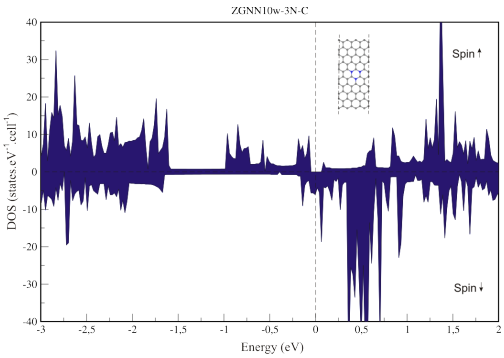

Figure 117: DOS of ZGNN10w-3N-C.

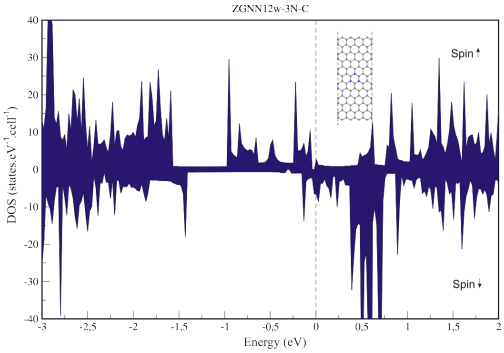

Figure 118: DOS of ZGNN12w-3N-C.

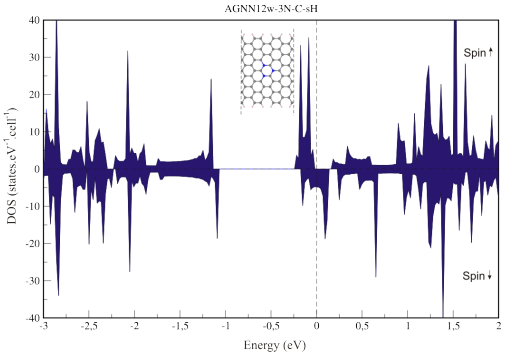

Figure 119: DOS of AGNN12w-3N-C-sH.

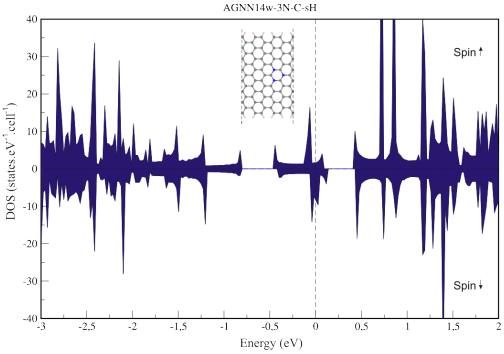

Figure 120: DOS of AGNN14w-3N-C-sH.

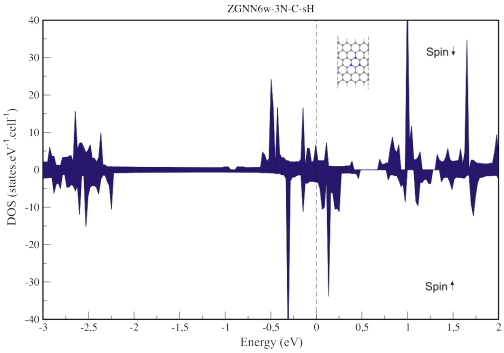

Figure 121: DOS of AGNN13w-3B-C.

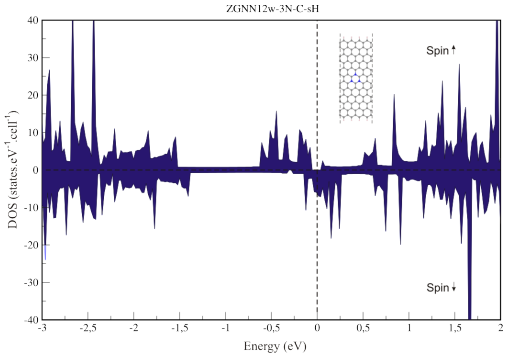

Figure 122: DOS of ZGNN12w-3N-C-sH.